Università degli studi di Padova

Centro ricerche Fusione

RESEARCH DOCTORATE IN FUSION SCIENCE AND ENGINEERING
Cycle XXXVI

Review and comparison of divertor configurations for High Magnetic Field Tokamak

Coordinator: Dr. Gianmaria De Tommasi
Supervisor: Dr. Paolo Innocente
University Supervisor: Prof. Leonardo Giudicotti

PhD student:
Muscente Paola

Contents

Abstract

In recent decades, the global energy demand has undergone a significant increase, leading to the urgent need to increase and develop new sources of renewable energy. Among alternative energy sources, nuclear fusion stands out as potentially abundant, continuous, clean, and safe. To achieve the required fusion rate to produce energy, the hot ($\sim 10^3$ eV) and dense ionised gas ($\sim 10^{20} \mathrm{m}^{-3}$), in a state called *plasma*, must be confined sufficiently long. One of the most promising fusion devices is the *tokamak*, based on magnetic confinement of the plasma. However, effective magnetic confinement does not exempt the tokamak wall from receiving energy and particle fluxes. Therefore, these fluxes must be compatible with the power handling capabilities and erosion lifetime of the components in contact with the plasma. To maintain a pure and dense plasma that reduces radiation losses and minimises plasma dilution, the plasma chamber must be in high vacuum. Moreover, a magnetic confinement method called *divertor* is used to split the plasma volume into a hot and dense plasma region, the *core*, and a colder outer region called the *Scrape-Off Layer* (SOL). Managing the *Power Exhaust* (PEX) has been identified as one of the main challenges in achieving magnetic confinement fusion. As the size of the tokamak and plasma duration increase, which are necessary conditions for a future reactor, controlling energy and particle losses will become even more challenging, eventually flowing to the divertor target surfaces exceeding the current technological limits of materials. Several ongoing studies are dedicated to addressing this issue. Among the possible solutions, there is the "detachment" regime associated with various advanced-tokamak scenarios and alternative divertor configurations (ADCs) that can increase radiation at the divertor without degrading it in the plasma centre.

The work presented here is dedicated to the study of the plasma at the edge, in the SOL, and the divertor region, with the ultimate goal of contributing to the development and improvement of current and future devices, such as DTT (Divertor Tokamak Test facility) and ITER (International Thermonuclear Experimental Reactor). The first part of the PhD was dedicated to studying the principles of edge and SOL physics, the *Two-point model*, which describes in first approximation the physics of the SOL, the 2D fluid code *SOLEDGE2D-EIRENE* and the

3D turbulent code *SOLEDGE3X*. Subsequently, we focused on the analysis of the power exhaust and its impact on the edge plasma in different types of magnetic configuration, such as the conventional Single-Null (SN), the Negative Triangularity (NT) and the Super-X Divertor (SXD).

One of the most promising among the advanced tokamak scenarios is the Negative Triangularity (NT) configuration, which achieves reactor-relevant conditions in the plasma core without, however, exhibiting the dangerous *Edge Localised Modes* (ELMs), instabilities that are present in the more commonly used Positive Triangularity High-Confinement mode (PT H-Mode) configuration. To understand the transport of energy and particles at the plasma edge of NT and to determine whether this configuration could be a viable alternative in terms of power exhaust, analytical and numerical studies have been conducted using TCV (Tokamak à configuration variable) experiments and the SOLEDGE2D-EIRENE code. Furthermore, studies in this field have been started using the turbulent code SOLEDGE3X.

The *detachment* regime for future fusion reactors, thanks to the reduction of the particle and heat fluxes on the divertor targets, allows a decrease in erosion and melting of the wall material. Among the optimal configurations to achieve these conditions, there is the alternative SXD. This magnetic configuration is characterised by a larger outer strike point radius than the conventional PT, resulting in a decrease in parallel heat flux along the flux tube and, therefore, in a lower temperature at the divertor targets. We have used experiments on TCV and the SOLEDGE2D code to study its potential.

Magnetic confinement fusion devices must have high confinement in the core to maximise fusion reactions and plasma conditions in the divertor that are compatible with the limits of plasma-facing components. In the PT H-Mode configuration, the density at its transport barrier (pedestal top, $n_{e,ped}$) is an essential indicator of confinement quality, while the density at the separatrix ($n_{e,sep}$), which is the last flux surface between the core and the SOL, is a crucial factor in determining the divertor regime. For this reason, several studies have been conducted on the relationship between $n_{e,sep}$ and $n_{e,ped}$ using JET (Joint European Torus) experiments conducted in two possible divertor configurations known as Vertical-Vertical and Corner-Corner.

Sommario

Negli ultimi decenni il fabisogno globale di energia ha subito un notevole aumento, portando all'urgente necessità di incrementare e sviluppare nuove fonti di energia rinnovabile. Tra le fonti di energia alternative si distingue la fusione nucleare in quanto potenzialmente abbondante, continua, pulita e sicura. Per avere il *fusion-rate* necessario per produrre energia, il gas ionizzato caldo e denso, in stato di plasma, deve essere confinato per un periodo sufficientemente lungo: uno tra i device da fusione più promettenti è il *tokamak* basato sul confinamento magnetico. Un buon confinamento magnetico non esula però la parete del tokamak dal ricevere flussi di energia e particelle ed è quindi condizione necessaria che questi flussi siano compatibili con le capacità di gestione dell'energia e dell'erosione dei componenti a contatto con il plasma.

Per mantenere un plasma puro e denso, cioè per ridurre le perdite da radiazione e minimizzare la diluizione del plasma, la sua camera contenitiva viene posta in alto vuoto e si utilizza un metodo di confinamento magnetico chiamato divertore. Quest'ultimo divide il volume del plasma in un nucleo caldo e denso (*core*) e una regione più esterna e fredda chiamata *Scrape-Off Layer* (SOL). La gestione del *Power Exhaust* (PEX) è stato identificato come una delle sfide principali per la realizzazione della fusione a confinamento magnetico. Infatti, all'aumentare delle dimensioni del tokamak e della durata del plasma, condizioni necessarie per un futuro reattore, avere sotto controllo le perdite di energia e particelle diverterà ancora più impegnativo fino ad avere flussi sui target del divertore che superano il limite tecnologico attuale dei materiali. Per risovere questo problema sono in corso diversi e numerosi studi dedicati. Tra le possibili soluzioni vi è il regime di *detachment* associato a diversi scenari avanzati e configurazioni magnetiche alternative (ADCs) che sono in grado di aumentare la radiazione al divertore senza però degradarla nel centro plasma.

Il lavoro qui presentato è dedicato allo studio del plasma al bordo (*edge*), nel SOL e nella zona divertore, e ha come obiettivo finale quello di contribuire allo sviluppo e il miglioramento delle macchine attuali e future, come DTT (Divertor Tokamak Test facility) e l'ITER (International Thermonuclear Experimental Reactor). La prima parte del dottorato è stata dedicata allo studio dei principi

della fisica di bordo e del SOL, del Two-point model, che permette di descrivere in prima approssimazione le dinamiche coinvolte nel SOL, del codice fluido 2D SOLEDGE2D-EIRENE e del codice turbolento 3D SOLEDGE3X. In seguito, ci si è concentrati sull'analisi del PEX e del suo impatto sul plasma di bordo in diversi tipi di configurazione magnetica, come la convenzionale *Single-Null* (SN), la *Negative TriangularITY* e il *Super-X Divertor* (SXD).

Uno tra i più promettenti scenari avanzati è la configurazione a NT, la quale raggiunge condizioni *reactor-relevant* nel core del plasma non presentando però le pericolose instabilità *Edge Localised Modes* (ELMs), che sono invece presenti nella finora più utilizzata configurazione a Triangularità Positiva ad alto confinamento (PT H-Mode). Per comprendere il trasporto di energia e particelle al bordo plasma della NT e per determinare se questa configurazione potrebbe rappresentare una valida alternativa dal punto di vista del power exhaust, sono stati fatti studi analitici e numerici utilizzando esperimenti di TCV (Tokamak à configuration variable). Inoltre, sono stati avviati in questo campo studi utilizzando il codice turbolento SOLEDGE3X.

Il regime di *detachment* per i futuri reattori a fusione, grazie alla riduzione del flusso di particelle e calore che consente di ottenere sui target del divertore, consente di ridurre l'erosione e fusione del materiale di parete. Tra le configurazioni ottimali per ottenere queste condizioni vi è la ADC *Super-X Divertor* (SXD). Questa configurazione magnetica è caratterizzata dall'avere lo *strike point* esterno ad un raggio maggiore rispetto al comune PT, dal quale segue una diminuzione del flusso di calore parallelo lungo il tubo di flusso e quindi una temperatura più bassa ai *target* del divertore. Per studiare le sue potenzialità, sono stati utilizzati in questo lavoro esperimenti su TCV e il codice SOLEDGE2D.

I devices per la fusione a confinamento magnetico devono avere sia un alto confinamento nel *core*, per poter massimizzare le reazioni di fusione, sia delle condizioni del plasma nel divertore compatibili con i limiti dei componenti a contatto con il plasma. Nella configurazione PT H-Mode, la densità sulla sua barriera di trasporto (*pedestal top*, $n_{e,ped}$) è un importante indicatore della qualità del confinamento, mentre la densità alla separatrice ($n_{e,sep}$), che è l'ultima superficie di flusso posta tra il *core* e il SOL, è un fattore cruciale nel determinare il regime del divertore. Per questo motivo, sono stati fatti diversi studi sulla relazione tra $n_{e,sep}$ e $n_{e,ped}$ utilizzando esperimenti di JET (Joint European Torus) condotti in due possibili configurazioni del divertore che prendono il nome di Vertical-Vertical e Corner-Corner.

Chapter 1

Nuclear fusion and the power exhaust in tokamak devices

The global energy demands have witnessed a surge in recent decades, driven by population growth, industrialisation, and technological advancements. Traditional fossil fuels, such as coal, oil, and natural gas, are now not so abundant, and they also come with significant environmental consequences, including greenhouse gas emissions and climate change. Nuclear fusion is a promising alternative energy source for global energy demands: abundant, continuous, clean and safe. Thanks to the good results it obtained over time, the tokamak is one of the most advanced and studied fusion concepts.

Successful realisation of fusion production in tokamak reactors must consider that the power and particle fluxes directed towards the reactor vessel must be compatible with the power handling capabilities and erosion lifetime of the plasma-facing components (PFCs). Erosion of PFCs can generate impurities that, entering the confined plasma, lead to fuel dilution and increase electromagnetic radiative losses with a consequent decrease of the fusion power production [75]. One key concept toward resolving these problems is the divertor configuration explained in detail in section 1.3.1. Moreover, as tokamak size and pulse length duration increase, power exhaust becomes even more challenging for future devices, so successfully resolving such issues is essential. For this reason, different advanced divertor approaches are under investigation on current devices (see section 1.3).

5

1.1 The global energy demand problem

In response to the urgent need for sustainable energy solutions, there has been a growing emphasis on exploring and implementing renewable energy sources such as solar, wind, hydropower, geothermal, and nuclear power. Energy transitioning requires careful planning, investment, and global cooperation. The challenge lies in meeting the current energy demands, ensuring that future energy needs are met in an environmentally responsible and sustainable manner, and finding innovative ways to balance energy security, economic growth, and environmental stewardship. Based on the current international commitments to address climate change, it is imperative to decarbonise our energy systems. For this reason, the European Union has adopted an Energy Roadmap, which foresees an 80% reduction in energy-related greenhouse gas emissions by 2050. This ambitious goal necessitates a significant shift towards decarbonised power sources, including fossil fuel power plants equipped with CCS (Carbon Capture and Storage), nuclear power plants and various renewable energy technologies. As for nuclear power, besides nuclear fission generation III+ and IV reactors, fusion power plants could contribute [16].

1.2 Nuclear Fusion

Nuclear fusion is the process of combining two light atoms to form a heavier one in which the mass difference converts into energy. Without enough gravity force, all electrons must be removed from the atoms to facilitate nuclei interaction, transitioning the fuel to the state of *plasma*. In this new state, only with sufficient energy do the two nuclei come close enough for the strong nuclear force to overcome the Coulomb force to have fusion[1].

The most promising fusion nuclear reaction is the one between deuterium and tritium. In figure 1.1, we can see that in the range of temperature 5-20 keV, for example, the ratio of $< \sigma v >$ for D-T reaction to that of D-D is around 80, thus showing its supremacy [101]. The reaction

$$D + T \rightarrow {}^4He + n$$
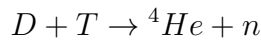
releases an energy of 17.6 MeV, of which 3.5 MeV accounts for the kinetic energy of the ${}^4He$ (α-particles), while 14.1 MeV is of the released neutron. Deuterium is an abundant hydrogen isotope extractable from water. However, tritium is an unstable isotope with a half-life of about 15 years, so it has to be necessarily produced. As mentioned above, sufficient energy is required to overcome the repulsion between the D and T ions and induce the reaction. Quantum mechanical tunnelling

---

[1]In stars, the fusion reaction occurs thanks to the enormous amount of gravity, which allows to overcome the Coulomb barrier between nuclei.

enables the most significant cross-section to occur at approximately 100 keV, lower than the energy needed to exceed the Coulomb barrier. The reaction rate in a hot D-T plasma is determined by integrating over the two species' Maxwellian distributions. It can be expressed as

$$R = n_d n_t \langle \sigma v \rangle$$

where n_d and n_t represent the deuterium and tritium densities. The thermonuclear
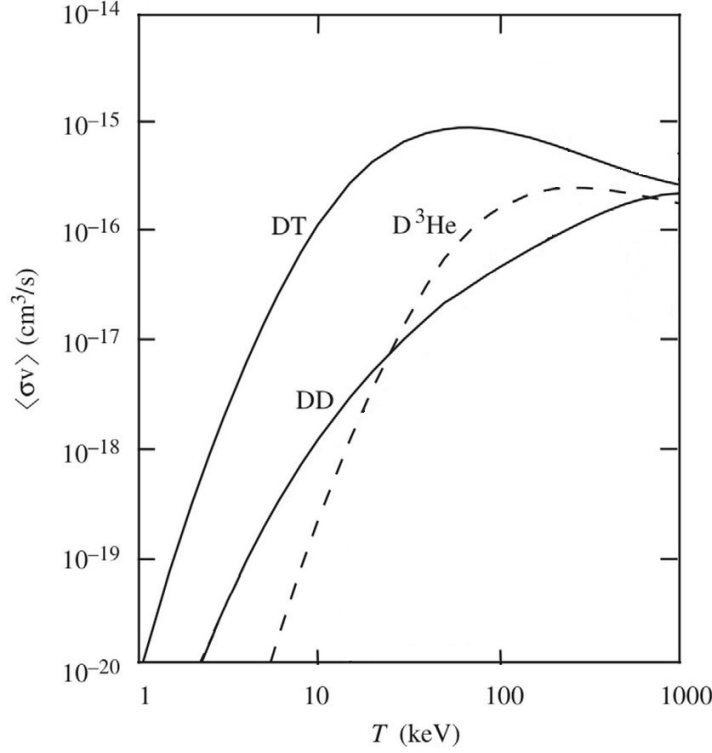
Figure 1.1: The product $\langle \sigma v \rangle$ against the plasma temperature for D-D, D-He^3 and D-T reaction. [70]

power per unit volume is given by

$$p = n_d n_t < \sigma v > \epsilon$$

where ϵ is the energy released per reaction. Considering that the total ion density is $n = n_d + n_t$ and p is maximised for $n_d = n_t = n/2$, the power per unit volume can be rewritten as

$$p = \frac{1}{4} n^2 \langle \sigma v \rangle \epsilon \tag{1.1}$$

The power generated by fusion is carried by neutrons, which leave the plasma without interactions, and by α-particles, which transfer their energy to the plasma

by collisions. In a tokamak, there is a continuous energy loss, which exceeds the replenished heat from the α-particles. For this reason, additional power heating is required to supply the fuel. When there are adequate confinement conditions inside the plasma, a point is reached where the heating from α-particles is enough to compensate for the energy loss, allowing to remove the external heating and the plasma to sustain itself. This state is named the *ignition condition*. A way to evaluate how to achieve the ignition condition is by using the triple-product

$$nT\tau_E > 3 \times 10^{21} \text{m}^{-3}\text{keV s} \qquad {}^2 \tag{1.2}$$

where n and T are the electron density and temperature and τ_E is the *energy confinement time*. This latter is the ratio between the total energy in the plasma[3], $W = 3\overline{nT}V$, and the difference between the power loss, P_L, which is normally balanced by externally supplied heating, so

$$\tau_E = \frac{W}{P_L} = \frac{W}{P_H} \tag{1.3}$$

Therefore, the challenge of nuclear fusion is to confine the heated plasma with enough temperature and density to sustain fusion reactions. Q, the ratio between the power produced and the heating power supplied, is the factor to measure the success in approaching ignition condition

$$Q = \frac{\frac{1}{4}n^2 \langle \sigma v \rangle \epsilon V}{P_H} = \frac{5P_\alpha}{P_H}.$$

The last equality is because the energy released per reaction (ϵ) is five times the α-particles energy. When the production of power and the heat power supplied are equal (*break-even point*), then $Q = 1$, whereas at ignition $P_H \to 0$ and hence $Q \to \infty$.

Nowadays, there are two ways to confine the plasma: increasing the temperature and density, the Inertial Confinement path [42], or confining particles enough time to make possible multiple interactions, the Magnetic Confinement Fusion, which is the objective of this manuscript.

1.2.1   Magnetic confinement: tokamak system

The basic idea of magnetic confinement is to confine the plasma, which is made of charged particles, using an external magnetic field: in the volume defined by

---

[2]This relation is reminiscent of the Lawson criterion of the early days of fusion research.

[3]The average density of plasma particles is $3/2T$ and, considering an equal number of electrons and ions, the plasma energy per unit volume is $3nT$.
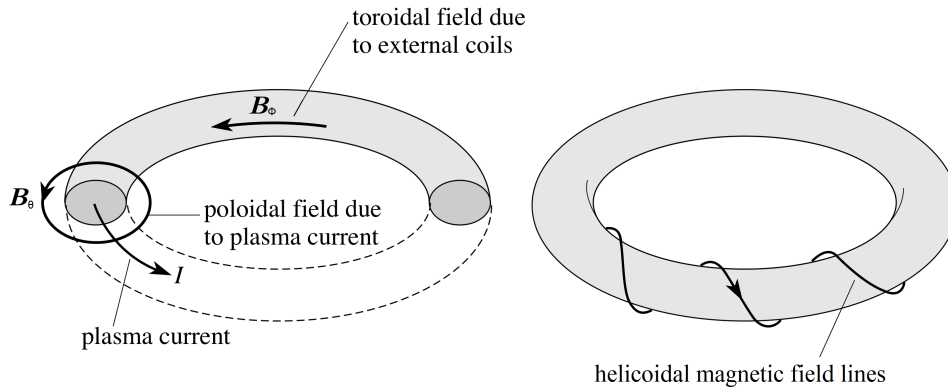
Figure 1.2: Combination of $\vec{B}_\phi$ and $\vec{B}_\theta$ cause field lines to twist.

$\vec{B}$, particles engage in multiple interactions, generating fusion events. The *toka-mak*, Russian acronym of "toroidal chamber with magnetic coils", represents one of the most advanced and studied fusion concepts thanks to its promising results obtained over time. This configuration reached the parameters needed for fusion, even if not yet all together and for a sufficient time. The tokamak is a toroidal system in which the plasma is confined by two magnetic fields, one in the toroidal and one in the poloidal direction. The toroidal field, $\vec{B}_\phi$, is the most intense and external magnetic coils produce it, while the poloidal field, $\vec{B}_\theta$, is mainly produced by the toroidal current in the plasma. The field combination leads to helicoidal magnetic field lines (see figure 1.2) around which charged particles move in a circular motion, the *gyro-motion*. Field lines lay on nested surfaces called *flux surfaces* on which magnetic flux and pressure are constant. The fusion criteria are reached in the core of the torus plasma where pressure and temperature have maximum values [101].

Several physics processes, not yet completely understood, limit the energy and particle confinement in tokamak devices. The confinement improves with plasma current and decreases with increasing plasma pressure, and experiments stress a correlation between plasma size and energy confinement. Moreover, in tokamak experiments, the energy loss is reduced above a critical heating power, increasing the confinement time τ_E (see equation 1.3). The plasma condition above and below this critical value are named *H-mode* [106] and *L-mode* respectively. H-mode profiles are characterised by the *edge pedestal*, a narrow edge plasma region with significantly enhanced gradients associated with an edge transport barrier. Empirical formulas describe the transition between these two plasma regimes and their
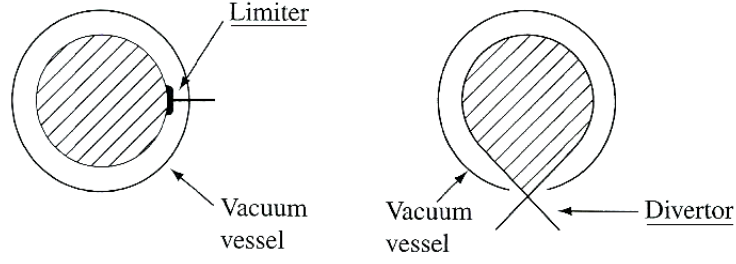
Figure 1.3: Configurations to separate the plasma from the vacuum vessel in the poloidal section of a circular tokamak: the limiter on the left, the divertor on the right. [101]

confinement times [15].

To maintain high-purity conditions and minimise dilution and radiation losses in the tokamak plasma, it is necessary to have a high vacuum and to keep the hot plasma separated from the vacuum vessel. For this purpose, one possible configuration is that of the *limiter*, in which a limiting material target, on which the magnetic field lines impinge, bounds the plasma. However, this solution became less used since the *divertor* configuration has proved more favourable to having good confinement and high-purity conditions. In this one, magnetic field modification keeps the particles away from the vacuum vessel to create the so-called *X-point*. The region of closed magnetic surfaces is separated from the open ones, so, unlike the limiter configuration, impurities should not be able to enter the closed surfaces before ionising and being brought back to dedicated targets. Moreover, this configuration efficiently redirects plasma losses to a dedicated area of the vacuum vessel capable of sustaining high energy and particle fluxes (see section 1.3.1 for more details). The two configurations are illustrated in figure 1.3.

1.2.1.1 Tokamak reactor

The structure of a future tokamak reactor will be very complex. A blanket envelopes the plasma within the vacuum vessel with two crucial roles: absorbing the neutron energy (14.1 MeV) to convert it into heat and breeding tritium to fuel the reaction. For this reason, the blanket is composed of a lithium compound that, reacting with neutrons, produces tritium:

$$^{7}Li + n_{fast} \rightarrow {}^{4}He + T + n_{slow} - 2.5 \text{ MeV}$$

$$^{6}Li + n_{slow} \rightarrow {}^{4}He + T + 4.8 \text{ MeV}$$
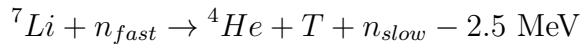
A neutron multiplier like beryllium or lead ensures a breeding ratio greater than a unit. Despite the blanked absorbs most of the neutrons, placing an external shield
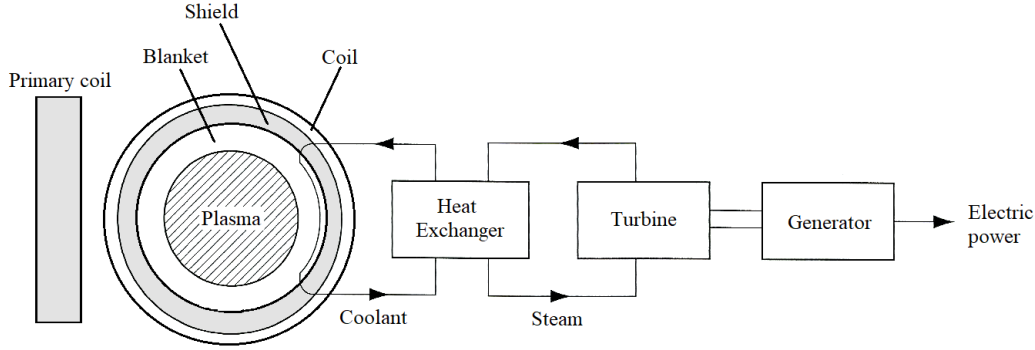
Figure 1.4: Layout of principal components in a tokamak reactor. [101]

of high Z material is necessary to prevent radiation damage and heating of the magnetic coils. A central transformer drives the toroidal current inside the torus. However, more than the inductive current is needed for long-pulse or steady-state operation. External sources like radio-frequency waves are used, and the non-inductive current[4] sources are maximised to overcome this issue. Finally, a fluid coolant extracts the heat produced in the blanket by the reactions and transforms it into electrical power by conventional means. Figure 1.4 shows a sketch of the principal components of the tokamak reactor.

To define size and input parameters for a reactor, the following considerations must be made.

- The confinement time τ_E has to be long enough to satisfy the power balance. Unfortunately, it is not possible to have an analytical scaling[5], but there are ad hoc empirical formulas for each operation regime. The scaling for two cases is useful to have an idea of the quantities involved: L-mode, equation 1.4, and H-mode in inter-ELMs phase, equation 1.5.

$$\tau_E = 0.048 \frac{I^{0.85} R^{1.2} a^{0.3} k^{0.5} (n/10^{20})^{0.1} B_\phi^{0.2} A^{0.5}}{P^{0.5}} s \quad {}^{6} \tag{1.4}$$

$$\tau_E = 0.053 \frac{I^{1.06} R^{1.9} a^{-0.11} k^{0.66} (n/10^{20})^{0.17} B_\phi^{0.32} A^{0.41}}{P^{0.67}} s \tag{1.5}$$

In both cases the confinement time depends on different geometrical vari-

---

[4]The *bootstrap current* is a self-generated current due to plasma pressure anisotropy.
[5]For details, see section 4.1 of [101].
[6]I in MA, P in MW.

ables, minor, major radius (a and R) and elongation k^7 of the plasma, from inputs such as plasma current I, toroidal magnetic field B_ϕ and applied power P, and also from plasma features, like average electron density n and atomic mass of the ions A. [101]

- To avoid detrimental instabilities in the plasma, the current has to be paired with a toroidal magnetic field that is large enough.
  It can be demonstrated that B_ϕ has to satisfy the following:

$$\frac{B_\phi}{B_\theta|_s} \leq 2\frac{R}{\overline{a}}$$

where $B_\theta|_s$ is the mean poloidal magnetic field at the plasma surface and $\overline{a}$ is the mean radius of the plasma. [101]

- To have efficient confinement and to avoid major plasma instabilities, the ratio of kinetic to magnetic pressure inside a tokamak

$$\beta = \frac{2\mu_0 p}{B^2}$$

should stay below the Troyon limit [96]

$$\beta_{max} = \frac{I\beta_N}{aB_\phi} \quad \text{with } \beta_N \sim 2.8$$

Here I is the total current, B_ϕ the toroidal field at the centre of the plasma, a the minor plasma radius in the equatorial plane, β_N is the normal beta value. This limit is based on numerical simulations but experimental validation made the Troyon limit a figure of merit to evaluate tokamak performances stability [34].

- The critical field of the conductors and magnetic stresses on the coil limits the toroidal field.
  For example, if we consider to have around 12 T, as planned for ITER (see section 1.2.1.2), at the centre of the plasma will be 6 T, considering that $B_\phi \propto 1/R_{tokamak}$. In this condition, R would be between 11 m and 5.5 m, with a between 3.5 m and 2 m. For the sake of completeness, we point out the existence of the SPARC project, a compact high-field superconducting tokamak, designed to have 12.2 T in the centre of the plasma with $R = 1.85$ m and $a = 0.57$ m [20].

Superconducting magnets allow for a high magnetic field, long pulse duration and reduced energy load for the power supply systems. However, many other physical
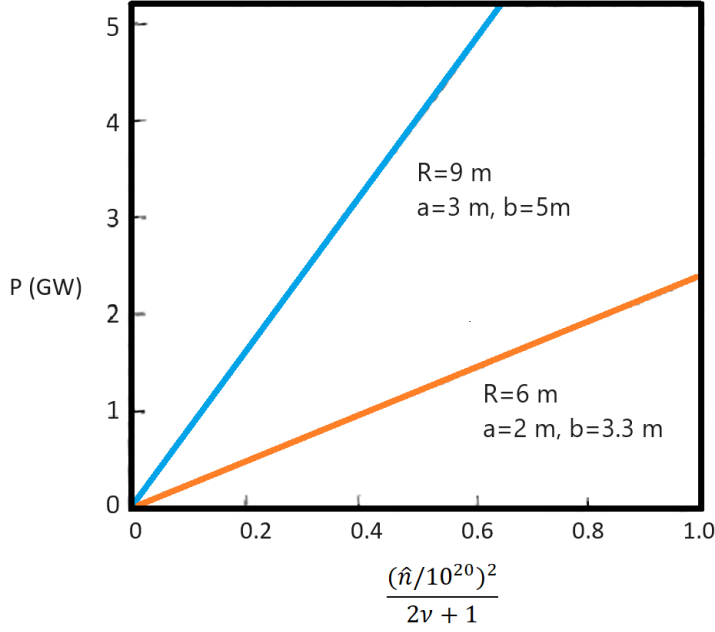
Figure 1.5: Dependence of P on the peak of density $\hat{n}$ and the pressure profile shape index ν for two reactor sizes at $\hat{T} = 20$ keV. [101]

and engineering constraints besides the simple approach described here must be considered when designing a tokamak-based fusion reactor.

To conclude, we would like to estimate the power produced by a tokamak reactor. Using equation 1.1, the total power results will be

$$P = \frac{\pi}{2}\epsilon \int n^2 \langle \sigma v \rangle R\, \mathrm{d}S$$

where $\mathrm{d}S$ is an area element of the poloidal cross-section. From this expression, it is possible to derive a simplified one by making some approximation, like considering simplified pressure profile and the expression of $\langle \sigma v \rangle$ valid for the temperature of 10-20 keV[8]. This expression enables us to have an idea of the power developed given geometrical parameters:

$$P = \frac{0.15}{2\nu + 1}Rab\left(\frac{\hat{n}}{10^{20}}\right)^2 \hat{T}^2$$

Here ν is the pressure profile shape index, b and a are the half-height and half-width of the plasma, and $\hat{n}$ and $\hat{T}$ are the peak density and temperature. Figure 1.5 shows

---

[7]The elongation is defined as $k = b/a$, where b and a are the half-height and half-width.

[8]See [101] for details.

that considering reasonable values of R, a, b at $\hat{T} = 20$ keV, the thermal power produced is of the order of GigaWatt. Its precise value depends on the pressure profile and the density, which are, in turn, dependent on stability constraints.

1.2.1.2 Large tokamaks experiments and future devices

 colour blackThe generation of large tokamaks started operations in the 1980s and 1990s, supported by wide-ranging studies on the small and moderate-sized tokamaks. Notable among these devices are TFTR (USA), JET (UK), see section 1.2.1.2, JT-60 (JP), DIII-D (USA), TCV (CH), see section 1.2.1.2, AUG (DE) and Tore Supra(FR). Some of these tokamaks, like TFTR and JET, were specifically designed for deuterium-tritium experiments. Thanks to these advanced tokamaks, fusion research has made significant progress. Milestones include achieving the $nT\tau_E$ criterion to approach the ignition requirements and produce over 10MW of thermal power using D-T fuel. Results are obtained thanks to their increased size and power capability. Moreover, considerable improvements have been made in fuelling and pumping systems, power handling surfaces, control techniques, and sophisticated diagnostic systems.

The successful development of tokamaks technology has brought us to a stage where an experimental reactor's general requirements and features can be extrapolated. The generation of large tokamak has demonstrated the ability to nearly balance losses with the generated fusion power. However, the International Thermonuclear Experimental Reactor (ITER), shown in figure 1.7, wants to take a significant step forward. It is designed to achieve an energy gain (eq. 1.2) at least in the range of 5-10 (as depicted in figure 1.6) and demonstrate the scientific and technological feasibility of fusion power. It was first conceived in the late eighties, and after several design revisions, it is now entering the final phase of construction in Cadarache (FR). The main goals of ITER are:

- achieving $Q = 10$ (see section 1.2) with a burn time of 200-300 s
- to demonstrate non-inductive steady-state operation at Q=5 and pulse length up to a thousand seconds
- test first wall materials
- demonstrating tritium breeding

ITER will also test some technology solutions for a full-scale fusion reactor, such as superconducting coils, remote handling and the divertor design.

In this context, the large tokamak Tore Supra (now upgraded to WEST) played an essential role in the definition of ITER. It was the first tokamak to implement superconducting magnets successfully and actively cooled plasma-facing components, exploring the physics of long-duration plasma pulses [1]. A pivotal role now
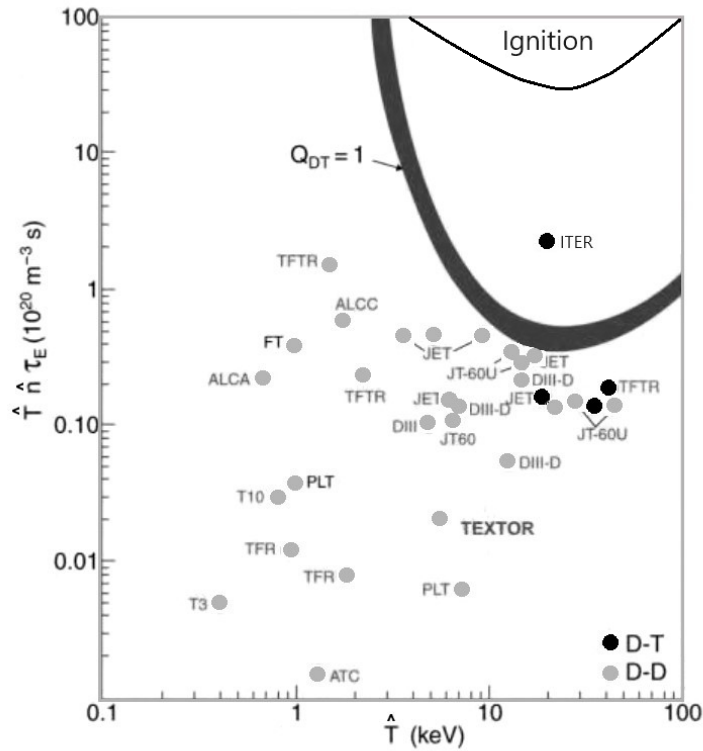
Figure 1.6: Q_{DT} values reached by tokamaks experiments. $\hat{n}$ and $\hat{T}$ are the peak density and temperature, P_H is the additional external heating power.
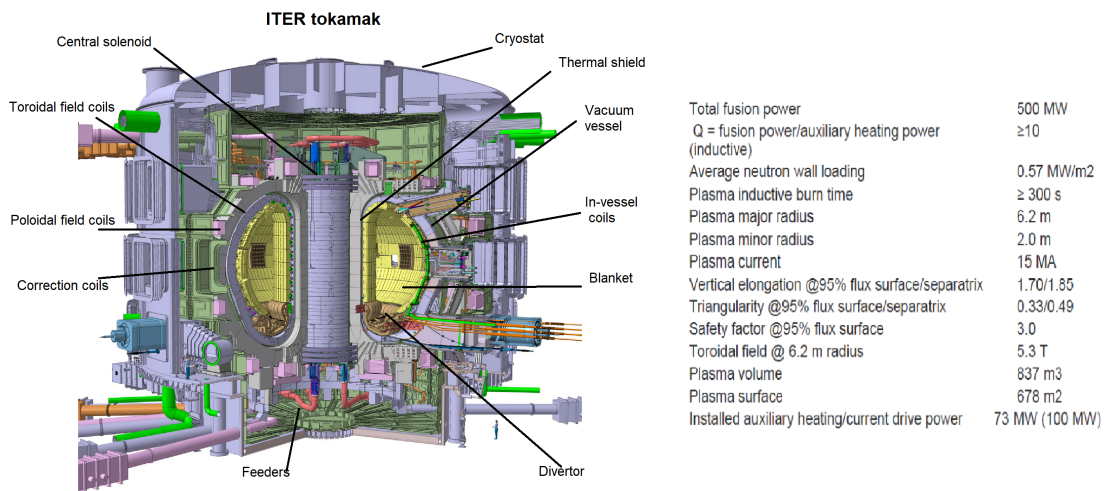

Figure 1.7: Main parameters and features of ITER.

	DTT	ITER	DEMO
R (m)	2.19	6.2	9.1
a (m)	0.7	2	2.93
A	3.1	3.1	3.1
I_p (MA)	5.5	15	19.6
B (T)	6	5.3	5.7
Heating P_{tot} (MW)	45	120	460
P_{sep}/R (MW/m)	15	14	17
Pulse length (s)	95	400	7600

Table 1.1: Comparison among DTT, ITER and DEMO. [22]

will be played by the Divertor Tokamak Test facility (DTT), a fusion experiment currently under construction in Frascati (IT). Its main objective is to explore innovative solutions to handle the power released to the divertor and to extract the heat generated by the fusion process. The divertor has to withstand harsh conditions and is one of the most critical components of a fusion system. While different solutions for the divertor have been investigated in present experiments, it remains uncertain if these solutions can be applied to future devices which will have significantly higher fusion power density. To address these challenges, DTT aims to investigate new divertor configurations and materials under conditions relevant to a fusion power plant. DTT is part of the strategic vision towards generating electrical power through the Demonstration Fusion Power Plant (DEMO) by 2050 [22]. A Comparison among DTT, ITER and DEMO features is shown in table 1.1.

DEMO is the next step in the fusion roadmap [68]. Its primary objective is to demonstrate the ability to control a more powerful plasma, safely generate electricity and enable regular, rapid, and reliable plant maintenance. The main requirements for DEMO are its capability to generate 300-500 MW net electricity for the grid and to operate with a closed fuel cycle. A robust conceptual design is crucial to meet these demands. For this reason, it is necessary to carefully select the appropriate breeding blanket and divertor concept, ensure that all maintenance tasks can be carried out remotely using manipulators, and address nuclear safety concerns. The successful realisation of DEMO will be a significant step towards achieving the ultimate goal of practical and sustainable nuclear fusion energy.

The Joint European Torus: JET

The Joint European Torus (JET) is a large size tokamak and has been, until now, the focal point of the European fusion research programme: its success has led to the construction of ITER. JET was the first device to produce controlled fusion

power with deuterium and tritium and holds the tokamak record for fusion power. It was constructed in 1978 with the main aims to study the α-particles production, the plasma confinement and heating, and the study of plasma-wall interactions. For this last purpose, JET now has an ITER-Like wall (ILW), in which the plasma-facing components are Tungsten and Beryllium. The JET chamber, with major radius R=2.96 m and minor radius a=0.95 m (aspect ratio $\sim 1/3$), has a D-shaped poloidal cross-section, which increases the current limit and provides a natural separatrix formation. It has 16 poloidal copper coils, an iron transformer core and a pumped divertor configuration. The primary source of heating is NBI (Neutral Beam Injection) with a total capability of ~ 35 MW for 20 seconds pulse duration and the ICRF system (Ion Cyclotron Resonance Frequency) with a power capability of about 10 MW. In chapter 5 is presented work done using JET experiments performed in different divertor configurations.

Tokamak à configuration variable: TCV

TCV is a European medium-sized tokamak which plays a pivotal role in fusion energy research. It has a carbon wall, a major radius of 0.88 m, an aspect ratio of about 4, and a magnetic field of up to 1.5 T. The tokamak incorporates versatile heating systems, many diagnostics, and a modern control system. It has unique shaping capabilities thanks to its highly elongated, rectangular vacuum vessel and a system of 16 independently poloidal-field coils. It has the broadest range of divertor topologies, from the conventional single (SN) and double-null(DN) to all versions of the snowflake concept (SF) and Super-X (SXD). For this reason, exhaust physics, including divertor detachment, heat load dynamics, SOL transport and fluctuations, has a central role in the TCV program. Many TCV studies focus on identifying alternative magnetic geometries for ITER, DEMO and future fusion reactors [19]. In recent years, TCV has been updating, adding in-vessel baffles to have a partially closed divertor, allowing us to reach reactor-relevant neutral density and impurity compression, allowing studying an even wider range of divertor magnetic geometries [27, 77]. In chapter 3 and 4, TCV experiments are used to investigate power exhaust behaviours of two alternative configurations: the Negative triangularity shape and the Super-X divertor concept.

1.3   The power exhaust problem

Plasma exhaust (PEX) has been identified as a significant challenge for realising magnetic confinement fusion. The plasma exhaust problem arises from a substantial disparity in the plasma energy transport across and along the magnetic field lines. The magnetic field acts as excellent thermal insulation, causing low effective heat diffusivity across the magnetic field. In contrast, high-speed heat transport is allowed along the open field lines, leading to the power depositing in a very small area. To reduce this problem and avoid material melting, a magnetic configuration called *divertor*, see section 1.3.1, was developed to have a large temperature drop along the length of the SOL and low plasma temperature at the targets. Nevertheless, as tokamak size and pulse length duration increase, managing power exhaust becomes even more challenging. For future devices, with power losses of hundreds of MegaWatts, this results in power fluxes at the divertor targets that exceed the current technological material limit of ~ 10 MW/m^2 [62]. The detachment regime (section 1.3.1.2) and different advanced divertor approaches are currently being explored on existing devices to address this issue. These approaches can enhance divertor radiation without causing excessive core degradation. Another critical concern for upcoming tokamak devices is the occurrence of *type-I ELMs* (Edge Localised Modes), which can potentially induce significant, uncontrolled heat fluxes at the machine PFCs, leading to confinement deterioration. Consequently, different techniques and alternative magnetic configurations are under investigation to mitigate or avoid these phenomena (section 1.3.2).

1.3.1   The divertor configuration

The *divertor* is formed by diverting the poloidal magnetic field (B_θ) by using the external coil to have a current parallel to that of the plasma. In such a way, a magnetic separatrix with B_θ equal to zero at one point (or more) called X-point is created [87], see figure 1.8. The magnetic surface passing through the X-point is called *separatrix* or LCFS (Last Close Flux Surface), and the volume below the X-point between the two divertor legs is named *private flux zone*. This particular volume is normally at low temperature and density, so particles that reach this region do not come from the main centre plasma but from the divertor legs or after being recycled by the wall. The divertor configuration decouples the confined thermonuclear plasma, the *core*, from the plasma interacting with the wall through a region of open field lines, the *Scrape-Off Layer* (SOL). This region is so called because the charged particles entering this zone are scraped off from the plasma and directed to specifically designed plates because of the difference between transport along and across the field lines: in fact, in a magnetically confined plasma $v_\parallel \gg v_\perp$. The SOL radial width can be estimated considering, for simplicity, the SOL region
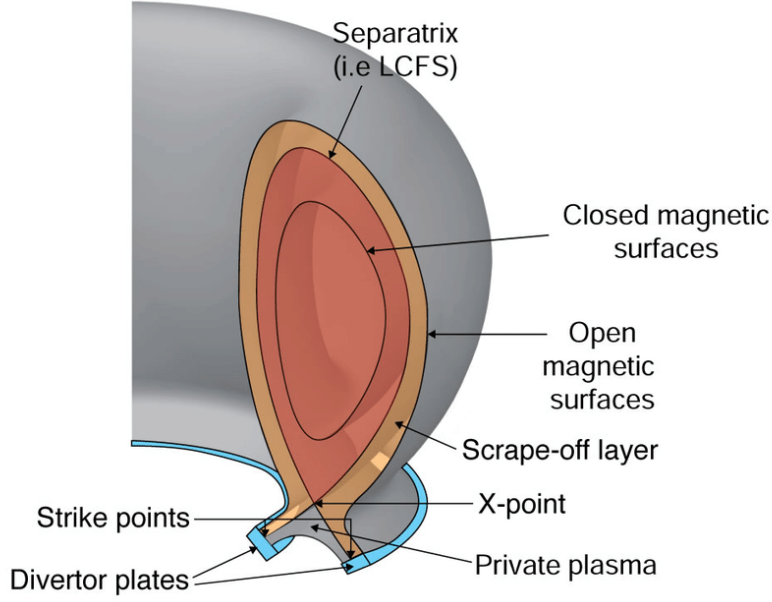
Figure 1.8: Representation of the divertor configuration. [94]

"unfolded" as shown in figure 1.9. Assuming for simplicity that the cross-field particle transport is diffusive[9](Fick's law), the particle source results to be the product between the radial density gradient and a cross-field particle diffusion coefficient ($D_\perp$):

$$\Gamma_\perp = -D_\perp \left. \frac{dn}{dr} \right|_{\text{LCFS}} = -D_\perp \frac{n}{\lambda_{\text{SOL}}}$$

The cross-field flux particles can also be written as $\Gamma_\perp = nv_\perp$ obtaining that

$$\lambda_{\text{SOL}} = \frac{D_\perp}{v_\perp}$$

The lifetime of particles in the SOL will be of the order of the parallel loss time, $\tau_\parallel = L/c_s$. Here, L is the connection length, typically considered as the length of the particle trajectory along the LCFS from the mid-plane of the plasma (*upstream*) to the target, and the sound speed, c_s, is the speed that particles have entering in the Debay sheath[10]. On the other hand, the time spent in the SOL can also be calculated perpendicular to the field, such as $\tau_\perp = \lambda_{\text{SOL}}/v_\perp$. Considering $\tau_\parallel = \tau_\perp$,

---

[9]This assumption is made in the Two-point model described in details in section 1.3.1.1.

[10]The Debye sheath is a layer in a plasma with a significant density of positive ions that balances an opposite negative charge on the surface of a material with which it is in contact.

the width of the SOL can be expressed by the following:

$$\lambda_{\text{SOL}} = \left(\frac{D_\perp L}{c_s} \right)^{\frac{1}{2}} \tag{1.6}$$
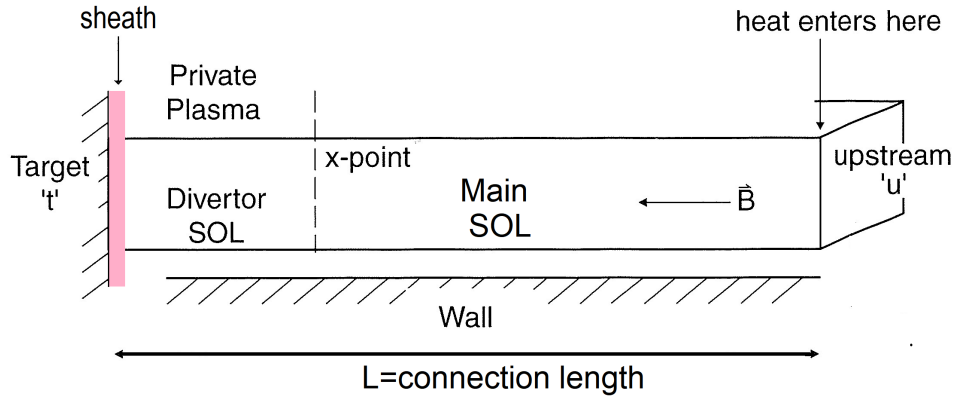
1.3.1.1   The two-point model

Figure 1.9: Representation of the "unfold" SOL.

The divertor SOL can be described by a simple analytic model called *the two-point model* [74, 88]. The Two-point model is a simplified treatment of the SOL with significant limitations and relies on assumptions that are not always valid. Despite this, its simplicity allows a broad understanding of dependencies between quantities in different divertor regimes. It has to be clear that its use must be limited to qualitative analyses while keeping its limits of validity in mind.

The *two* reference points of the model are the *upstream*, *u*, which is normally considered the mid-plane of the tokamak poloidal section, and the *target*, *t*. The main variables used in the model are the plasma density and temperature and the heat $q_\parallel$, which is the power density that flows in the SOL parallel to the magnetic field. This basic model neglects the variation of these three quantities across the SOL. Let now see in detail the three equations of the model: the relation between heat and particle flux (eq 1.7.), the pressure balance (eq. 1.10) and the temperature relation (eq. 1.11.

The model assumes that the only energy and particle sink is the target and that the divertor is *opaque*, i.e. the neutrals recycling from the divertor are all ionised in the *recycling region*, a thin layer in front of the target. Using the Debye sheat

theory, **the relation between heat and particle flux** transported through the sheat results to be

$$q_\parallel^{sheat} = \gamma n_t k T_t c_s \tag{1.7}$$

where γ is the heat transmission coefficient, n_t is the plasma density at the target, k is the Boltzmann constant and c_s the ion acustic speed in the sheath.

It is possible to define the pressure balance assumed by the model between the upstream and the target, starting from the conservation of the momentum. For a plasma specie s, provided by a charge q_s in a magnetic and electric field ($\vec{B}$ and $\vec{E}$) and with velocity v_s, we have

$$\nabla \cdot \Pi_s = n_s q_s (\vec{E} + \vec{v_s} \times \vec{B}) + \vec{S}$$

where $\vec{S}$ is the source of momentum and Π is the total pressure tensor. This latter is defined for each species as

$$\Pi_s = p_s I + n_s m_s \vec{v_s} \otimes \vec{v_s} + \pi_s$$

where p_s is the isotropic pressure and π_s the stress tensor. The two-point model assumes no sources or sinks of momentum in the SOL; therefore, $\vec{S}$ and π_s can be neglected. In the direction parallel to $\vec{B}$, named x, the equation becomes

$$\frac{d(p_s + n_s m_s v_{s,\parallel}^2)}{dx} = n_s q_s E_\parallel$$

and for a plasma of hydrogen, in which the momentum conservation involved both ions and electrons

$$\frac{d(p_i + p_e + n_i m_i v_{i,\parallel}^2 + n_e m_e v_{e,\parallel}^2)}{dx} = e E_\parallel (n_i - n_e) \tag{1.8}$$

Given that $m_i \gg m_e$, assuming the quasi-neutrality ($n_e = n_i = n$) and taking into account the validity of ambipolarity in the plasma edge, where both species drawn towards the targets, $J_\parallel \sim 0 \Rightarrow n_i v_{i\parallel} \sim n_e v_{e,\parallel}$, equation 1.8 becomes

$$p_i + p_e + n m_i v_\parallel^2 = const \tag{1.9}$$

Rewriting eq. 1.9 in terms of the pressure for Maxwellian species [33] and of the Mach number[11], we obtain

$$p_i + p_e + n m_i v_\parallel^2 = n(k T_i + k T_e) + n m_i M^2 c_s^2 =$$
$$= n(k T_i + k T_e)(1 + M^2) = const \qquad \text{[12]}$$

---

[11]The Mach number is defined as $M = u/v$, where u is the local flow velocity to the boundaries and c is the speed of sound in the medium.

Finally, considering that M = 0 upstream and M = 1 at the target (Bohm criterion), we obtain **the pressure balance equation** of the two-point model:

$$n_u k T_u = 2 n_t k T_t \tag{1.10}$$

In this simple model, the power in the SOL is considered all entering at the upstream and equal to $P_{SOL} = P_{tot} - P_{rad,core}$, where $P_{rad,core}$ is the power radiated by the core plasma. Friction is not allowed over the entire SOL; hence only conduction carries the parallel power flux density, $q_\parallel = q_{\parallel,cond} + q_{\parallel,conv} \sim q_{\parallel,cond}$, and power arrives at the divertor equal to P_{SOL}. For describing conduction, the model uses the Spitzer and Härm electron heat conduction definition for both ions and electrons:

$$q = -k_0 T^{5/2} \frac{dT}{dx}$$

In a thermalised plasma, $q_{e,\parallel} >> q_{i,\parallel}$ and, so, electron conduction is generally used to describe the transport of the total conducted power

$$q_\parallel \sim q_{e,\parallel} = -k_{0e} T_e^{5/2} \frac{dT_e}{dx}$$

Integrating the equation between the upstream and target positions, it follows that

$$\int_u^t q_\parallel dx = -\int_u^t k_{0e} T^{5/2} dT$$

$$q_\parallel L = -\frac{2}{7} k_{0e} (T_u^{7/2} - T_t^{7/2})$$

where L is the connection length as explained in section 1.3.1. It follows the Two-point model **relation between the temperature upstream and at the target**:

$$T_u^{\frac{7}{2}} = T_t^{\frac{7}{2}} + \frac{7}{2} q_\parallel \frac{L}{k_{0e}} \tag{1.11}$$

A critical parameter for the edge plasma is the *radial power decay length* λ_q (power e-folding distance in the SOL), strictly connected to the quantities defined before. Considering the perpendicular heat flux diffusive, it can be demonstrated the following

$$P_{SOL} \approx A_\perp q_\perp \approx A_\perp n_u \chi_\perp \frac{T_u}{\lambda_T} \tag{1.12}$$

where $n_u \chi_\perp$ is the anomalous heat conduction coefficient, $A_\perp$ is the surface area of the LCFS and λ_T is the radial temperature decay length. It is possible to relate the power into the SOL to the upstream parallel by considering the magnetic topology

$$q_\parallel = \frac{1}{4\pi a k^{1/2} N} \frac{q_{95} P_{SOL}}{\lambda_q} \tag{1.13}$$

where a is the minor radius of the device, q_{95} is the safety factor on the 95% flux surface and N is the number of the X-points. According to the regime in which we are (see section 1.3.1.2), λ_q and λ_T are in relation with a different constant, $\lambda_q = C\lambda_T$, and from previous equalities, the radial power decay length can be obtained:

$$\lambda_q{}^2 = C\frac{\pi R_0 q_{95}}{N}\frac{n_u \chi_\perp T_u}{q_\parallel} \tag{1.14}$$

where R_0 is the major radius of the device.

The model presented here is the simplest one. Power and momentum loss factors can be included to consider volumetric radiation, charge exchange loss, frictional collisions with neutrals (present below $T \sim 5$ eV), viscous forces and volume recombination (active below $T \sim 1$ eV), but this goes outside of our intention to give a general overview of the model. For details about these *modified Two-point models* see references [74, 72, 49].
The Onion-Skin method (OSM) is used to study actual experiments. In this method, the SOL is subdivided radially into tight, constant cross-sectional areas along $\vec{B}$, through which the plasma flows from the upstream to the target. In this situation, the Two-point model can be applied to each flux tube, including the effect of cross-field sources and sinks. The OSM is a reduced approach for carrying out 2D modelling.

1.3.1.2   SOL regimes and divertor conditions

One important goal of the divertor configuration is to avoid targets melting, having in this region a relatively cold plasma. To satisfy this request, combining it with a good condition for density and temperature in the main plasma (criterion 1.2) requires a significant temperature gradient between the upstream and target. Different plasma regimes are possible, but not all have the desired ∇T in the SOL. At low plasma density or high input power [74], the temperature along the SOL is almost constant, $T_u \approx T_t$, and gradients only occur in the direction perpendicular to the sheath. This regime is called *sheat-linear regime* because $n_t \propto n_u$ (linear) and only the sheath influences the transport from the confined plasma inside the separatrix to the solid surface. From the Two-point model equations (eq. 1.7, 1.10 and 1.11), it is possible to derive the following dependencies specific to this regime

$$T_t \propto n_u^{-2/3} \qquad\qquad n_t \propto n_u$$

Fortunately, a substantial parallel temperature gradient can arise in the SOL due to the finite heat conductivity of the plasma. This condition keeps the name of *conduction-limited regime*, and it occurs when $T_u >> T_t$. From the Two-point

model equations (eq. 1.7, 1.10 and 1.11), it is possible to extrapolate the following.

$$T_u = \left(\frac{7}{2}\frac{q_\parallel L}{k_{0e}}\right)^{2/7} \qquad\qquad T_t \propto n_u^{-2} \qquad\qquad n_t \propto n_u^{3}$$

In this regime, the upstream density is a function only of geometry and power entering the SOL, while target quantities strongly depend on the upstream density. Note that low divertor temperature is achievable simply by increasing the upstream density, inducing an "energy dilution": the enhanced particle flux dilutes the energy of the recycling particles, and thus, although the total power density may be the same, the energy carried per particle is strongly reduced. When the electron temperature at the targets is between 10 eV and 20 eV, this regime takes the name of *high-recycling* [74]. However, the radiating zone can be close to the target, causing sputtering[13] of the divertor plate. As the plasma temperature at the target is further reduced, more attractive SOL conditions are achieved. For very low temperatures, few eV, ion-neutral friction and volume recombination become strong, and the divertor reaches the *detached state*. In this case, there is a significant reduction of n_t and T_t, and the plasma is "detached" from the target, reducing erosion and melting of the divertor material structure. To have a detachment regime, one of the major solutions is to seed impurity that enhances the radiation, dissipating the power towards the divertor. The neutral pressure in the divertor volume increases after the detachment onset, which is also beneficial for pumping and thus particle and impurity control [99]. Note that a high level of detachment can be problematic for the core plasma. The cold region can move to the X-point and core, affecting the confinement. For this reason, it is essential to have reasonable control over the position of the detachment front [92].

1.3.2   Advanced configurations

To reduce the radiation fraction in the SOL and access easily to detachment (e.g. requiring lower impurity seeding levels) and good control of the location of the radiation front [52, 51, 55], advanced divertor configurations, an alternative to the conventional axisymmetric poloidal magnetic X-point divertor (SND) [86], have been developed. Some of these are shown in figure 1.10 and will now be explained. The *X-divertor* concept (XD) relies upon a flaring of the field lines near the divertor plates with consequent larger flux expansion[14], which increases the target wetted area and the connection length, lowering the detachment threshold. The

---

[13]Sputtering is a phenomenon in which solid material particles are ejected after energetic particles of plasma or gas bombard the material.

[14]The flux expansion is the ratio between the width of the flux tube at the target and its width upstream.
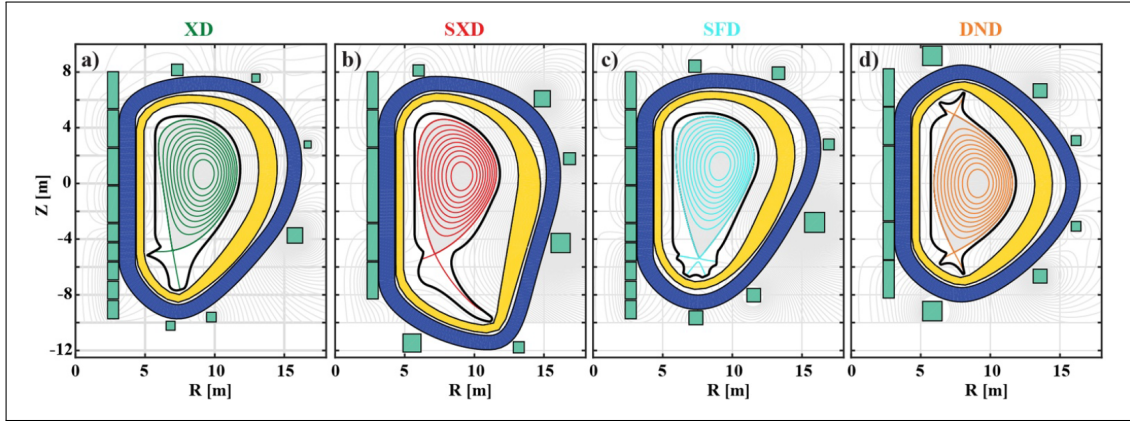
Figure 1.10: example of advanced configurations: (a) SND, (b) XD, (c) SXD, (d) SFD and (e) DND. [76]

Super-X divertor (SXD), discussed in detail in section 4.1, is an extension of the XD in which the major radius, R_t, is increased. The *Snowflakes divertor* (SFD) is characterised by a second-order null point, which leads to a hexagonal symmetry of the separatrix, increasing connection length and SOL volume. Furthermore, turbulent cross-field transport increases, resulting in a broadened λ_q and a lower threshold for the detachment. The *Double Null divertor* (DND) is an up-down symmetric configuration with X-points at the top and bottom with corresponding divertors. The heat fluxes are distributed on two divertor plates at the outer targets with consequently lower peaks; it has an extremely quiescent and squeezed inner SOL, with strongly reduced heat flux onto the inner wall [76].

To mitigate or avoid type-I ELMs phenomena, techniques such as *Resonant Magnetic Perturbations* (RMP) [24] and operating regimes with high ELMs frequency at reduced amplitude [46, 90] have proved to be effective. They avoid PFCs melting and reduce erosion to an acceptable level whilst remaining in a good H-mode performance range (see section 1.2.1). Other studies focus on developing different regimes or magnetic configurations that do not feature ELMs. An example is the *Enhanced D-Alpha H-mode* (EDA), characterised by a prominent edge fluctuation called the quasi-coherent mode (QCM), which enhances plasma transport, allowing high confinement operation without impurity accumulation [35, 32]. Another one is the *Quasi Continuous Exhaust* (QCE) regime, in which high plasma core performance combines with high separatrix density, a key parameter to reach high radiative power losses and divertor detachment [26]. Among others, one of the most promising magnetic configurations that do not feature type-I ELMs is the *Negative Triangularity* configuration that is explained in detail in section 3.1.

To conclude with a practical observation, it is to keep in mind that many of the alternative divertor geometries will come at additional cost, e.g. due to a larger

divertor volume, additional poloidal field coils, new concepts for neutral divertor confinement, and these aspects will be included to evaluate advantages and drawbacks of the various geometries [93].

1.4 General structure of the work

One major challenge for future fusion reactors revolves around managing the intense heat flux that impacts the first wall divertor plates, where most power load concentrates. This study focuses on edge, Scrape-Off Layer (SOL) and divertor plasma to contribute to developing the best scenarios for current and future machines. Different and alternative magnetic divertor configurations are studied with the help of the edge code SOLEDGE2D-EIRENE, and analyses with SOLEDGE3X have also started. The work of these three PhD years is organised in four parts below. Chapter 2 illustrates the edge codes SOLEDGE2D-EIRENE and SOLEDGE3X used to make our studies.

Chapter three is dedicated to the studies done in negative triangularity configuration using TCV pulses and SOLEDGE2D code. The final aims of this work are to understand the energy and particle edge transport of this D-shape and investigate whether it could be a viable alternative from the power exhaust point of view w.r.t. positive triangularity H-mode. The ongoing work with SOLEDGE3X is also presented.

Chapter four is about the study done in Super-X configuration to investigate its potential benefits regarding detachment behaviour. Also, here, TCV experiments and SOLEDGE2D code are used.

Finally, chapter five is dedicated to the study done with SOLEGE2D to understand how to make edge simulations to enhance the existing studies about the relation between electron density at the pedestal and at the separatrix ($n_{e,sep}/n_{e,ped}$) based on experiments. JET experiments were performed in Vertical-Vertical and Corner-Cornern divertor configurations peculiar to this device.

Chapter 2

The SOLEDGE code

To study the edge and SOL physics in tokamaks plasma, different tools have been and continue to be developed. Among recent codes, SOLEDGE stands out thanks to its capability to treat complex geometry of the chamber wall. A refined description of the geometry of the plasma-facing components is fundamental to computing a realistic wall response considering both the particle and energy flux. SOLEDGE is an excellent choice to study any of the presently tested tokamak divertor configurations, and it can work in two modes: 2D transport mode (sec. 2.1) and 3D turbulent mode (sec. 2.2).

2.1 SOLEDGE2D-EIRENE

The multi-species fluid code SOLEDGE2D [13, 14, 18], coupled with the kinetic neutral EIRENE code [78], is specific to study the SOL and divertor plasma. One of its strengths is the capability to model plasma until the wall, a treatment that is not included to date in the other edge codes, such as SOLPS-ITER [102] and UEDGE [79]. The code SOLEDGE2D-EIRENE is particularly suited to study many different edge plasma, including closed divertor geometry or alternative divertor configurations, which is why it was decided to use it for these studies.

SOLEDGE2D investigates the transport of quasi-neutral plasma implementing mass, eq. 2.1, momentum, eq. 2.2, and energy balances, eq. 2.3, derived from the Braginskii's transport equations [8], and evolving density, parallel velocity, ions and electrons temperatures. The balance equations used are the following, in which $\vec{b}$ is a unit vector aligned with the magnetic field $\vec{B}$.

- Mass balance

$$\frac{\partial n_i}{\partial t} + \vec{\nabla} \cdot (n_i \vec{v_i}) = S_{n,i} \tag{2.1}$$

where n_i is the ion density, $\vec{v_i}$ is ion velocity, and $S_{n,i}$ is the source of ions from ionisation and neutrals recombination.

- Momentum balance

$$\frac{\partial}{\partial t}(m_i n_i v_{\parallel,i}) + \vec{\nabla} \cdot (m_i n_i \vec{v_i} v_{\parallel,i}) = -\nabla_\parallel p_i + e n_i E_\parallel + R_{ei}$$
$$+ \vec{\nabla} \cdot (\nu_\parallel \nabla_\parallel v_{\parallel,i} \vec{b} + m_i n_i \nu \vec{\nabla}_\perp v_{\parallel,i}) + S_{\Gamma,i} \tag{2.2}$$

where the second term on LHS is parallel momentum advection, and the RHS is composed from left to right by the parallel projections of pressure force, Lorentz force and the force R_{ei} due to ion-electron collisions; after these, there is the parallel viscous term due to collisions, the turbulent perpendicular transport of momentum and finally the source of momentum due to interaction with neutrals.

- Energy balance

$$\frac{\partial \mathscr{E}_i}{\partial t} + \vec{\nabla} \cdot (\mathscr{E}_i \vec{v_i} + p_i v_{\parallel,i} \vec{b}) = e n_i v_{\parallel,i} E_\parallel + v_{\parallel,i} R_{ei}$$
$$+ \vec{\nabla} \cdot (k_i \nabla_\parallel T_i \vec{b} + n_i \chi_i \vec{\nabla}_\perp T_i)$$
$$+ \vec{\nabla} \cdot (\nu_\parallel v_{\parallel,i} \nabla_\parallel v_{\parallel,i} \vec{b} + m_i n_i v_{\parallel,i} \nu \vec{\nabla}_\perp v_{\parallel,i})$$
$$+ Q_{ei} + S_{E,i} \tag{2.3}$$

where the second term on LHS describes the advection of total energy and the quantities on the RHS are: work of the electric field, work of the ion-electron collision force R_{ei}, the parallel heat conduction, the turbulent perpendicular heat flux, the energy flux due to parallel viscosity, the cross-field energy flux due to perpendicular turbulent viscosity, an internal energy exchange term due to collisions between ions and electrons, and an energy source term due to interactions with neutrals. The electron total energy equation is equal, but the electron kinetic energy is neglected.

From equation 2.1 the evolution of mass is taken. Here, the cross-field particle flux, $\vec{\Phi}_{n,i} = n_i \vec{v}_{\perp,i}$, is a diffusion event:

$$\vec{\Phi}_{n,i} = -D\vec{\nabla}_\perp n_i \tag{2.4}$$

This diffusion term is also called *anomalous transport* due to the fact that cross-field diffusion is experimentally much larger than the pure collisional one. The origin of such a strong transport is plasma turbulences, so the diffusion coefficient in the transport code mimics the turbulence effect. In modelling studies, the diffusion coefficient D is set to match the experimental radial density profile. Since

$\vec{\Phi}_{n,i} = n_i \vec{v}_{\perp,i}$, it is possible to define the perpendicular component of the ion velocity as

$$\vec{v}_{\perp,i} = -D \frac{\vec{\nabla}_\perp n_i}{n_i} \tag{2.5}$$

The evolution of ion parallel velocity is given by the ion parallel momentum balance, equation 2.2. Here, the *diffusion coefficient* ν is not always easy to understand from the experimental radial profiles of ion momentum. In all the studies presented here, it is fixed to an arbitrary flat value to eliminate it somehow between the degrees of freedom. Concerning electrons, $v_{\parallel,e} = v_{\parallel,i}$ because it is assumed ambipolarity. Ion and electron energy balances give the evolution of ion and electron temperatures, equation 2.3. Here, the turbulent perpendicular flux is described as diffusion

$$n_i \chi_i \vec{\nabla}_\perp T_i \tag{2.6}$$

and depends on the *diffusivity* χ_i, which has to be set empirically from radial temperature profiles. The code SOLEDGE2D-EIRENE also implements the vorticity and drifts equations, which are not presented here because our 2D studies do not include them. For details see reference [12].

The code assumes toroidal axisymmetry, and the simulation domain is a poloidal cross-section (2-dimensional domain). The boundary conditions between the plasma and the PFCs are imposed using a penalisation technique [71]. The simulation domain is extended until the solid components where is added a strong particle sink that triggers a supersonic transition of the plasma in a thin layer close to the wall (Bohm–Chodura boundary conditions). The penalisation technique allows the inclusion of interactions of the plasma with the full complexity of the PFCs geometry, which is important to determine the particle influx that can also include impurities.

EIRENE code uses a Montecarlo method launching multiple test particles from neutral source locations, giving in such a way a kinetic description of the neutral behaviour and transport. The velocity, intensity of the source and collision rate for particles are provided from input parameters and atomic data derived from different databases. Considering the kinetic dynamics of each neutral particle allows us to consider the real geometry of the PFCs.

The SOLEDGE mesh is a quadrangle grid aligned with the magnetic flux surfaces. The grid must be capable of seeing all dynamics of interest, so the mesh definition has to be of the same order as the phenomena' typical length. For example, it was said that one important parameter to study the power exhaust is the heat flux decay length λ_q, so it is necessary to have at least 2 or 3 cells in this radial space close to the separatrix to study it. Another important region for PEX study is, of course, the divertor region. Also, a high spatial resolution is required here,
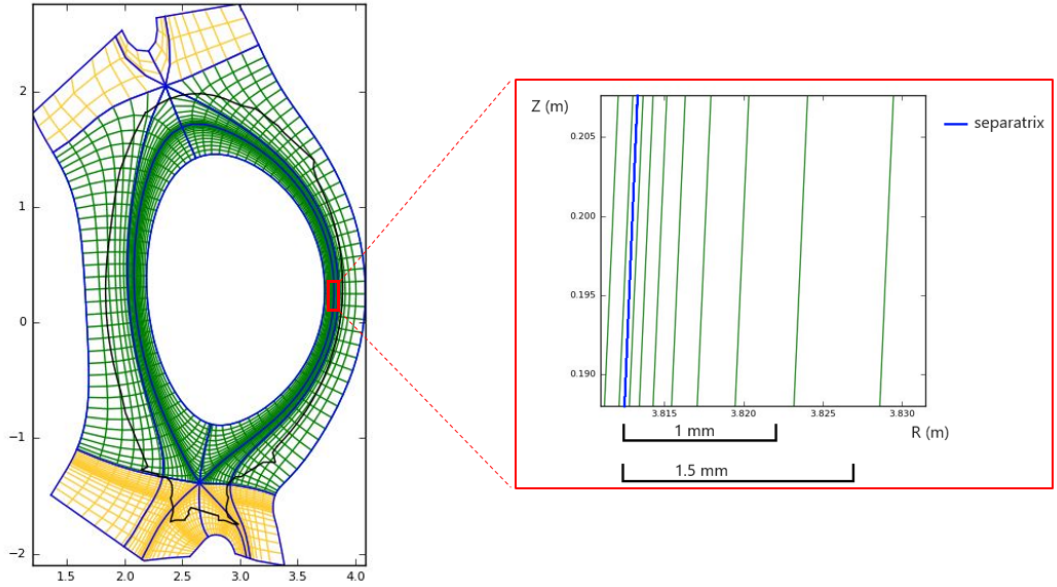
Figure 2.1: Example of SOLEDGE2D mesh for a JET case with a zoom on the cells' definition on the outer mid-plane.

considering the typical mean free path of neutrals in the divertor region that are thermalised with the wall. The definition required here depends on the neutrals' density and can vary from millimetres to a few centimetres. From a computational point of view, the cells' width limits the maximum time step in each iteration of the code. Therefore, a compromise between spatial resolution and time-step is required because too small cells would prevent the simulation from proceeding. The relation between the time step (Δt) and the spatial definition of the cell (Δl) is

$$\Delta t \leq 0.4 \frac{\Delta l}{v} \quad [58]$$

where v is the parallel velocity for the poloidal direction and the perpendicular one for the radial direction; from this relation, it is clear that to have a reasonable time-step (not too small) in the poloidal direction would be better not to have a too high spatial resolution to counteract the high parallel velocity. Figure 2.1 shows an example of the grid made for a JET case. JET λ_q calculated at the outer mid-plane is about 1/1.5 mm in PT H-mode plasma [23]. The mesh has on the outer mid-plane 6/7 cells in one λ_q, which is more than enough to catch the phenomenon of interest. A higher resolution would only increase the computational time without improving the description of the physical phenomenon of interest. More detailed studies about the mesh definition necessary for a reasonable fluid description of the plasma can be found in references [83] and [98]. A good definition is also
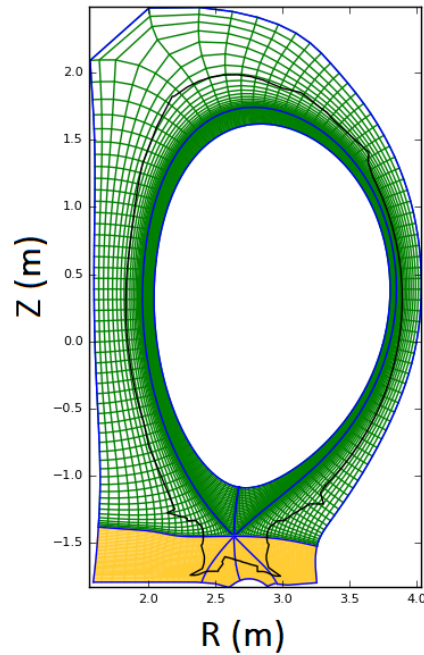
Figure 2.2: Example of SOLEDGE2D mesh for a JET case. The separatrix is the internal blue line, and the black one represents the poloidal section of the vessel (PFCs).

required at the strike points to catch the phenomena of interest. Finally, what this relation shows is that also D and χ have a role in defining the time-step since they are related to the velocity (see eq. 2.5, 2.3 and 2.6). Another example of SOLEDGE2D mesh for a JET case is shown in figure 2.2. To preserve mass and energy conservation between SOLEDGE and EIRENE, an interpolation between the quadrangles mesh and the EIRENE triangles is done.

SOLEDGE2D-EIRENE can cover from the simplest case, pure hydrogen isotope plasma, to more complex cases, including impurities due to wall erosion (W, Be, C, ...) or added to the plasma to radiate plasma power. Of course, including various species requires solving transport equations for each ion level, significantly increasing the computational time.

2.2 SOLEDGE3X

The code SOLEDGE3X [11, 104, 10] is a new code born from the merging of SOLEDGE-2D and TOKAM3X [91]. The code can be used in 2D transport mode, like the previous 2D version (section 2.1), and in 3D first-principle turbulence mode, modelling both large-scale plasma flows and micro-scales turbulent structure

(similar to GBS [37], BOUT++ [105], Grillix [89]). In turbulent mode, the code solves mass, momentum and energy balance for every ion species, vorticity and drifts. Considering that the velocity can be decomposed in $\vec{v} = v_\parallel \vec{b} + v_\perp$, the perpendicular component of $\vec{v}$ could be considered in a diffusive way, in transport mode (eq. 2.5), or can be decomposed in different parts:

$$v_\perp = \vec{v_E} + \vec{v^*} + \vec{v_p} + \vec{v_D}$$

Here $\vec{v_E}$ takes in account the $\vec{E} \times \vec{B}$ drift

$$\vec{v_E} = \frac{\vec{E} \times \vec{B}}{B^2}$$

with $\vec{E} = -\vec{\nabla}\phi$ that is the electric field, $\vec{v^*}$ denotes the diamagnetic drift

$$\vec{v^*} = \frac{\vec{B} \times \vec{\nabla} p}{ZB^2 en}$$

where Z denotes the species charge number, $\vec{v_p}$ is the polarisation drifts, and $\vec{v_D}$ is an effective velocity associated with diffusive processes (anomalous transport). Cross-field diffusivity of particles $D_\perp$, viscosity $\nu_\perp$ and temperature $\chi_\perp$ can take classical values ($\sim 10^{-2}$ m²/s) for turbulent simulations or anomalous values (~ 1 m²/s) for transport simulations, where the cross-field diffusion emulate turbulent transport. Electron density is computed following quasi-neutrality, so $n_e = \sum_i Z_i n_i$.

It also implemented the resolution of the current balance to compute the electric potential, $\vec{\nabla} \cdot \vec{j} = 0$, where

$$\vec{j} = j_\parallel \vec{b} + \vec{j} * + \vec{j_p} + \vec{j_D}$$

Here, on the RHS, there is the parallel current given by the generalised Ohm's law law[85], the diamagnetic current, the polarisation current and the diffusion current. The penalisation technique is the same used in SOLEDGE2D, allowing the domain to be extended until the PFCs also in turbulence treatment. Coupled with the code SOLEDGE3X, it is possible to have two neutral models: a crude fluid model where neutral transport is considered diffusive or EIRENE. As of today, for computational time issues, SOLEDGE3X in turbulence mode uses only the neutral fluid model, which, however, provides a good approximation for the source of plasma generated by recycling as well as power losses by radiation in the divertor that is enough if details of neutral transport are not required. In the future, the possibility to use EIRENE will be implemented [36].

In SOLEDGE3X is implemented a simplified heuristic turbulence model inspired by the "$k - \epsilon$" one, where k and ϵ are the intensity and the dissipation rate of the

turbulence [5, 4]. In the code is considered only k and its evolution, but, despite its simplicity, the model computes self-consistently a map of diffusion coefficients calculated by $D = \tau k$, where the time τ is equal to R/c_s[1]. The evolution of k is described by the following

$$\partial_t k + \vec{\nabla} \cdot (k\vec{v}) = S_k - P_k + \vec{\nabla} \cdot (D\vec{\nabla}_\perp k) \tag{2.7}$$

where $S_k = \gamma_I k$ is the source of turbulence, defined by the linear growth rate of interchange instability γ_I. P_k is a saturation mechanism for turbulence intensity assumed to be $P_k = \alpha k^2$. At steady state, neglecting transport terms in equation 2.7, source and saturation terms must compensate, giving $S_k = P_k$, following that $k = \gamma_I/\alpha$. Combining the $D(k)$ expression and the theoretical SOL width λ_{SOL} (see equation 1.6), we have

$$\lambda_{SOL}^2 = \frac{2\pi q R^2}{c_s^2} \times \frac{\gamma_I}{\alpha}$$

where q is the safety factor. To recover $\lambda_{SOL} = \lambda_{scaling}$, parametrers α has to be proportional to $\lambda_{scaling}^2$ and, considering for L-mode plasma the simple scaling law $\lambda_{scaling} = 4q\rho_L$, we have that $\alpha \propto \rho*^2$, where $\rho* = \rho_L/a$ is the normalized Larmor radius [2]. For more details about the model, see reference [10]. From the k model used, the quadrangle grid of SOLEDGE3X simulations requires more or less a definition of the order of the ion Larmor radius (~ 1 mm) in all the plasma domain. The small cells' width and the more extensive 3D domain in turbulence mode lead to a considerable increase in the computation time to reach a quasi-steady state. No simulation of an experiment in SOLEDGE3X turbulent mode has achieved to date the convergence significant steps have done in the last months [36]. Considering the great potentialities of this code, it was decided to start an experimental analysis, presented in section 3.4.

---

[1] R is the major radius of the device and c_s sound velocity.
[2] ρ_L is the Larmor radius and a the minor radius of the device.

Chapter 3

Negative Triangularity PEX study

One problem for future tokamak devices is the Edge Localised Modes (ELMs) as they can lead to large, uncontrolled heat fluxes at the machine targets, as explained in section 1.3.2. For this reason, different techniques and alternative magnetic configurations are under study to mitigate or avoid these phenomena, managing to have a good core confinement. One of the most promising among these studies is the Negative Triangularity (NT) configuration. In this chapter, the advantages of this alternative plasma shape are described (section 3.1) and the numerical studies done using TCV experiments to understand energy and particle edge transport are presented (section 3.2). One of the objectives of this work is to determine whether this reversed D-shape could serve as a viable alternative in terms of power exhaust compared to the Positive Triangularity H-mode. Section 3.3 is dedicated to studies on that topic.

3.1   The negative triangularity

In PT H-mode plasmas, the confinement is strongly correlated to the height of the edge pedestal [103], which increases with positive triangularity. The triangularity is defined as follows:

$$\delta = \delta_{edge} = \frac{\delta_{top} + \delta_{bottom}}{2}$$

$$\delta_{top} = \frac{R_0 - R|_{Z=Z_{max}}}{a}$$

$$\delta_{bottom} = \frac{R_0 - R|_{Z=Z_{min}}}{a}$$

where R_0 is the major radius of the torus[1] and a is the minor radius, the half-width of the poloidal section on the mid-plane [81]. To maximise the core confinement, the power entering the SOL from the core has to remain above the L-H power threshold, and this power will be convected to the vessel along a very narrow tube, leading to a significantly decreasing lifetime of PFC [56]. Moreover, in this condition, the pedestal region presents a very low transport, developing large radial pressure gradients that can trigger ELMs, which cannot be tolerated in future large tokamaks, e.g. DEMO. Negative triangularity is a promising candidate to avoid these problems among the alternative configurations [48, 60]. It achieves a global confinement comparable with positive triangularity H-Mode operation, although it does not develop an edge transport barrier, thus avoiding type-I ELMs [47]. Moreover, it is not necessary to achieve the power to exceed the L-H threshold, and it could enable an easier power exhaust dissipation due to a more extensive heat flux decay length [84] with a consequent larger plasma−wetted area on the target. Finally, due to the geometrical layout, particularly the more external position of the strike points, it should be possible to have a larger pumping conductance from the divertor. The difference between a conventional D-shape with positive triangularity and NT is shown in figure 3.1.
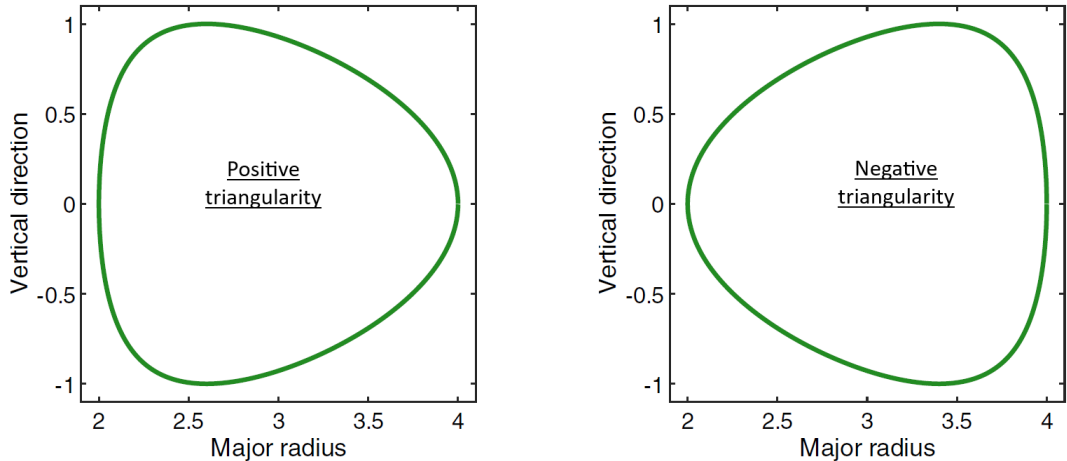

Figure 3.1: Examples of poloidal cross sections used in tokamaks, in arbitrary units, with the torus axis on the left: on the left the *dee or positive triangularity*, on the right *reverse-dee or negative triangularity*. [59]

Different analytical studies [64, 57] and experiments, performed on DIII-D [66, 95], AUG [39] and TCV [31], were and are dedicated to the investigation of the

---

[1]R_0 is the radial distance of the poloidal section centre of the torus from the axis of symmetry of the device.

NT proprieties. Even if the actual literature about NT covers more prominently the core plasma region, thanks to the recent development of integrated scenarios that try to optimise all aspects of a reactor, in the last two years, different works devoted to the scrape-off layer and plasma-wall interactions appeared [59]. Note that because of its promising features, NT is taken into account for future projects such as DTT [2, 43] and DEMO [82].

The work presented here was done within different packages of European Tokamak Exploitation with the specific aim of explaining the effects of negative triangularity on plasma performance in order to extrapolate it to a reactor-scale device. In this context, we aim to study the NT's power exhaust and edge transport behaviours without ELMs to the PT in both L-mode and H-mode. The code SOLEDGE2D-EIRENE, coupled with experiments performed on TCV, is used for this study. The next step, starting now, is to use this modelling tool to predict the behaviour of NT plasmas at reactor scales in terms of compatibility with highly radiative/dissipative scenarios.

Since an official name has not yet been established, we will label the NT state without ELMs as "NT L-mode." However, it is essential to emphasise that this is not a formal definition, and, in particular, NT can not be defined as a *low confinement regime* (L-mode).

3.2   NT L-mode VS PT L-mode

An upper triangularity scan performed in TCV is studied experimentally and using the transport edge code SOLEDGE2D-EIRENE (section 2). Experimental data from Thomson Scattering (TS), Langmuir Probes (LP), bolometry and spectroscopy, as well as modelling results, allow us to understand how triangularity affects particle and heat transport in the edge of the plasma. This study was presented as a poster at the PSI-25 conference 2022 and published in the journal Nuclear Materials and Energy in 2023 [65].

3.2.1   Experiment data set

All the pulses under analysis are in single null magnetic divertor configuration with fixed lower triangularity, $\delta_{bot} = +0.5$, and δ_{up} from -0.28 to $+0.45$. These discharges were used in a previous study about the heat flux decay length [25], allowing us to compare results. In figure 3.2, equilibria given by the magnetic

I_p (kA)	B_T (T)	Te (keV)	Ohmic power (kW)	Area (m^2)	Volume (m^3)	q95	q0
-240	-1.43	0.8	300	0.22	1.2	3–3.2	0.7–1

Table 3.1: Parameters common to all pulses in the time interval of interest. [65]

Pulse #	δ_{up}	$n_{e,avg}$ (x10^{19} m^{-3})	κ	Grazing angle	P_{SOL} (kW)
52789	$+0.45$	4.9	1.59	4.18	268
52785	$+0.28$	5.4	1.64	3.85	263
52787	$+0.04$	5.6	1.59	3.85	261
52783	-0.28	6.5	1.5	4.33	254

Table 3.2: The average electron density, n_e, the elongation, κ, the grazing angle and P_{SOL} are kept fairly constant between discharges with different upper triangularity. [65]

equilibrium reconstruction LIUQE code [40] are shown. All discharges are ohmically heated a nd in L-mode deuterium plasmas in high recycling regime (section 1.3.1.2). The global plasma parameters, shown in table 3.1, are the same for all pulses. Other parameters, such as the mean electron density, n_e, the elongation κ, the grazing angle and P_{SOL}, are fairly constant, allowing us to compare all cases independently of these parameters, see table 3.2. For more details about the pulses, please refer to reference [25].
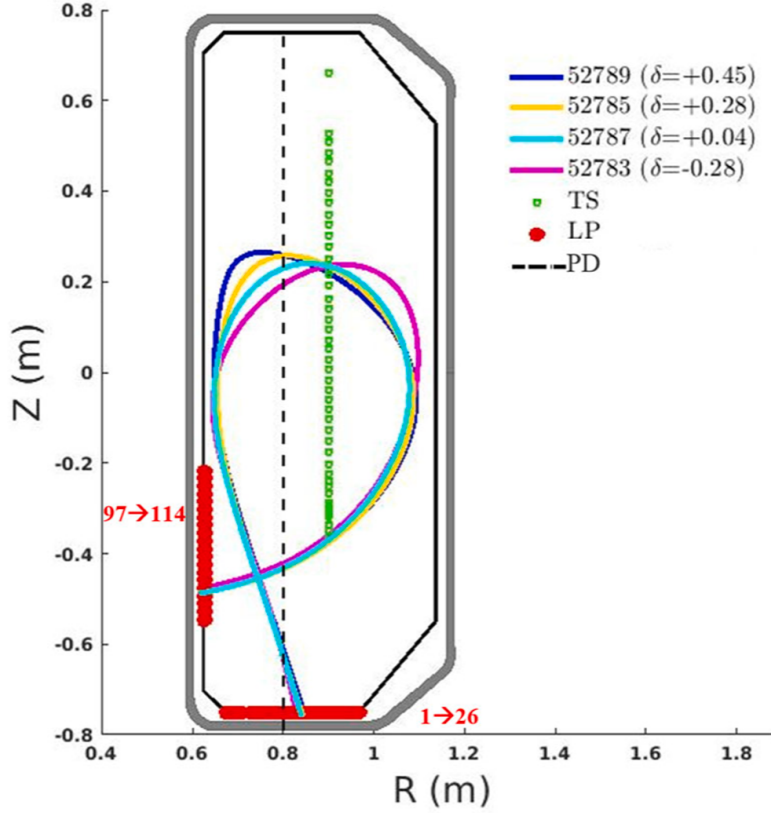
Figure 3.2: Poloidal cross-section of magnetic equilibrium reconstruction for the four pulses with different upper triangularity. In the figure, the locations of the diagnostics used are also shown: Thomson scattering (TS) in green, Langmuir probes (LP) in the divertor region in red and photodiode vertical central line of sight (PD) in dashed black line. [65]

3.2.2 Data analysis

Experimental data can give qualitative information on how triangularity affects transport at the plasma's edge. Figure 3.2 shows the diagnostics used for the following analysis. The H-α emission, typically mainly localised in the divertor region, shows that the deuterium influx changes with δ_{up}. Figure 3.3 shows the emission collected by the photodiode (PD), which intersects the outer leg of the LCFS in the same position for all pulses under analysis (see fig. 3.2), giving information about the region around the outer strike point. At the time studied, the emission decreased going from PT to NT configuration, suggesting a lower particle transport with the decrease of the upper triangularity. The comparison between cases can be done since the average density is mainly the same for all four cases. The emission decrease is also confirmed by the decrease of the ion saturation
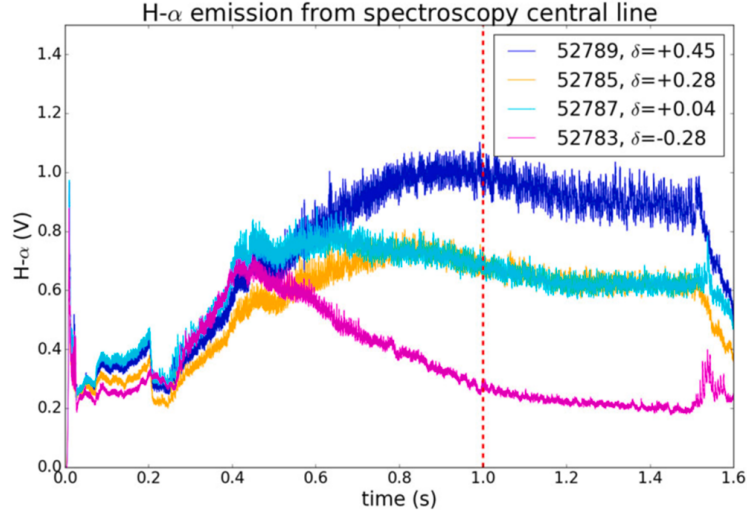
Figure 3.3: H-α emission collected by the PD in a central vertical position for the four pulses. The red dashed line indicates the instant in which the analysis was made. [65]

current ($J_{sat,i}$) collected by Langmuir probes [21] at the targets, with the decrease of δ_{up}. To show clearly this behaviour, the $J_{sat,i}$ dependency on electron density is taken into account with the help of the two-point model (section 1.3.1.1). It is known that $J_{sat,i} \propto n_t \sqrt{T_t}$ and in the high recycling regime $n_t \propto n_u^3$ and $T_t \propto 1/n_u^2$, and so it follows that $J_{sat,i} \propto n_u^2$, where u indicates upstream quantities and t indicates quantities at the target. Because there are no reference data for the upstream electron density, the average values of Thomson Scattering data [6] near the separatrix (around $\rho = 0.98$) was used, which could be considered reliable in estimating the upstream SOL density. In figure 3.4, the integral of the saturation current on targets, divided by n_u^2 and normalised to the maximum of the four cases, is plotted against the upper triangularities. The $J_{sat,i}$ increases with the δ_{up} on both targets, confirming the previous statement based on H-α emission: NT decreases the particle transport in the SOL. Langmuir probe measurements are also analysed to explore the dependency of heat flux decay length on the OMP[2], λ_q, on triangularity. Previous studies made with IRT found an increase of λ_q with the δ_{up} at the outer divertor target, while non-monotonic behaviour at the inner target was seen [25]. Figure 3.5 shows the heat flux measurements collected at targets by LP fitted with a composition between one Gaussian distribution and two exponential functions, figure 3.5a and 3.5b. Data normalised and centred compared to the maximum value of the heat flux (fig. 3.5c and 3.5d) show a non-monotonic trend on both targets. From this first analysis, it would seem that

---

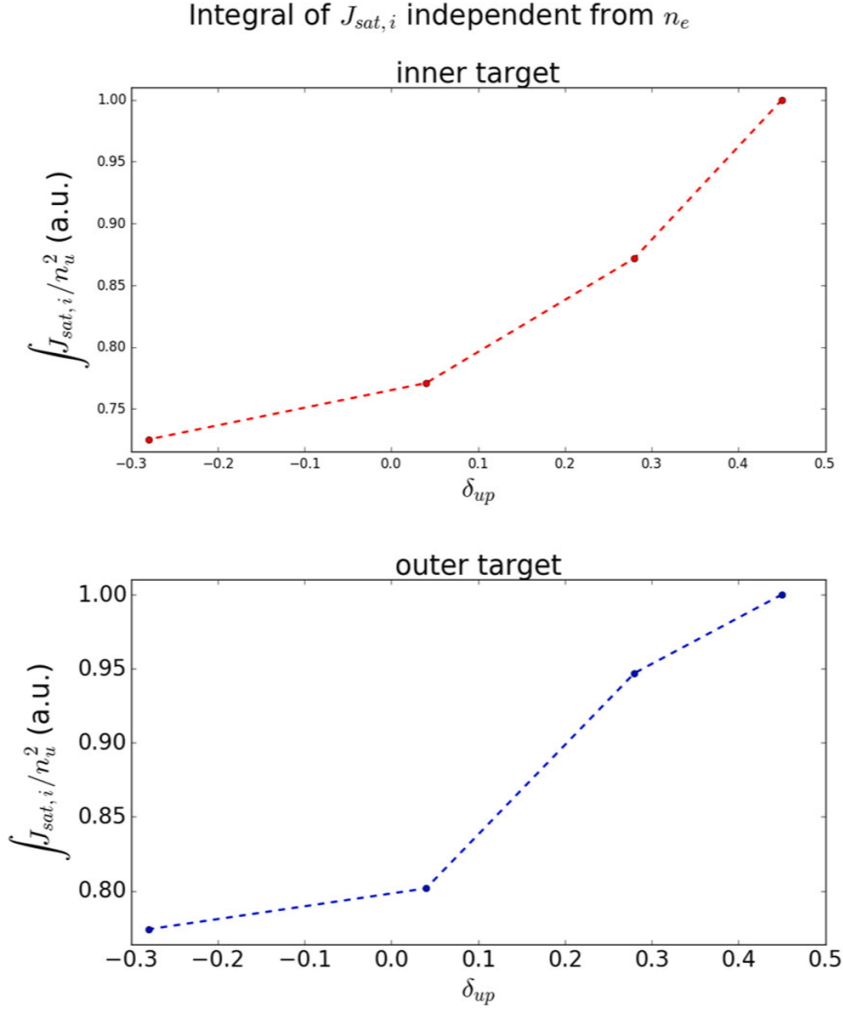[2]Note that this $_q$ is not the conventional one calculated on the divertor target.

Figure 3.4: Integral of the saturation current on targets from LP, divided by n_u^2 and normalised to the maximum, plotted against the upper triangularity, for the inner and the outer target. [65]

LPs do not agree with IRT analysis [25]. However, it must be considered that the heat flux calculated from Langmuir probe measurements might not be accurate enough to see λ_q differences between pulses. On the contrary, in the following section, it will be shown that the edge modelling constraint on the more reliable $J_{sat,i}$ measurements by LP, provides some indication about λ_q differences between pulses.

Experimental data analysis brings us to the conclusion that there is a monotonic decrease in particle transport going toward the negative triangularity.
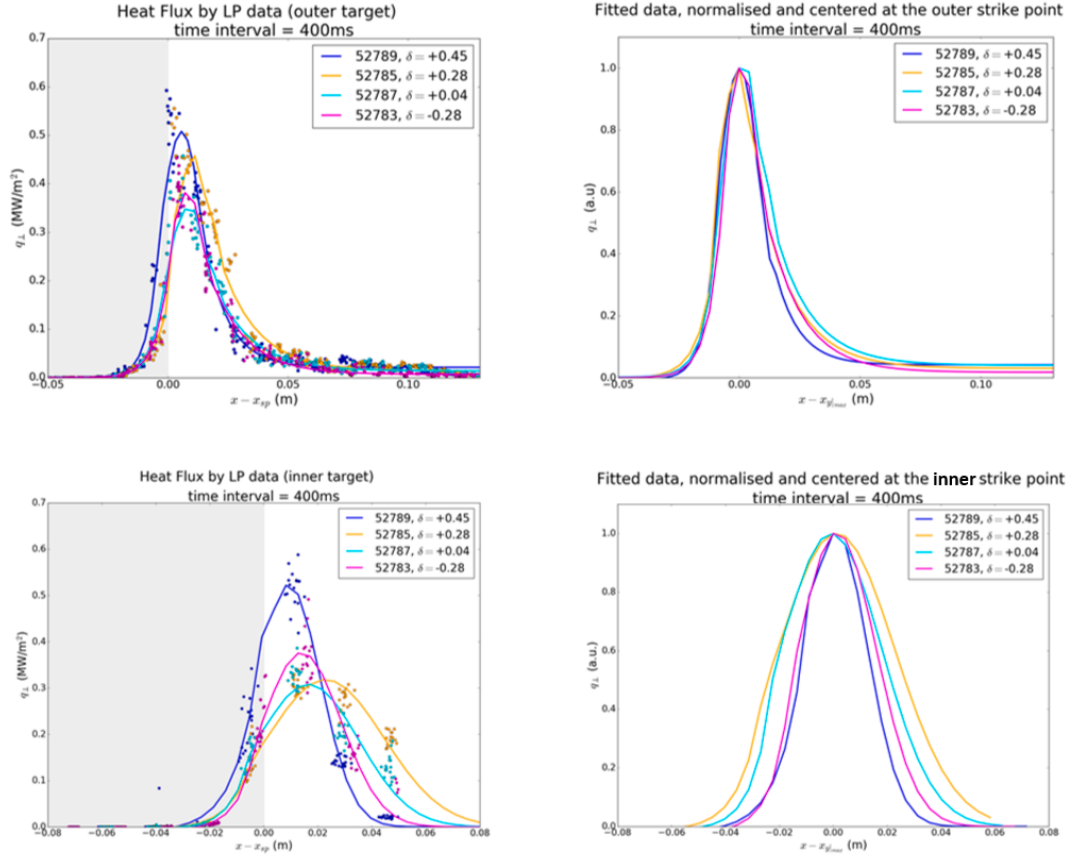
Figure 3.5: Heat flux data by LP with fits on 400 ms time interval: a) on the outer target; b) on the inner one. The private region is coloured in grey. Fitted data normalised and centred compared to the maximum value of the heat flux: c)outer target; d) inner target. [65]

3.2.3   Modelling setup and results

In order to understand edge transport behaviours depending on the triangularity, the code SOLEDGE2D-EIRENE is used. Wall and divertor geometry is the same for all four cases. Figure 3.6 shows an example, for the negative δ_{up} case, of the meshgrid for SOLEDGE plasma fluid solver (fig. 3.6a), which covers all the edge plasma volume extending outside the wall to provide the boundary constraint for the penalisation method. In figure 3.6b is shown the EIRENE meshgrid, which overlays the SOLEDGE one in the plasma domain. In contrast, figure 3.6c shows the locations of the D2 puffing valve and the pump, which does not have a significant role in the particle balance because the TCV carbon wall itself plays the
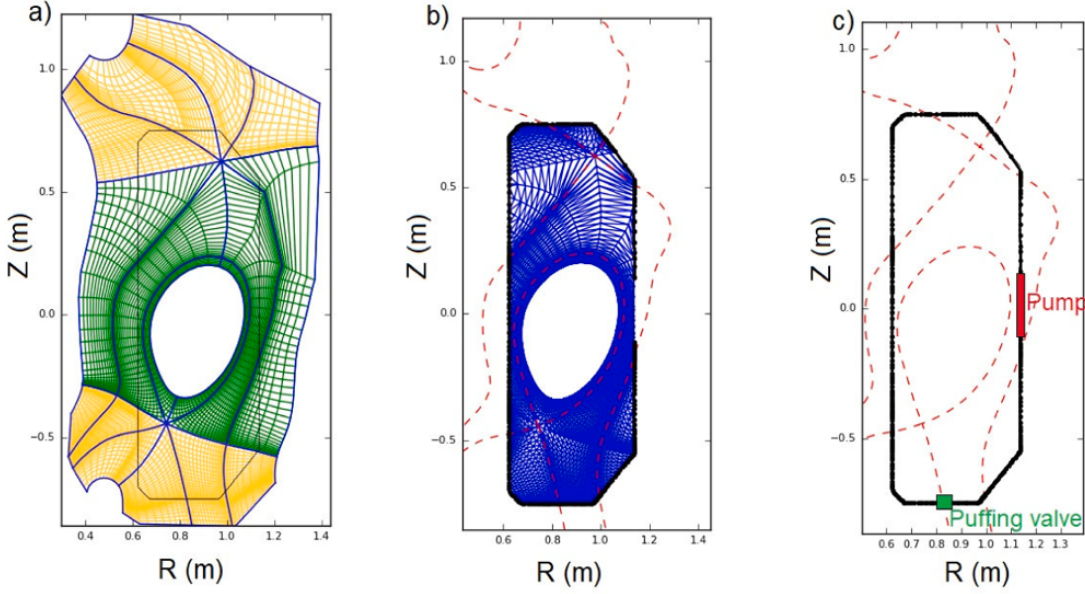
Figure 3.6: Modelling meshes and wall: a) SOLEDGE2D quadrangles fluid mesh; b) EIRENE triangles mesh; c) gas-puffing and pump locations. [65]

major role [101] in the particle balance. The wall recycling coefficient, an input parameter of the code, is adjusted to achieve particle balance with the experimental puffing imposed. It was investigated if the spatial non-homogeneity of the toroidal magnetic field module could have some influences on simulation results, including the normalised $1/B_{toroidal}$ dependency and no effects at all were found. For this reason, the simulations were done without including any spatial magnetic field dependencies in transport values.

Since the modelling domain includes only a negligible portion of the plasma core, P_{SOL} is computed by subtracting from the ohmic heating the radiated power in the core in addition to that due to impurity since simulations are performed in pure Deuterium. Impurity radiation is mostly localised out of the LCFS, and it is mostly due to Carbon because of the carbon wall of the device. All radiation power estimations are based on bolometry measurements [63]. The P_{SOL} values used, shown in fig. 3.1, are split equally between electrons and ions. [30]. Thomson scattering data are used to tune transport profiles. In figure 3.7, an example of the matching between experimental data, which cover only the region inside the separatrix, and modelled profiles are shown for the cases with $\delta_{up} = \pm 0.28$. Transport parameters have been kept radially non-uniform to reproduce LP profiles on the outer target, in particular $J_{sat,i}$, the electron density and the electron temperature. Figure 3.8 shows profiles on the outer target for the negative δ case.
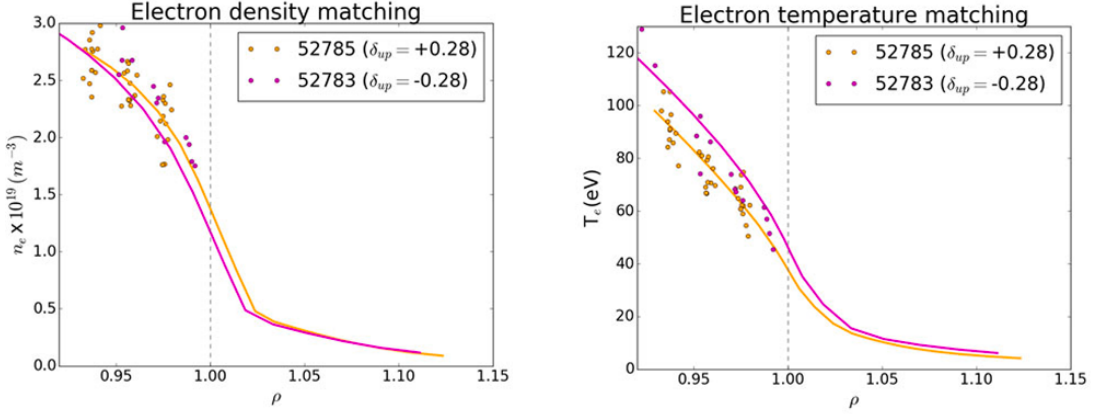
Figure 3.7: Matching between TS data (dots) and modelled profiles (solid line) on the outer mid-plane for cases with $\delta_{up} = \pm 0.28$. [65]
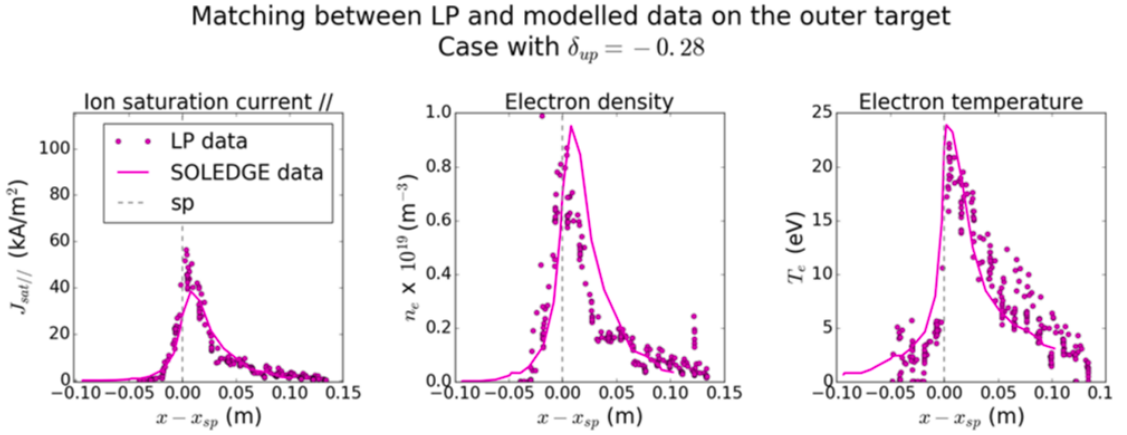

Figure 3.8: Matching between LP profiles (dots) on the outer target and modelled profiles (solid line) for the negative triangularity case. The dashed line in grey indicates the strike point reference. [65]

The transport profiles, which allow to have a good match in shape, and experimental data values are shown in figure 3.9. Focusing inside and at the separatrix, particle diffusion decreases monotonically with δ_{up} from PT towards NT, while the heat diffusion does not show any particular trend. In particular, the negative δ case has the same value $\chi_{i,e} = 1.0$ m^2/s as the two positive cases. Firstly, the same $\chi_{i,e}$ and then D values are used in all cases to investigate if triangularity affects the particle diffusion more than the heat diffusion in the whole near-SOL and not only at the separatrix. In the same-χ cases, the $\chi_{i,e}$ values chosen are that which change out of the separatrix after $\sim \lambda_T$ for all the cases, corresponding to the cyan profile in figure 3.9, while the D values are left in ad hoc shapes. The same-D
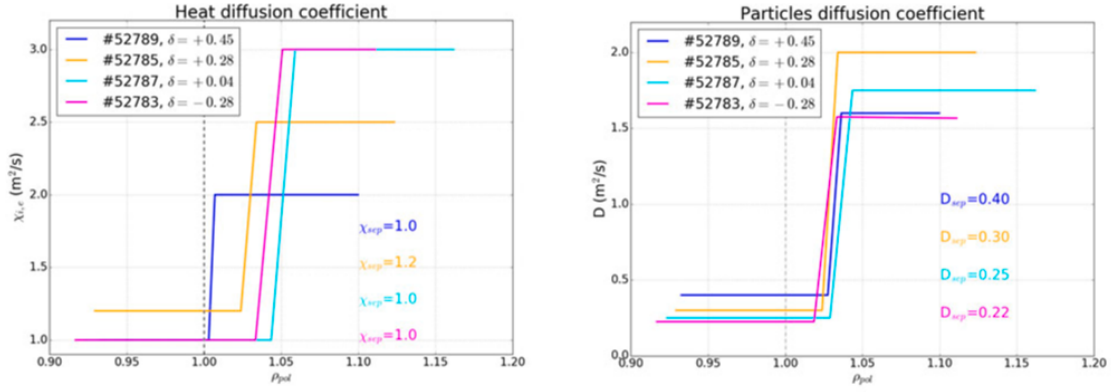
Figure 3.9: Particles and heat transport profiles for the four cases under analysis. [65]

cases follow the same logic, but concerning λ_n, D profile chosen was the one in blue in figure 3.9, and ad hoc $\chi_{i,e}$ are used. Fixing $\chi_{i,e}$, the match between data and simulated profiles is as good as before, see figure 3.10, only a little change in shape is visible, but its investigation is out of our purposes. On the contrary, fixing D, the simulated profiles do not match experimental data as well as before. In particular, the density profile at the outer mid-plane is overestimated, and density and temperature at the outer target are overestimated and underestimated, respectively, see figure 3.11.

It can be concluded that in the analysed cases, triangularity affects particle transport more than energy transport in the near-SOL. In the far-SOL, no particular trend is found, both in particles and heat transport, but note that the experimental data available allow us to focus only on the near SOL. The transport values in the far SOL were chosen to increase the diffusion to help match the LP data on the targets, but real values could be different.

The good match between profiles on the targets allows a reliable estimation of the heat flux decay length by SOLEDGE2D-EIRENE. Figure 3.12 shows λ_q calculated by fitting the outer mid-plane $nT^{3/2}$ profile that, as for the conventional λ_q calculated at the divertor target obtained by using IRT [25], shows a monotonically increasing trend with δ_{up}.

3.2.4 Section conclusions

The work presented here allowed us to characterise the edge transport in upper Negative Triangularity discharge, confirming that the NT affects not only the core transport but also edge transport. Experimental data were analysed directly, and the edge transport code SOLEDGE2D-EIRENE was used to investigate particle
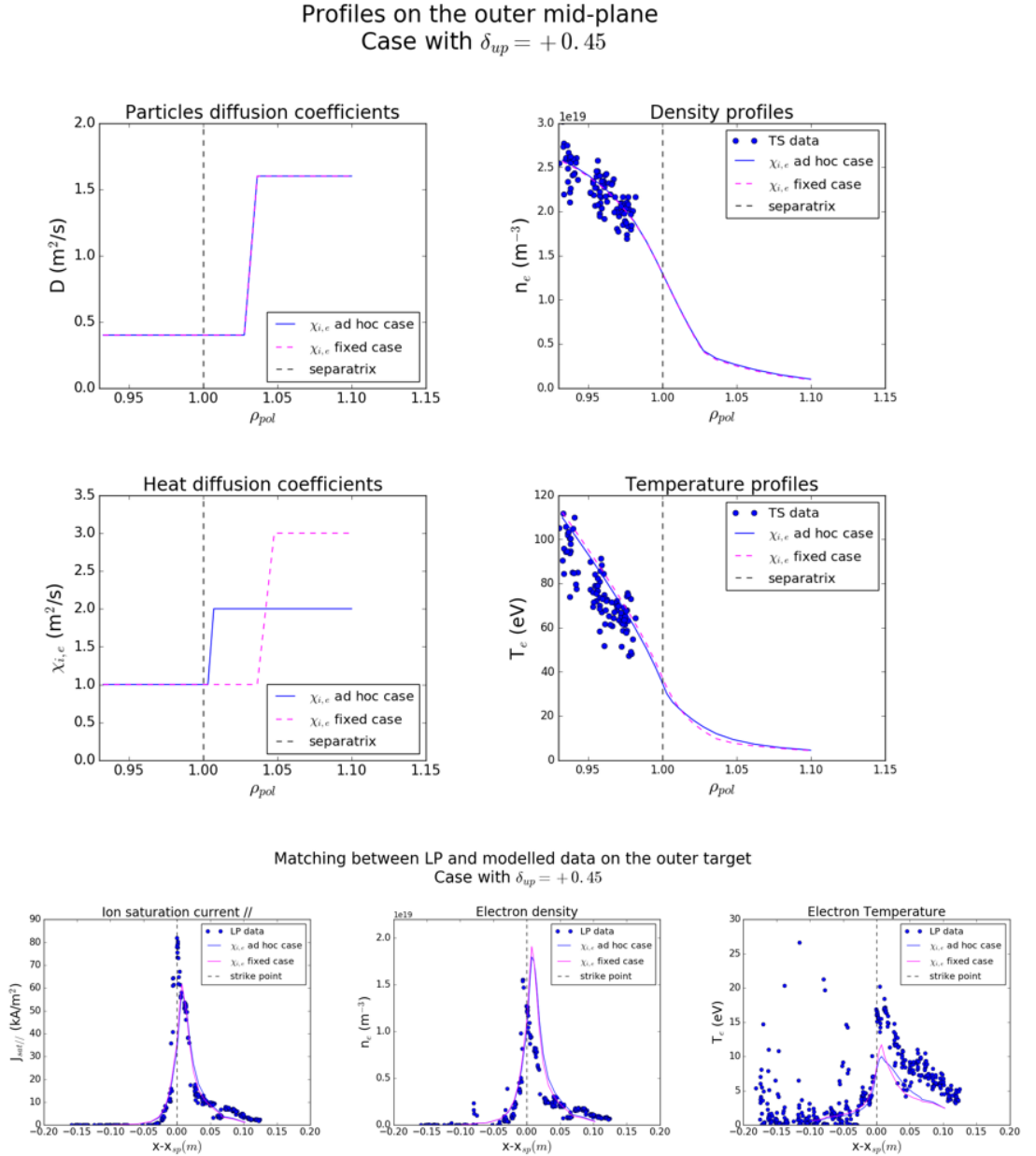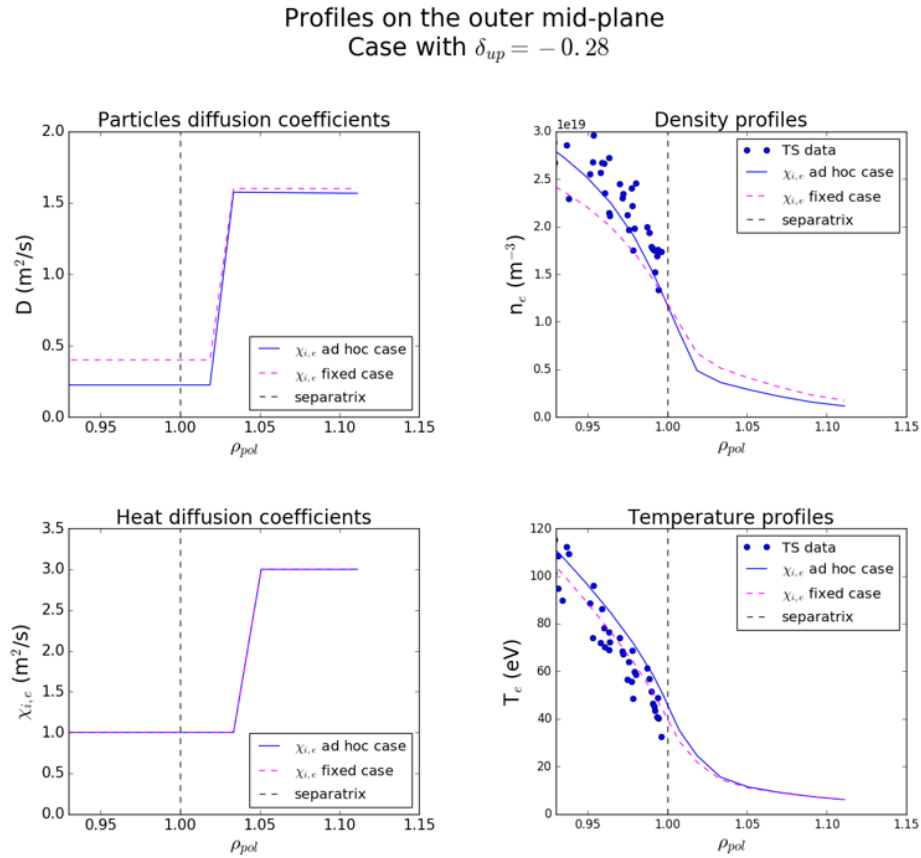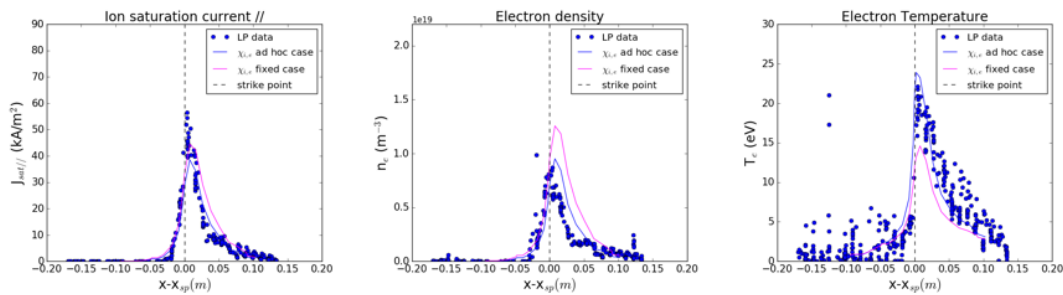
Figure 3.10: The same $\chi_{i,e}$ of pulse #52787, corresponding to the cyan profile in figure 3.9, is used to simulate pulse #52789 to investigate if triangularity affects the heat diffusion in the whole near-SOL and not only at the separatrix. On the top are shown outer mid-plane profiles, and on the bottom target profiles. Note that the match between data and simulated profiles is as good as before. [65]

Figure 3.11: The same D value of pulse #52789, corresponding to the blue profile in figure 3.9, is used to simulate pulse #52783 to investigate if triangularity affects particle diffusion. On the top are shown outer mid-plane profiles, and on the bottom target profiles. The density profile at the outer mid-plane is overestimated, and density and temperature at the outer target are overestimated and underestimated, respectively. Fixing D, the simulated profiles do not match experimental data as well as before. [65]
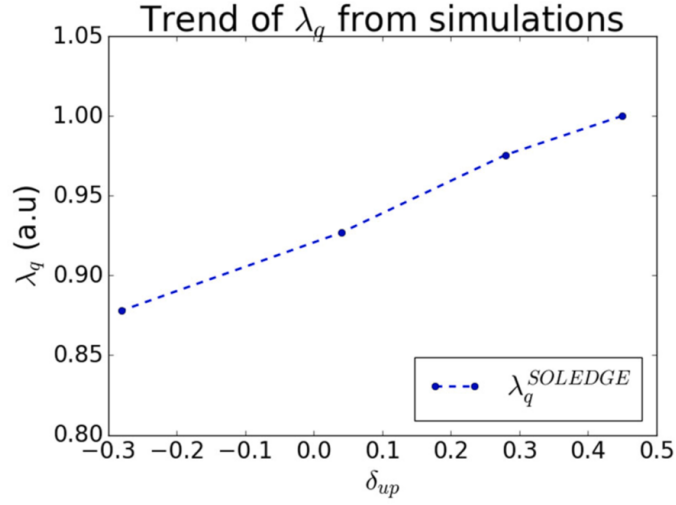
Figure 3.12: λ_q on the outer mid-plane obtained by modelling fitting the $nT^{3/2}$ profile. [65]

and heat diffusion and heat flux decay length behaviour. Modelling results explain the initial data analysis, showing that particle transport has a monotonic behaviour, decreasing towards NT, while the heat transport does not seem to depend on the triangularity. Moreover, the transport code highlights that λ_q on the outer mid-plane increases monotonically with δ_{up}, consistent with the IRT analysis [25]. What is found here is also consistent with results obtained independently and contemporary with GBS simulations [54].

Our analysis only allows precise information about transport coefficient values in the near-SOL due to the lack of experimental data in the far-SOL. Because of the importance of having information on this region, a necessary prerequisite to improve our studies will be to have more extensive diagnostic coverage in the experiments used for the analysis [38].

3.3 NT L-mode VS PT H-mode

This section is dedicated to comparing PT H-mode and NT L-mode plasma to compare relevant reactor conditions and understand if and how Negative Triangularity could provide improvements from the power exhaust point of view. In particular, the final aim of this study will be to use a modelling tool to predict the behaviour of NT plasmas for DTT. This device will also explore and test alternative materials and new divertor concepts [2]. Part of this work has been presented as a poster at the EPS conference in 2023 and at the annual meeting of the TSVV2-02 European work package.
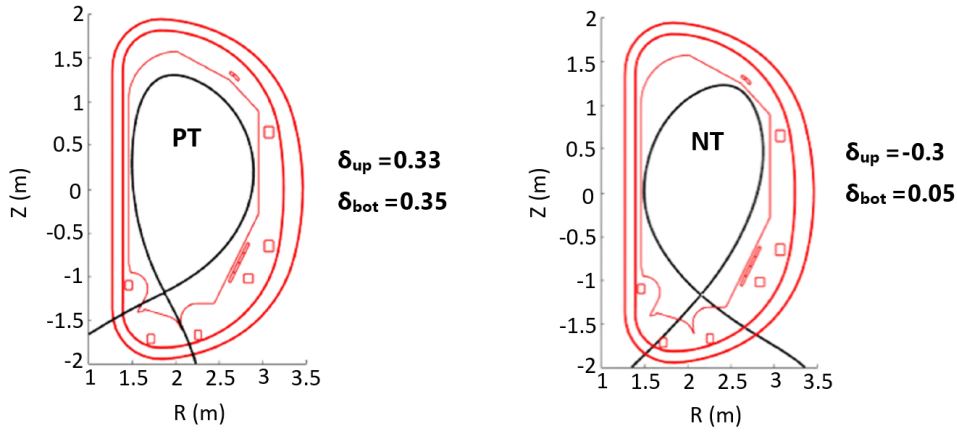
3.3.1 Experiment data set

Figure 3.13: Sketch of the DTT poloidal section with separatrix of SN PT (left) and SN NT scenario (right).

Our analysis is focused on couples of NT L-mode and PT H-mode pulses performed on TCV with the DTT-like shape. DTT single null positive triangularity scenario provides an upper and bottom triangularity of $\delta_{up} = 0.33$ and $\delta_{bottom} = 0.35$ respectively with $B_T = 6$ T and $I_p = 5.5$ MA. For the single null NT scenario, the values planned are $\delta_{up} = -0.3$ and $\delta_{bottom} = 0.05$ with $B_T = 6$ T and $I_p = 4$ MA. Figure 3.13 shows the different shapes in the poloidal section of the DTT device. Many TCV pulses have been performed[3] with different power supply, NBI, ECH or the two combined to try to reproduce as much as possible the two DTT scenarios. It is possible to extract the three couples shown in table 3.3 from

---

[3]2022 Experimental campaign WPTE/RT22-02.

experiments. All the shots have a magnetic field of $B_T = 1.4$ T and plasma current of about $I_p = -200$ kA. The upper and bottom triangularities are close to the DTT reference values except for the pulse number 73382, which comes from the previous experimental campaign dedicated to NT[4].

TCV pulses		I_{plasma} (kA)	δ_{top} / δ_{bottom} (LCFS)	NBI + ECH (kW)
#76701	PT H-mode	-200	+0.4 / +0.5	1300
#73382	NT	-240	-0.22 / -0.024	490
#76702	PT H-mode	-200	+0.4 / +0.5	1300
#76735	NT	-180	-0.3 / +0.08	500
#76702	PT H-mode	-200	+0.4 / +0.5	1300 + 900
#76735	NT	-180	-0.3 / +0.08	500 + 900

Table 3.3: Couples of PT H-mode and NT L-mode from the DTT-like experiments performed in TCV. Colours highlight the different couples.

3.3.2   Data analysis

During this experimental campaign, the Thomson scattering diagnostic has more extensive coverage than the previous study (section 3.2), covering until the bottom of the vessel. This extension makes it possible to investigate electron density and temperature in almost all the SOL. However, the geometry of the NT equilibrium does not allow the exploitation of all the advantages from the wide TS coverage because part of the area seen by the diagnostic is located in the private plasma region, which is not the object of this analysis. Despite this, useful information for NT near the separatrix can also be collected. Figure 3.14 shows the diagnostics positions used for the analysis: TS in green and Langmuir probes in black.
The analysis uses the pair of pulses highlighted in green in figure 3.3: PT H-mode #76702 and NT L-mode #76735. Figure 3.14 shows the equilibrium separatrix at the time of interest in the NBI-only heating phase. Currently, the additional power equals 1300 kW for PT and 490 kW for NT. Looking at the TS outer mid-plane profiles, shown in figure 3.15, the astounding and exciting thing is that NT L-mode recovers n_e and T_e of the PT H-mode in the core despite its L-mode condition and less than half input power.
Focusing on the edge and SOL region, NT shows a gradient around the separatrix,
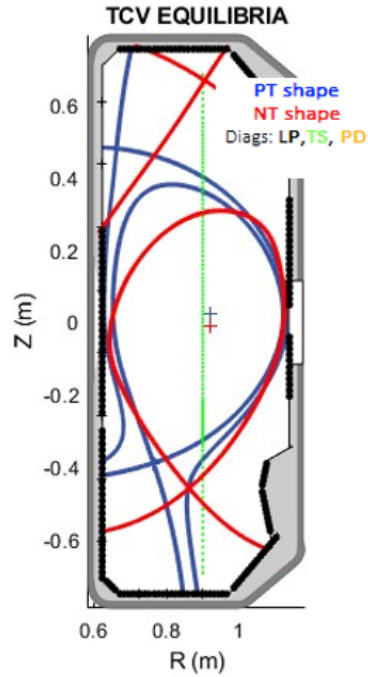
---

[4]2021 Experimental campaign WPTE/RT07.

Figure 3.14: Poloidal cross-section of magnetic equilibrium reconstruction for pulse numbers 76702 (PT, in blue) and 76735 (NT, in red). The figure shows the diagnostics locations used: Thomson scattering (TS) in green and Langmuir probes (LP) in black.
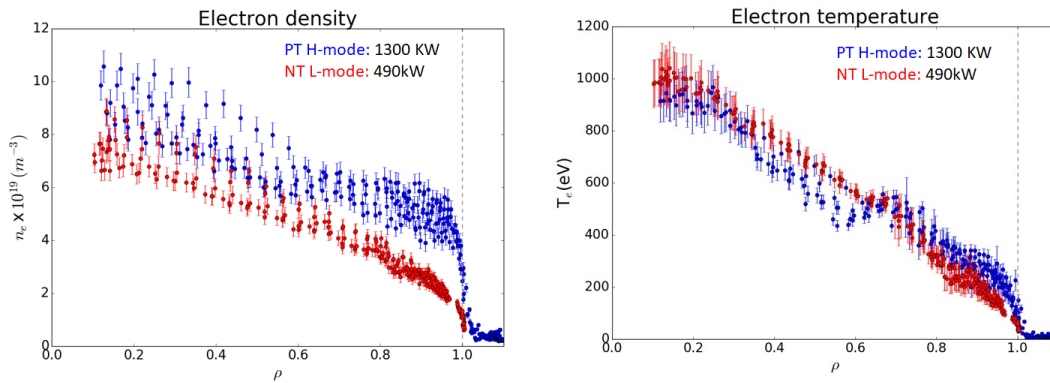

Figure 3.15: Electron density and temperature profiles on the outer mid-plane. TS data corresponding to a time interval of 100 ms. In blue is the PT H-mode, and in red is the NT L-mode case. The vertical dashed line indicates the separatrix position.

like a little edge barrier. Figure 3.16 compares n_e and T_e profiles of the green pulse couple during the NBI-only and NBI+ECH heating phase, while figure 3.17 shows the comparison between two other pulses, NT pulse #76742 and PT pulse
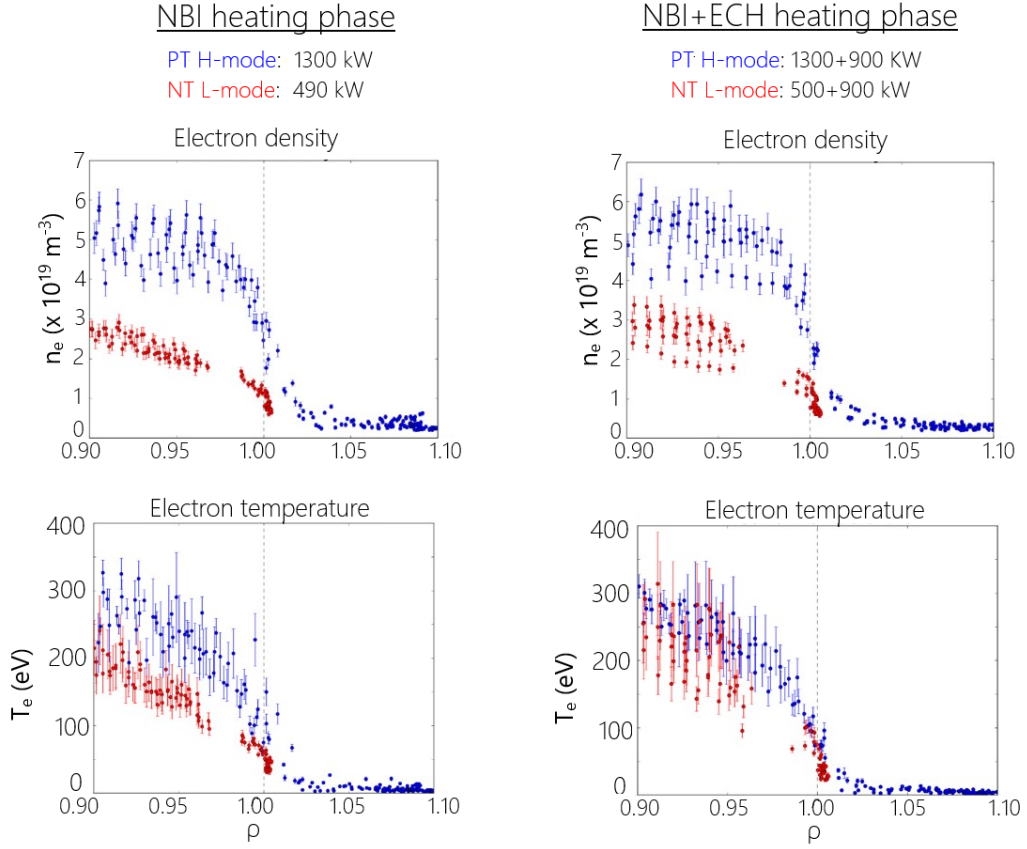
Figure 3.16: n_e and T_e profiles zoomed in edge-SOL region for the green pulse couple. In blue is the PT L-mode, and in red is the NT L-mode case. On the left is the comparison during the NBI-only heating phase, and on the right, is the NBI+ECH phase. The vertical dashed line indicates the separatrix position.

#76740, both in L-mode. These latter have the same ECH heating power of about 670 kW. All NT cases, independently from the additional heating used, have this little edge barrier. In particular, NT has a steeper gradient compared to the PT L-mode case (figure 3.17), which is consistent with the NT narrower λ_q found in the previous study (see section 3.2.3).

3.3.3   Modelling setup and results

Perpendicular transport of the green couple in table 3.3 is studied with the code SOLEDGE2D-EIRENE. Poloidal geometry, i.e. wall, pumps, divertor and gas valve positions, are equal to that of the experiment. Also, the D_2 puffing value corresponds to the real one. The pump does not have a significant role in TCV,
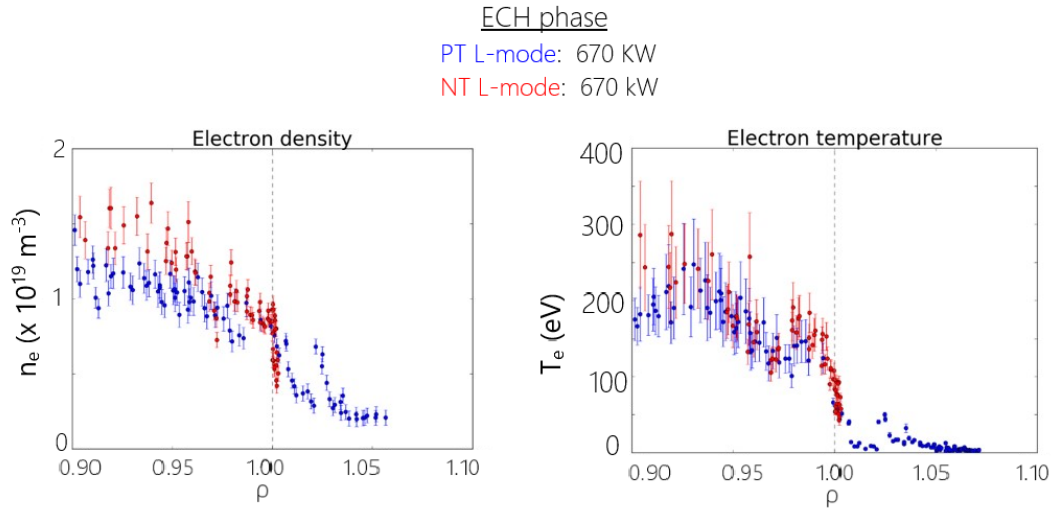
Figure 3.17: n_e and T_e profiles zoomed in edge-SOL region. Comparison between NT (red) and PT (blue), both in L-mode and with ECH-only heating. The vertical dashed line indicates the separatrix position.
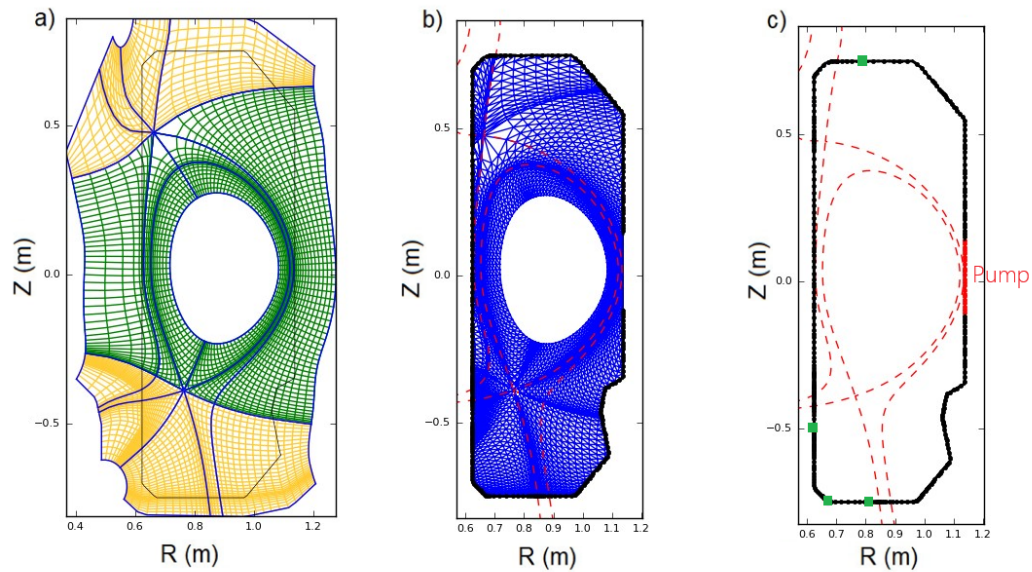

Figure 3.18: Pulse #76702: PT H-mode. Modelling meshes and wall: a) SOLEDGE2D quadrangles fluid mesh; b) EIRENE triangles mesh; c) gas-puffing (green squares) and pump locations (in red).

Figure 3.19: Pulse #76735: NT L-mode. Modelling meshes and wall: a) SOLEDGE2D quadrangles fluid mesh; b) EIRENE triangles mesh; c) gas-puffing (green squares) and pump locations (in red).
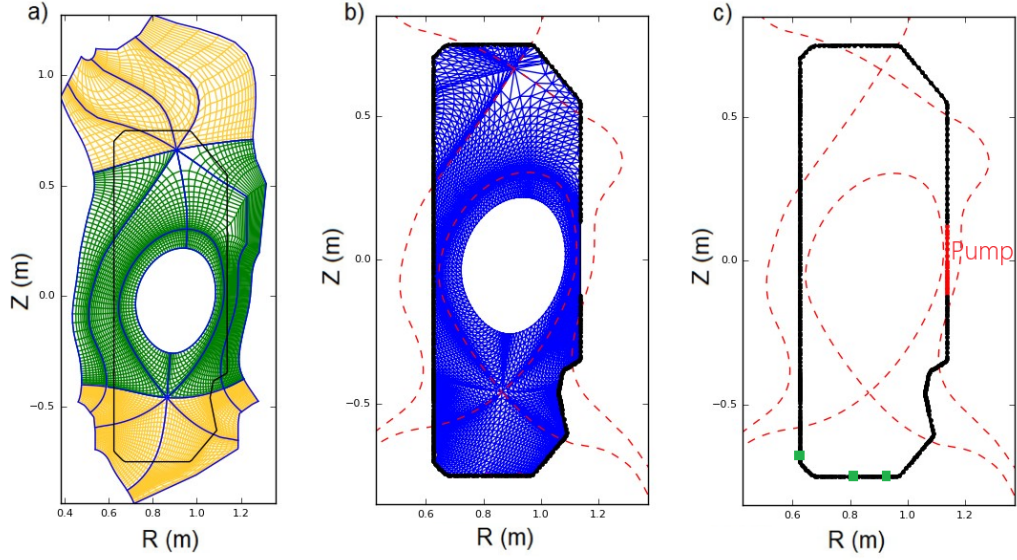
and the carbon wall plays a major role in the particle balance. The wall recycling coefficient, an input parameter of the code, is adjusted to achieve particle balance with the experimental puffing imposed. Figure 3.18 and 3.19 show the simulation domain for SOLEDGE (a) and EIRENE (b) with the relative grids used for the PT H-mode and NT L-mode, respectively. The SOLEDGE grid has a definition at the outer mid-plane between 0.5 mm (close to the separatrix) and 1.5 mm (in the near SOL) in the direction perpendicular to the magnetic field and at the target of about 0.5 mm in parallel direction w.r.t. $\vec{B}$. These high definitions prevent losing information about heat distribution. Figure 3.19c shows the position of puffing valves (green squares) and pump (red). Nor spatial magnetic field dependencies are included in transport values. P_{SOL} is computed by subtracting from the total heating, ohmic plus additional, the radiated power in the core and the radiation due to impurities since simulations are performed in pure Deuterium. The bolometry measurements are used to estimate all these radiations. In addition, averaged power loss due to ELMs, evaluated with the diamagnetic energy drops during the phenomena, is subtracted in the H-mode case. The resulting P_{SOL} is 628 kW for the PT and 277 kW for the NT case, and it is split equally between electrons and ions. The matching between experimental data and modelled profiles for PT and NT cases are shown in figure 3.20 and 3.21. Particle and energy diffusion, D and $\chi_{i,e}$, have been kept radially non-uniform specifically to reproduce electron density

and temperature on the outer mid-plane and the $J_{sat,i\parallel}$ profiles at the outer target. The resulting D and χ profiles confirm the presence of a small transport barrier at the separatrix in the NT configuration.
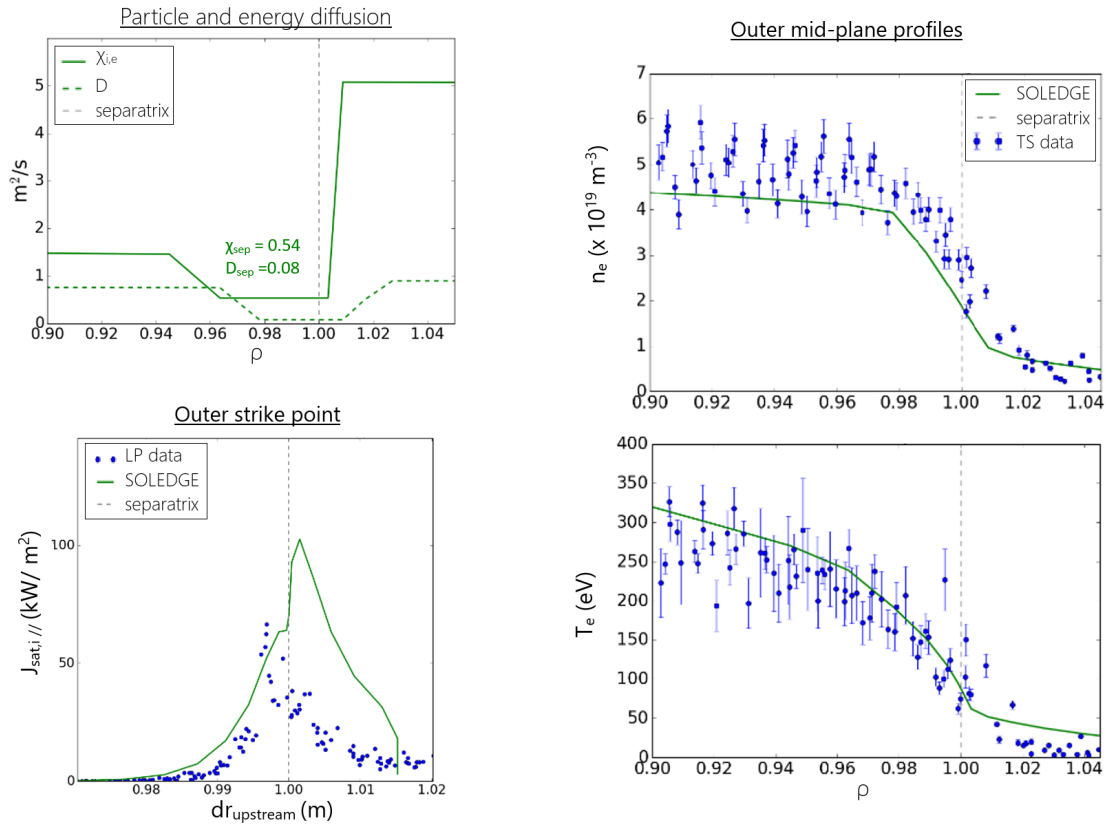

Figure 3.20: PT H-mode modelling. Upper left: Particles and heat transport profiles on the outer mid-plane to match experimental data. Bottom left: $J_{sat,i,\parallel}$ profile on the outer target[5]. The dashed line in grey indicates the strike point reference. On the right: n_e and T_e profiles in the edge-SOL region. The vertical dashed line denotes the separatrix. The solid green line corresponds to the simulated profiles, and blue dots with error bars correspond to the experimental data.

Comparing perpendicular transport profiles for the two cases, shown in figure 3.22 (PT H-mode in green, NT L-mode in magenta), NT perpendicular transport around the separatrix and in the near SOL results to be higher than in the PT H-mode. In fact, diffusion has the values of $D = 0.08$ m^2/s and $\chi_{i,e} = 0.54$ m^2/s for the PT and $D = 0.095$ m^2/s and $\chi_{i,e} = 1.01$ m^2/s for the NT case. Note that the NT diffusion found for this case agrees with the previous studies (see section
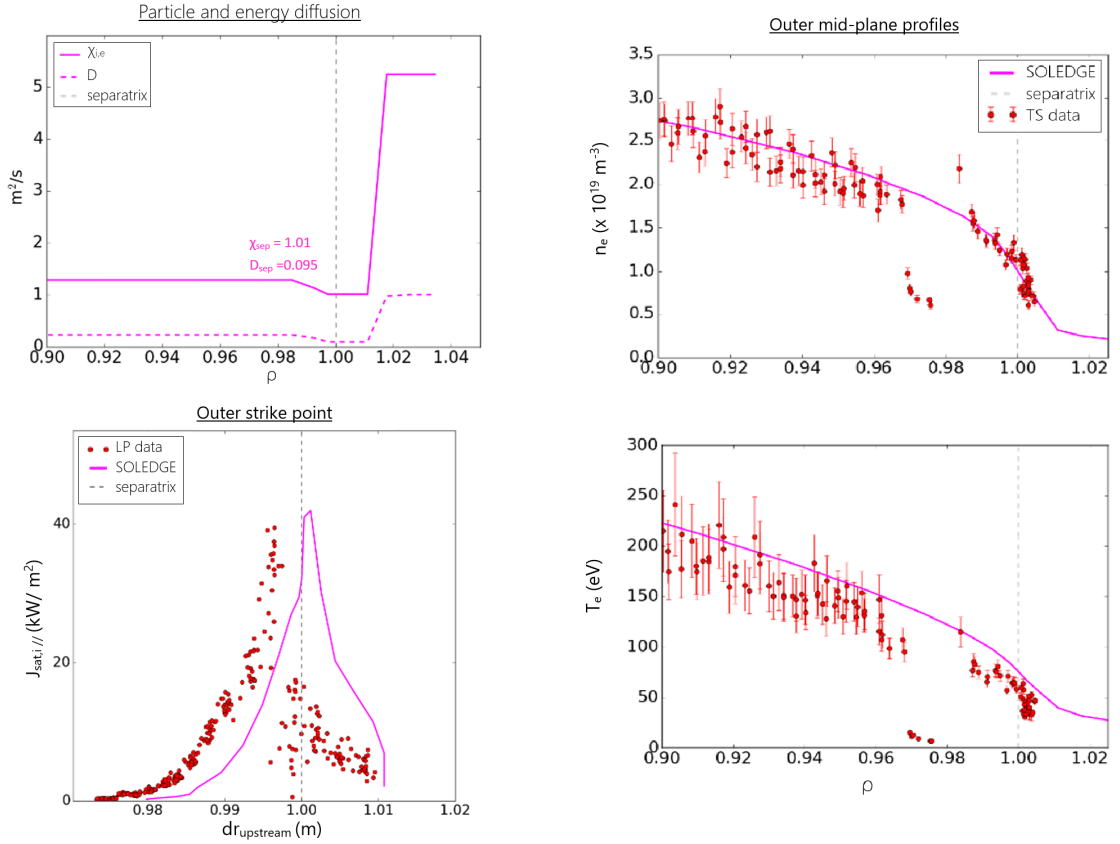
---

[5]Preliminary inter-ELMs data

Figure 3.21: NT L-mode modelling. Upper left: Particles and heat transport profiles on the OMP used to match real data. Bottom left: $J_{sat,i,\parallel}$ profile on the outer target. The dashed line in grey indicates the strike point reference. On the right: n_e and T_e profiles in the edge-SOL region. The vertical dashed line denotes the separatrix. The solid magenta line corresponds to the simulated profiles, red dots to the experimental data.

3.2.3). Nothing can be said about the far SOL because, as written before, no data are available for the NT configuration. The bigger perpendicular transport of NT, particularly for the heat part, is good news for the power exhaust dissipation because it allows the reduction of the power density convection to targets.

Figure 3.22 shows a comparison between three different situations: PT H-mode (green), NT L-mode (magenta) and PT L-mode (blue). Note that NT has a perpendicular transport between the two PT, both for particle and energy. Meanwhile, NT has the worst power exhaust performance compared to PT L-mode; it performs better than the reactor-relevant PT H-mode.
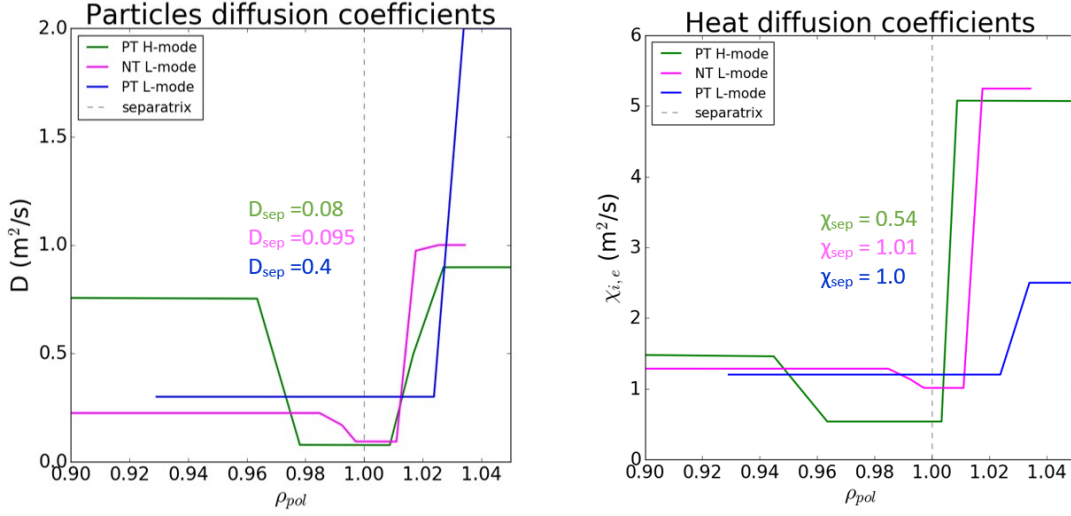
Figure 3.22: Comparison of particles (left) and heat (right) transport profiles on the outer mid-plane between the PT H-mode (green), NT L-mode (magenta) and PT L-mode (blue).

3.3.4 Section conclusions

The analysis compares PT H-mode and NT L-mode pulses with specific reference to DTT triangularity. Experimental data shows that the NT L-mode recovers the electron density and temperature of the PT H-mode in the core despite its L-mode condition and less input power. The SOLEDGE2D-EIRENE code is used to study the edge perpendicular transport. Here, particles and energy diffusion have been optimised to match experimental measurements, such as those given by Thomson scattering on the OMP and Langmuir probe in the divertor region. For the NT L-mode configuration, both experimental data and transport from modelling highlight the presence of a little barrier around the separatrix, also found in DIII-D experiments [67]. It can be speculated that this small barrier could have a role in the good confinement achievable with the negative D-shape. NT transport, which agrees with our previous studies, is found to be between PT L-mode and PT H-mode. NT has the worst power exhaust performance compared to PT L-mode but performs better than the reactor-relevant PT H-mode. The good power exhaust and core conditions are achievable with less power and without ELMs, making NT a really interesting configuration for a future reactor.

This work is still ongoing to extend the study by combining experiments from AUG, which work has already started, and DIII-D. The idea is to confirm what was found here and extrapolate NT L-mode transport for the DTT device. It will be beneficial, allowing us to foresee what kind of heat flux should be expected to

arrive at the targets of DTT in this alternative D-shape.

3.4 SOLEDGE3X application

Section 2.2 presents the code SOLEDGE3X, which can be used in 2D transport mode and in 3D first-principle turbulence mode. As written before, SOLEDGE3X is now under validation with experiments, but its first results are auspicious [36]. Moreover, the possibility of extending the domain up to the wall, peculiar to the two SOLEDGE codes, will allow us to have a complete overview of the physical phenomena present in the edge and SOL of the plasma. For these reasons, it has been decided to use this new code to investigate negative triangularity behaviours and understand why and how it differs from the PT.
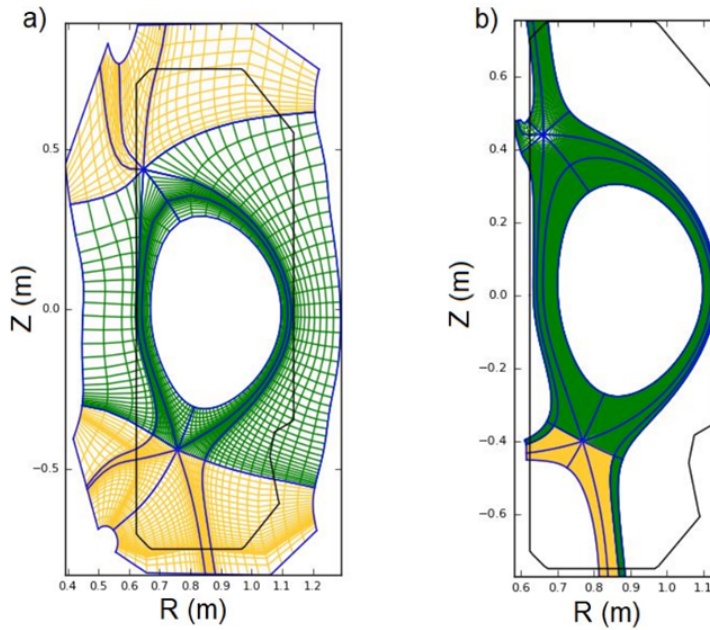

Figure 3.23: TCV pulse #73388: PT L-mode. a) fluid mesh with extended domain; b) turbulence mesh with reduced domain.

The study started analysing a PT-NT couple performed in TCV during the RT07 experimental campaign[6]. The two pulses, PT L-mode #73388 and NT L-mode #73382, have the same plasma current $I_p \approx -250$ kA and the same heating power from NBI ($P_{aux} \approx 490$ kW). While the positive pulse has δ_{up} =+0.39 and δ_{bottom} =+0.5, the NT case has δ_{up} =-0.22 and δ_{bottom} =-0.024.

To study turbulence, it is necessary to have a mesh with a spatial resolution of about the scale of the ion Larmor radius. Due to the long computational time needed to reach the steady state (estimated to be approximately 3.2×10^5 hours),

---

[6]RT07: Negative Triangularity scenarios as an alternative for DEMO.

it is decided to start with a reduced domain and less resolution: the high resolution of about 1 mm only is applied on the outer mid-plane because we are working in pure deuterium. Figure 3.23 shows the mesh for the PT case with, on the left, the resolution needed to make transport studies and on the right that to make turbulence analysis. First, the simulation was performed in 2D transport mode, which was easy and fast to run, until particle and energy balance was reached. After that, the case was extended on 1/4 of the torus and turbulence mode was activated. So, drifts and current balance are considered by the code. For neutrals, the fluid model was used. Until now, $2.4\mu s$ of the plasma was simulated; simulation is far away from the steady state, and no turbulence is visible. This work will continue in parallel with NT-PT fluid simulations in the following months.

Chapter 4

Super-X divertor PEX study

The detachment (section 1.3.1.2) is one of the desirable regimes for future fusion reactors thanks to particle and heat flux reduction that it allows to have on divertor plates. Advanced divertor magnetic configurations are potentially promising to reduce the plasma and impurity density thresholds for detachment. One of these configurations is the Super-X Divertor (SXD), which shows the theoretical onset of the detachment at lower $\langle n_e \rangle$. In this chapter, the advantages of SXD are described in the section 4.1 and the numerical study done on TCV discharges about the Super-X configuration is shown in section 4.2.

4.1   The Super-X divertor

In the SXD, the outer strike point radius, R_t, is maximised with many positive consequences. In particular, the magnetic connection length $L_\parallel$ and the plasma-wetted area A_w on the divertor plate are increased, and the magnetic flux tubes broaden. In such a way, the parallel heat flux, $q_\parallel$, decreases along the flux tube towards the target, followed by a lower plasma temperature at the divertor plate. Consequently, the radiation in the divertor increases with fewer impurities bleeding back into the main plasma. Together, all these improvements can increase the total power that may flow into SOL by a factor of about 5 compared to the standard divertor (SD) while keeping the heat flux on the divertor plate below the actual material limit of 10 MW/m² [97, 50].

The potential benefits of larger R_t geometries in terms of detachment behaviour and heat exhaust come directly from the SOL physics and can be expressed simply by using a modified TPM [72, 49], which allows the implementation of the dependence from R_t. The difference between the modified model and the one shown in section 1.3.1.1 is that it lets variate R along the length of SOL flux tubes, allowing

the change of the cross-sectional area of the SOL perpendicular to $\vec{B}$ due to magnetic flux expansion: $A_{SOL\parallel} \propto 1/B$. When R and $A_{SOL\parallel}$ vary along the flux tube, $q_\parallel$ is no longer constant along the flux tube too ($q_\parallel \propto 1/A_{SOL\parallel} \propto B$) and equation 1.11 for the parallel electron heat conduction needs to be modified. Considering the simple TPM assumption of no volumetric power loss/gain along the flux tube

$$\frac{q_\parallel(\theta)}{q_\parallel(0)} = \frac{B(\theta)}{B(0)} \approx \frac{B_\phi(\theta)}{B_\phi(0)} = \frac{R(0)}{R(\theta)}$$

where θ is the poloidal location along the flux tube and 0 the OMP. So

$$q_\parallel = q_{\parallel,OMP}\frac{R_{OMP}}{R}$$

which is general for any location along the flux tube. Making some assumptions (for details, see reference [73]) and focusing put of simplicity on the outer divertor and strike point (OSP), the following relations can be defined. Figure 4.1 shows some useful quantities: the heat flux towards the target $q_\parallel$, the infinitesimal volume between two closely flux surfaces upstream and at the target, Δr^u and Δr^t, the target tilt w.r.t. the magnetic field, β, and the outer strike point radius, R_t. The heat flux that arrives perpendicular to the divertor plate, $q_\perp^t$, assuming toroidal symmetry, can be written as

$$q_\perp^t = \frac{R_u}{R_t}\sin\beta\, q_\parallel^t \tag{4.1}$$

where R_u is the major radius upstream and $q_\parallel^t = q_\parallel^u/f_x$ in which f_x is the *flux expansion*. This latter is the ratio of the perpendicular flux surface at the target and upstream

$$f_x = \frac{\Delta r^t}{\Delta r^u} = \frac{B_\theta^u R_u}{B_\theta^t R_t} = \frac{B_\theta^u B_\phi^t}{B_\theta^t B_\phi^u}$$

where θ and ϕ denote poloidal and toroidal components. From the definition of $q_\perp^t$ itself, it is clear that one way to reduce it is to move the outer strike point (OSP) to a larger major radius. Other possibilities are increasing the flux expansion or/and tilt the target. As said before, increasing R_t allows an increase in the plate's wetted area

$$A_w = A_{SOL\parallel}^t = \frac{2\pi R_t}{\sin\alpha}\lambda_q f_x$$

and to decrease the electron temperature at the target

$$T_e^t \propto \frac{1}{f_x^2}\left(\frac{R_u}{R_t}\right)^2\frac{(q_\parallel^u)^{10/7}}{L_\parallel^{4/7}}\ . \tag{4.2}$$
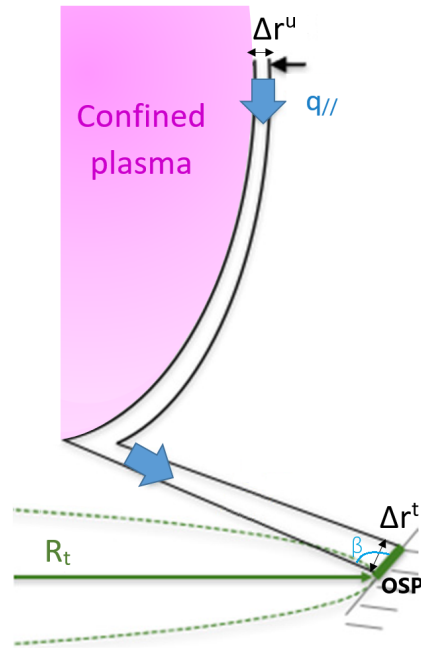
Figure 4.1: Sketches of heat transport between two closely spaced flux surfaces in the SOL from upstream to the outer target.

The modified TPM also provides an equation for the electron density at the target

$$n_e^t \propto f_x^2 \left(\frac{R_u}{R_t}\right)^{-2} \frac{L_\parallel^{6/7}}{(q_\parallel^u)^{8/7}} \tag{4.3}$$

Only the significant dependencies that differentiate the simple and the modified model are shown in these last two equations. The dependencies from R_t of the ion saturation current collected by Langmuir probes at the target would also be useful for the study. Considering that $J_{i,sat} = e\,n_e M c_s$, where M is the Mach number and $c_s \sim \sqrt{T_e}$ is the sound speed in the fluid, it follows that

$$J_{i,sat} \propto R_t \ \ .$$

From the theoretical equation 4.2, it is evident that SXD configuration, with the increase of both R_t and $L_\parallel$, could be an excellent candidate to have easier detachment compared to SD.

4.2   Numerical study of Super-X L-mode on TCV

As mentioned in section 4.1, the Super-X divertor configuration theoretically allows for a lower-density detachment onset. However, experiments on DIII-D [72] and on TCV without baffles [93] did not agree with the expected trend. One plausible reason is the difference in geometric design and the strike-point angle of the cases analysed, which results in varying neutral particle confinement. As SOLPS-ITER modelling has demonstrated [28], in order to have more similar divertor neutral confinement, it is necessary to force a constant poloidal incidence angle between the divertor leg and wall and have a solid divertor closure by using baffles. Based on these predictions, more optimised experiments have been performed [92], but they still showed considerable deviations from the Two-point model.

It is presented here the work done using the code SOLEDGE2D-EIRENE on three fully baffled Super-X L-mode discharges performed on TCV with three different outer strike-point radii. The goal is to understand why experiments deviate from the model predictions. This study has been published in the journal *Nuclear Materials and Energy* in 2023 [61].

4.2.1   Experiment and modelling set-up

The three experimental cases compared are all L-mode ohmic discharges with $P_{ohm} \approx 280$ kW and plasma current of $I_p = 250$ kA, see figure 4.2. The three pulses are characterised by a density ramp, which is useful to evaluate the detachment onset as a function of the outer strike point position. Figure 4.3(A) shows equilibria of the pulses in analysis. Discharge number 70202, in blue, is the "small" case with the outer strike point at $R_t = 0.62$ m, pulse #70201, in magenta, is the "large" scenario with $R_t = 1.01$ m, and shot #70207, in red, is the "extreme" case with $R_t = 1.08$ m. The small and the large cases have similar poloidal flux expansion and poloidal incidence angle, $f_x = 2.5 - 2.9$ and $\beta = 114° - 111°$ respectively. At the same time, the extreme scenario could not achieve for technical reasons such properties, so it has $f_x = 1.4$ and $\beta = 80°$.

The radial values of the perpendicular transport used in SOLEDGE2D-EIRENE are shown in figure 4.4. Diffusion has been chosen to have a reasonable agreement between simulation results and experimental data from Thomson Scattering (TS), Langmuir Probes (LP) and Bolometry (see figure 4.3(B) for diagnostic positions). The same input parameters and transport conditions are applied to all three cases to eliminate potential differences arising from cross-field transport. Carbon impurities originating from the wall are introduced through physical and chemical sputtering processes on all plasma-facing components, employing the same transport mechanism used for deuterium. The chemical sputtering, which is typically bigger than the physical sputtering (see the Roth-Bohdanky formula [7]), is assumed to
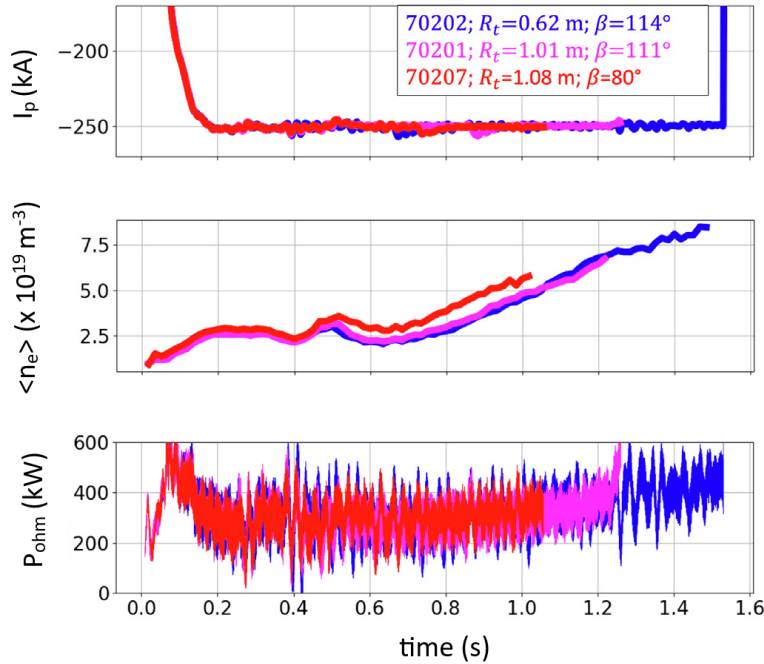
Figure 4.2: From the top: plasma current, average electron density and ohmic heating in time for the three cases analysed. [61]

yield 3.5%. The carbon recycling coefficient, difficult to determine in experiments, is imposed on carbon tiles to be $R_c = 0.73$ to obtain a total radiated power in the SOL in agreement with the bolometry experimental data. The Deuterium recycling coefficient has been assumed to be $R_D = 0.99$ [30]. The heating power crossing the radially inner core boundary is distributed equally between electrons and ions and chosen to match the power crossing the separatrix for all three cases. The D_2 injection, which takes place in the Private Flux Region (see figure 4.3), has been adjusted in each geometry to have the same electron density at the separatrix, $n_{e,sep}$. The resulting puffing rates for the small, large and extreme cases are respectively 4.5×10^{20} particles/s, 3.01×10^{20} particles/s and 4.0×10^{20} particles/s.

4.2.2 Upstream plasma parameters and profiles

Figure 4.5 shows electron density, n_e, and temperature, T_e, along the SOL. Here, the solid lines represent the modelling results, the dots are the experimental data with error bars, and the dashed lines are the average over 100 ms. The time
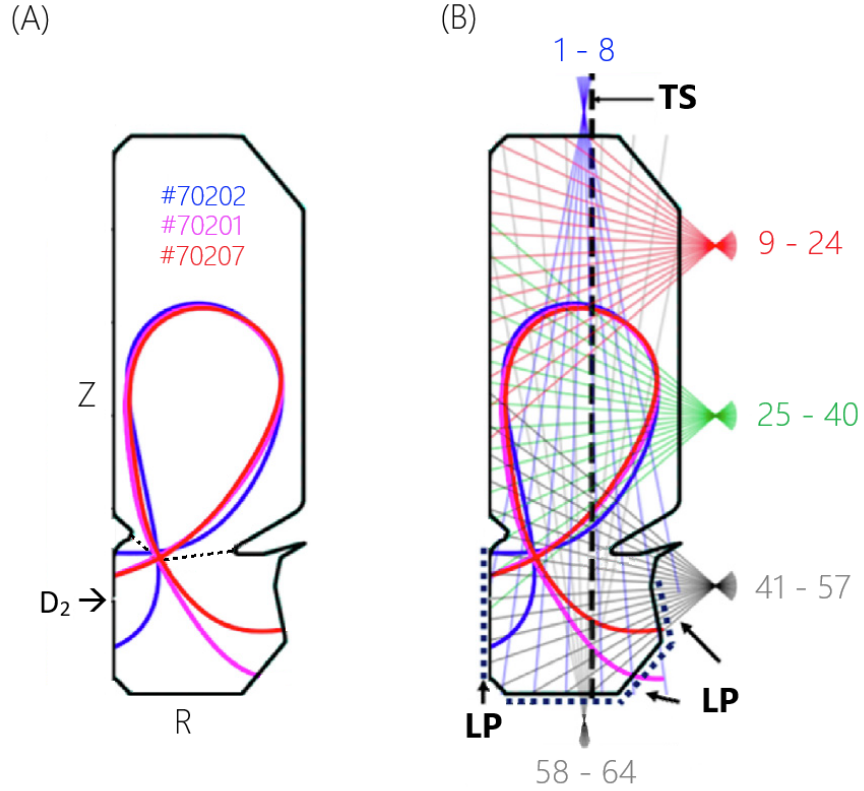
Figure 4.3: (A) TCV poloidal cross-section with the separatrix of the three cases, small in blue, large in magenta and extreme in red, and the D_2 injector position. The dashed black line separates the divertor region from the main chamber region. (B) Thomson scattering (TS) in dashed vertical black line, Langmuir probes positions (LP) in black squares, and line of sight of the bolometry clockwise: LOS in blue, red, green and grey. [61]

chosen correspond to that when the average density value[1] at the separatrix is $\langle n_{e,\text{sep}} \rangle = 1.3 \times 10^{19} \, \text{m}^{-3}$. The experimental and simulated electron density profiles, as shown at the top of Figure 4.5, agree within the error bars for the large and extreme cases. However, there is less agreement for the small scenario, where the modelling shows approximately 20% lower values in the core and approximately 30% higher values in the SOL. This discrepancy can be attributed to the improved neutral confinement in the divertor region, which is more pronounced at small R_t (in line with findings in reference [30]). Defining the divertor closure as the ratio between the average total neutral density in the divertor region (see fig. 4.3) and

---

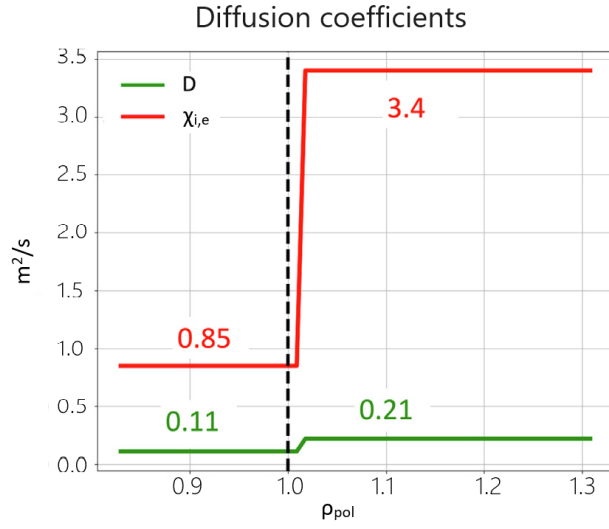[1]The average is calculated using TS data.

Figure 4.4: Diffusion coefficients for particle, D, and energy, $\chi_{i,e}$. [61]
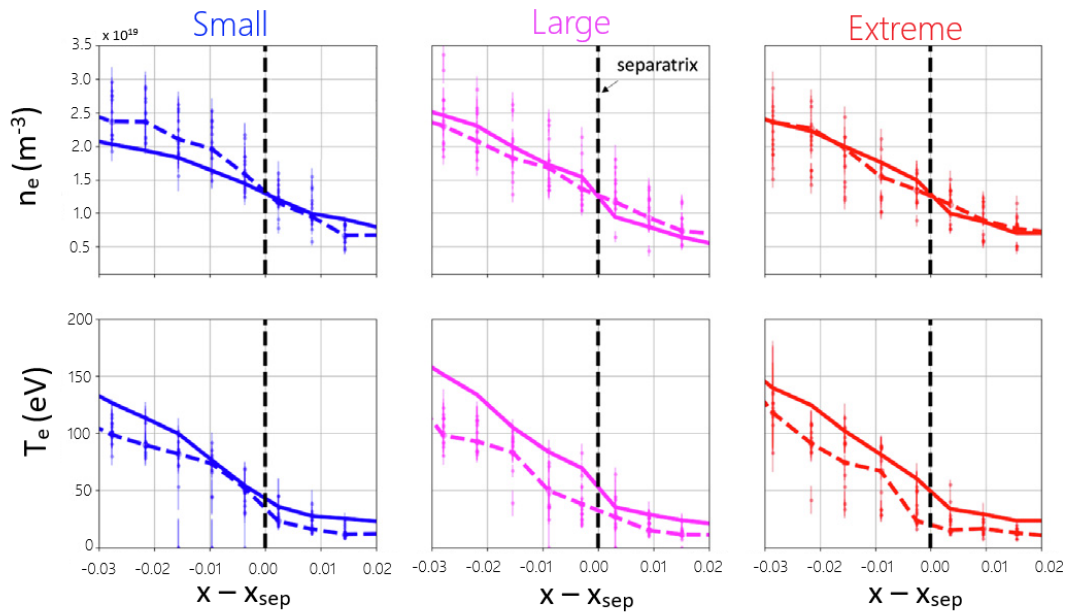

Figure 4.5: Electron density and temperature from TS data, dots with error bar and averaged data in dashed lines, and from SOLEDGE2D-EIRENE simulations, solid line. From left to right: the small, the large and the extreme case. [61]

the main chamber over the volume

$$c_{div} = \langle n_n \rangle_{div} / \langle n_n \rangle_{\mathrm{main}}$$

it is found that $c_{div} \approx 65$ in the small case, about 30 in the large, and 55 in the extreme R_t case. The electron temperature (bottom of fig. 4.5) is higher than the experimental value but still within the error bars in all cases. This overestimation is intentional because it is necessary to better agree with experimental data on the outer target. This approach is common for 2D transport codes such as SOLEDGE2D and SOLPS-ITER [100].
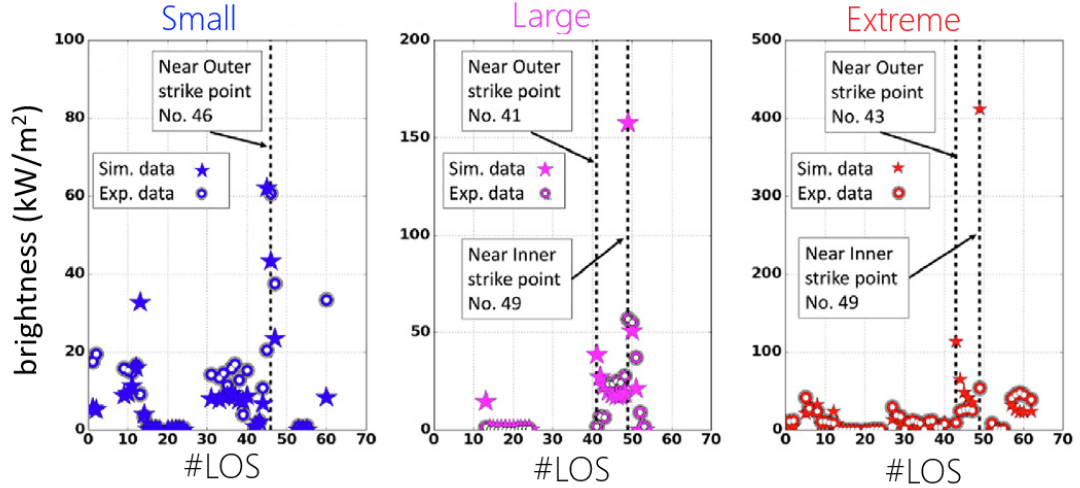
4.2.3 SOL radiation

Figure 4.6: Comparison between experimental and synthetic data: brightness for each line of sight (LOS) of the bolometer for the small (blue), large (magenta) and extreme (red) cases. The stars represent SOLEDGE results, and the dots represent the experimental data. [61]

The power entering the SOL results in about 280 kW. It is calculated as $P_{\mathrm{input}} = P_{\mathrm{ohm}} - P_{\mathrm{rad,core}}$, where $P_{\mathrm{rad,core}}$ is the total radiation from the region of the core not included in the SOLEDGE2D mesh (≈ 15 kW). In order to have the measured radiation of about 100 kW, the carbon recycling coefficient is set to $R_C = 0.73$. The radiation distribution in the SOL can be explored using SOLEDGE synthetic bolometer developed for TCV modelling. Figure 4.6 compares each bolometric chord's experimental and simulated brightness. Reasonable agreement is achieved all around the domain for all the cases. The dashed black vertical line indicates the position of the inner and outer targets. In the small case (blue), the agreement

of the data is very good, particularly near the outer target. Data are not available for the inner target, as shown better in figure 4.7. Figure 4.7 is the zoom of the previous one and allow us to have a deeper look around the inner and outer strike point. In large and extreme cases, there is good agreement around the outer leg, represented by the grey-shaded area. Less agreement is around the inner leg, the light blue shaded area, where the simulated chord brightness exceeds measured values. This discrepancy could be due to an overestimation of the carbon content in the divertor or to a favourable plasma condition for local carbon radiation in the simulations.
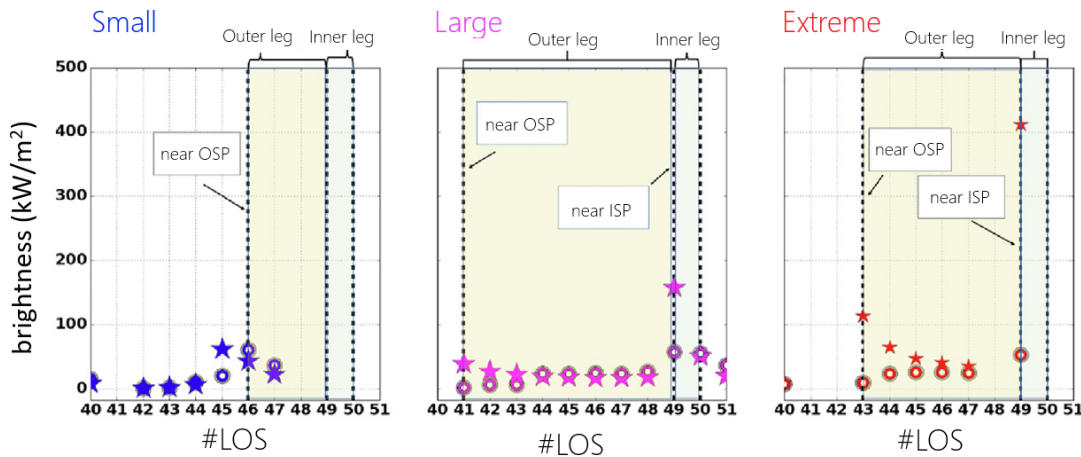

Figure 4.7: Zoom of figure 4.6. OSP and ISP stay for the outer and inner strike points, respectively. Stars represent SOLEDGE results and dots the experimental data. [61]

4.2.4 Target plasma parameters and profiles

For all three cases, as Figure 4.8 indicates, SOLEDGE overestimates the density peak ($n_{e,\text{peak}}$) compared to experimental Langmuir probe measurements, particularly by a factor of 3 for the small case and by a factor of 2 for the large and extreme cases. The electron temperature peak ($T_{e,\text{peak}}$) is well reproduced by simulations for the small and extreme cases but is underestimated for the large case. Unfortunately, the uncertainties about the carbon wall emission and the associated radiation make it complicated to provide a proper interpretation of the observed discrepancy. In the large case, the $T_{e,\text{peak}}$ is lower than that of the extreme case, contrary to experimental data. This difference might be related to the different poloidal angle β incident to the wall, which could also impact carbon sputtering emission. Finally, the ion saturation current, J_{sat}, agrees with the experiment, overestimating the peak only by a factor of about 1.2. Figure 4.8 also shows that
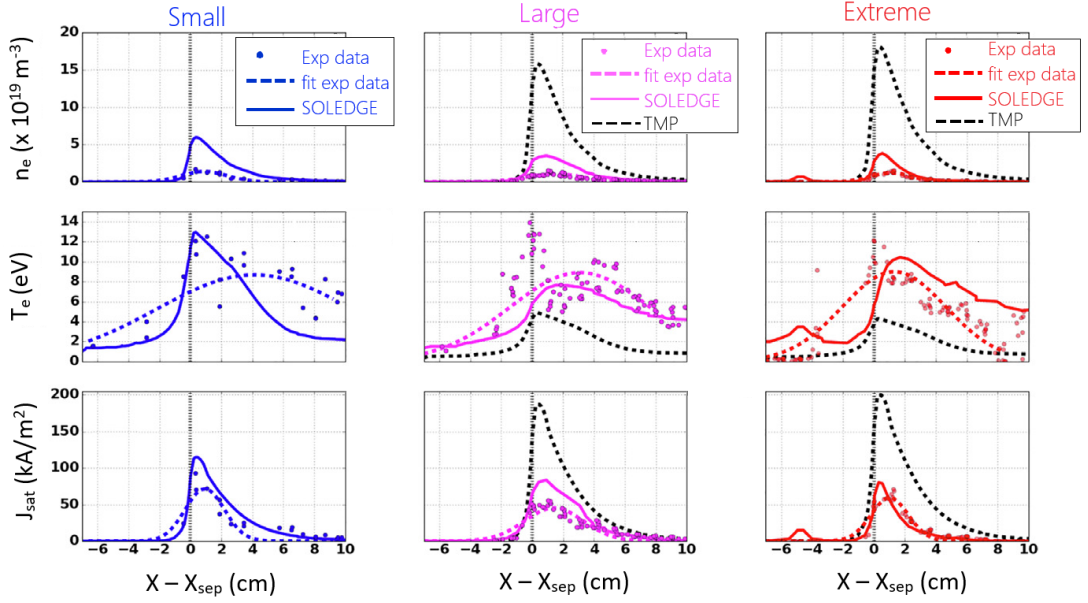
Figure 4.8: Form the top: outer target profiles of electron density, n_e, temperature, T_e, and ion saturation current, J_{sat}. From left to right: the small (blue), large (magenta) and extreme (red) R_t case. The abscissa represents the distance from the strike point along the wall, and the dashed black vertical line indicates the strike-point location. Dots represent experimental data from Langmuir probes, and the dashed curve is the fit of the data. In large and extreme cases, the modified TPM prediction is represented by the dashed black curve. [61]

for the large and extreme cases, both experimental and simulated data deviate from the modified TPM predictions (see section 4.1)

$$T_{e,target} \propto \frac{1}{R_t^2} \qquad n_{e,target} \propto R_t^2 \qquad J_{i,sat} \propto R_t$$

showing lower density and saturation current but higher temperature. Part of the divergence between real and simulated data could be attributed to neutral confinement, as explained in the following section 4.2.5.

4.2.5   Increasing the divertor closure

The studies presented so far have been conducted using the current geometry of the TCV outer baffle, and they indicate that the small R_t case exhibits better neutral confinement in the divertor than the other two cases. The same three pulses were modelled with the addition of an extended outer to determine whether improved divertor closure can help achieve the expected results according to the
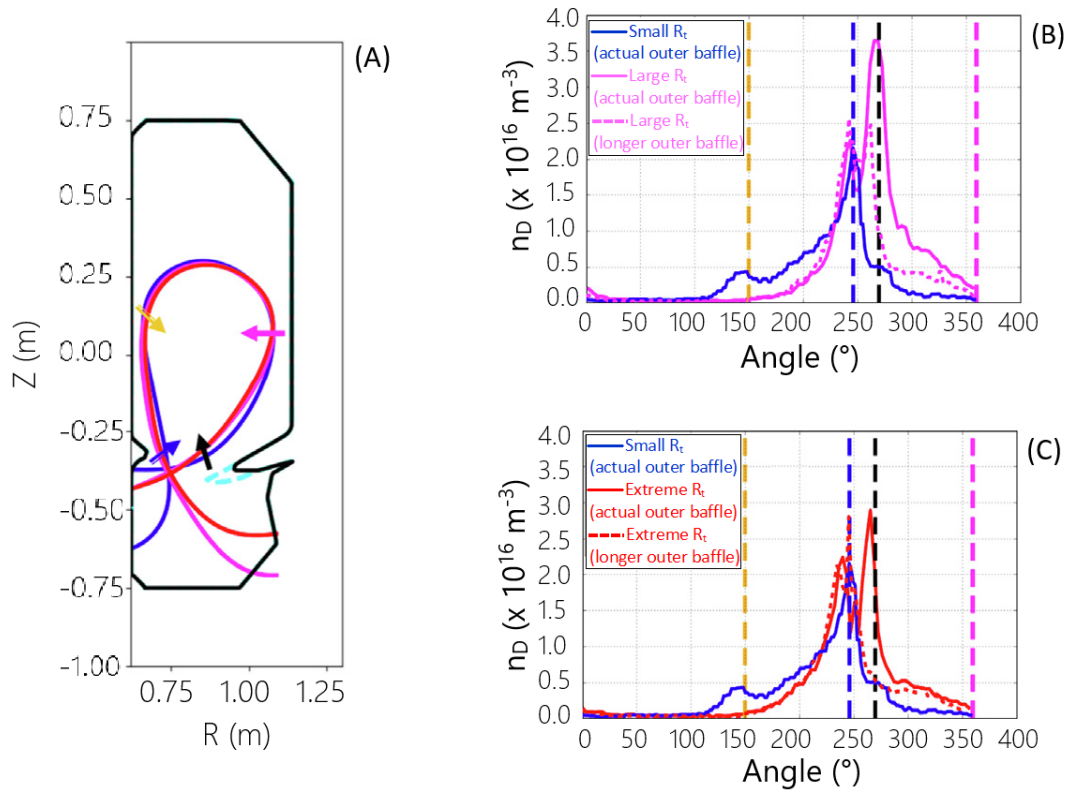
TPM

Figure 4.9: (A): poloidal cross-section with equilibria and longer baffle in cyan. (B-C): neutral deuterium density, named as n_D, along the LCFS as a function of the poloidal angle. The outer mid-plane is at $360°$ and $0°$. The peak at $150°$ (orange vertical dashed line and orange arrow in (A)) is near the inner mid-plane, the peak at $250°$ (blue vertical dashed line and blue arrow) is close to the inner baffle, and the peak at $270°$ (dashed vertical black line and black arrow) corresponds to the outer baffle. In (B), the small case with the actual baffle (blue solid line) is compared with the large case using the actual (magenta solid line) and the longer baffle (magenta dashed line). In (C), the small is compared with the extreme case, with the actual baffle (continuous red line) and the longer one (red dashed line). [61]

baffle. The new geometry, featuring a synthetic baffle approximately 9 cm longer, is depicted in Figure 4.9(A), while (B-C) display the neutral atom density along the LCFS, denoted as n_D, for the various cases. The goal is to achieve a neutral pressure as close as possible to that of the small case with the actual baffle, thus eliminating the variability associated with n_D. Figure 4.9(B-C) shows that the longer baffle reduces n_D along LCFS by about 30% in the large case and 10%

in the extreme R_t case. In particular, there is a significant reduction of neutral particles coming from the outer leg and entering the core with the vanishing of the peak at 270° (black line in fig. 4.9(B-C) and black arrow in (A)). Moreover, the flux of neutral particles from the inner leg at 250° (blue line in fig. 4.9(B-C) and blue arrow in (A)) remains relatively consistent across the three cases leading to the compression factor $c_{div} \approx 75$ for the small case, $c_D \approx 162$ for the large and $c_D \approx 200$ for the extreme R_t case. While the effect is negligible for the small case, the other two cases exhibit a significant increase in their compression factor when they have a neutral density on the LCFS, similar to that of the small case with the actual baffle. Figure 4.10 shows the profile on the outer target of electron
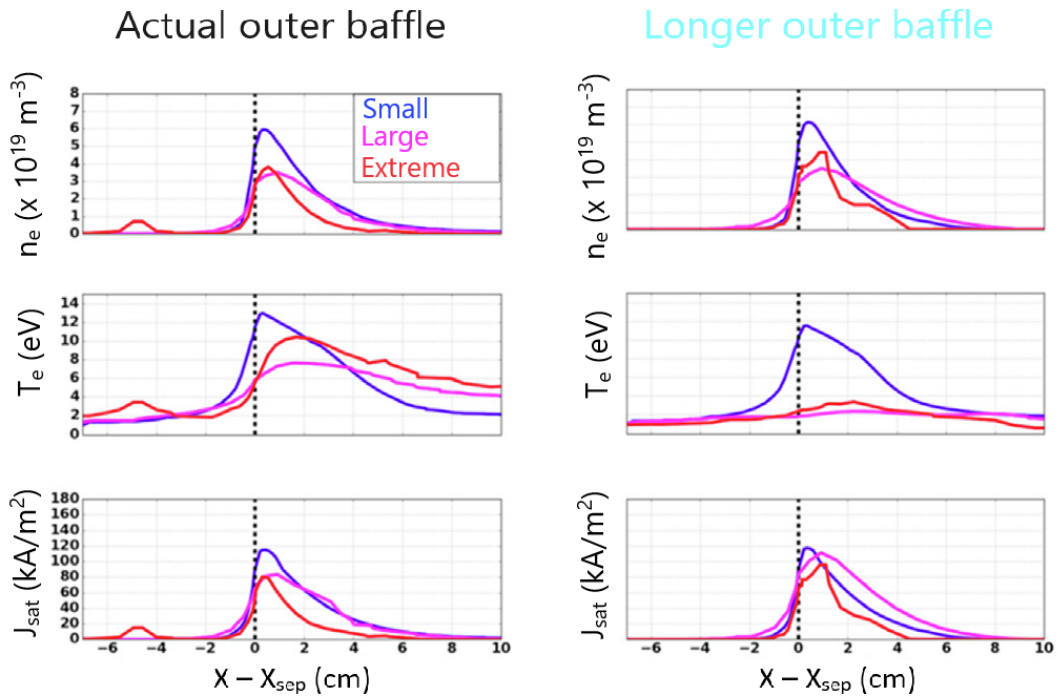

Figure 4.10: Comparison of outer-target electron density, n_e, temperature T_e, and ion saturation current J_{sat} between the actual outer baffle (left) and the longer outer baffle (right) for all the three cases: small in blue, large in magenta and extreme in red. The abscissa is the distance from the outer strike point (dashed black line) along the wall. [61]

density, n_e, temperature, T_e, and the ion saturation current, J_{sat}, obtained using the real (left) and the longer (right) outer baffle. Note that the integral value of J_{sat} stays stable for the small and extreme case, while in the large R_t case, the longer baffle increases it by about 36%, remaining far away by what is predicted by the modified TPM (figure 4.8). Focusing on the electron temperature, in the large
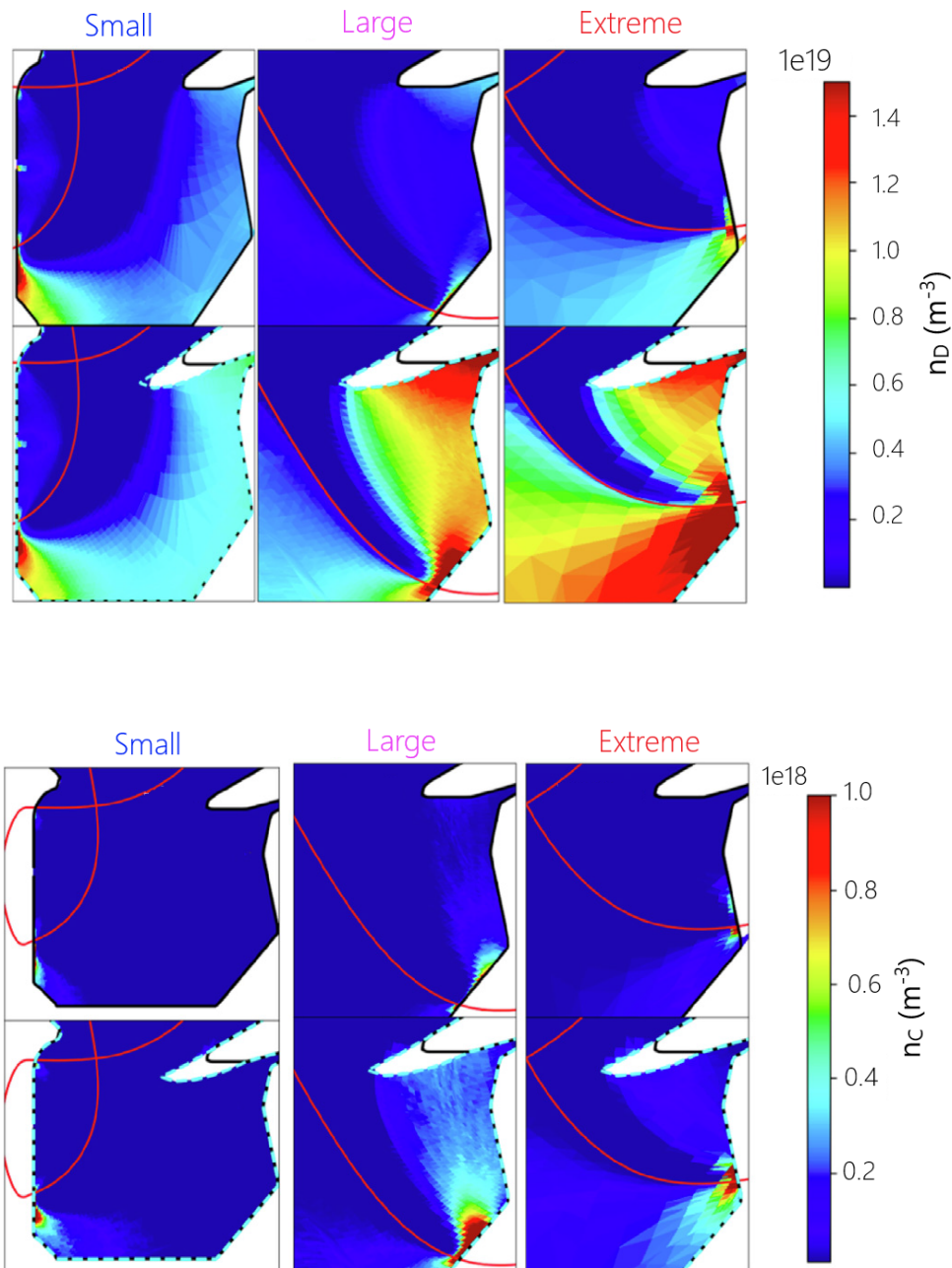
Figure 4.11: 2D divertor plots of the total neutral density, n_D, and total carbon density, n_C, with the actual outer baffle (top) and the longer one (bottom). For the large and extreme R_t cases, only the outer leg and strike point, where most of the changes appear, are shown. [61]

and extreme case, it drastically drops around 3 eV, similar to what is expected from modified TPM prediction (figure 4.8). In contrast, the small case shows only a negligible variation. No electron density variation is visible when changing the baffle, putting once again the cases far from what is predicted by the TMP (figure 4.8). It can be concluded that only the electron temperature presents a significant variation going very close to what the TPM predicts when the divertor closure is changed. Modelling outputs can help to understand what mechanism leads to this temperature reduction. Figure 4.11 shows the total Deuterium and Carbon density with the real outer baffle (top) and with that longer (bottom). Note that for the large and extreme cases, both densities increase in the divertor region, particularly in the SOL shadowed by the longer outer baffle. This increase is consistent with the compression factor seen before. Figure 4.12 on the top shows the total ionisation source, S_i. In large and extreme cases, there is a spatial extension along the outer leg of the power lost by radiation, and the ionisation peak is reduced in front of the wall. All of these variations, due to the elongation of the outer baffle, lead to the reduction of the electron temperature, reducing also the power loaded on the outer target. The latter is less than about 25% and 30% for the large and extreme cases, respectively. Note that 80% of the reduction is due to Carbon and Deuterium radiation. On the contrary, for the small case, the longer baffle has no significant impact, presenting only a small increase of n_C (fig. 4.11) and of the radiation with the ionisation peak staying in front of the target (fig. 4.12 top). The momentum sink (S_g) due to the charge-exchange phenomena (CX) is also investigated. Figure 4.12 on the bottom shows that the longer baffle increases CX in large and extreme cases with a consequent pressure change. Defining the pressure drop as

$$p_{drop} = p_{tot,t}/p_{tot,u}$$

where t stays for target and u for upstream, its value changes with the longer baffle from 0.5 to 0.15 for the large and from 0.7 to 0.29 for the extreme case. For the small case no drop is present, i.e. $p_{drop} \sim 1$. In figure 4.13 is shown the J_{sat}, T_e and $q_{\parallel}$ peaks at the outer target as a function of $n_{e,sep}$, useful to study the detachment threshold. On the top are the results obtained with the real baffle, and on the bottom are the ones with the longer baffle. The black horizontal dashed line in T_e plots highlights the detachment threshold. The small R_t case does not exhibit significant differences when using either baffle, so the focus will be on describing the large and extreme cases. For these $J_{sat,peak}$ loses the quadratic dependence on $n_{e,sep}$, expected from the modified TPM, with both types of baffles, in particular when $T_{e,peak}$ drops to 10-5 eV. At these values, volumetric power and pressure losses become significant, and these phenomena are not accounted for in the TPM. The longer baffle allows the achievement of the maximum value of $J_{sat,peak}$ at lower density, staying then approximately constant. The heat flux peak, $q_{\parallel}$, with both types of baffles, drops more quickly for the extreme case due to the increase of R_t.
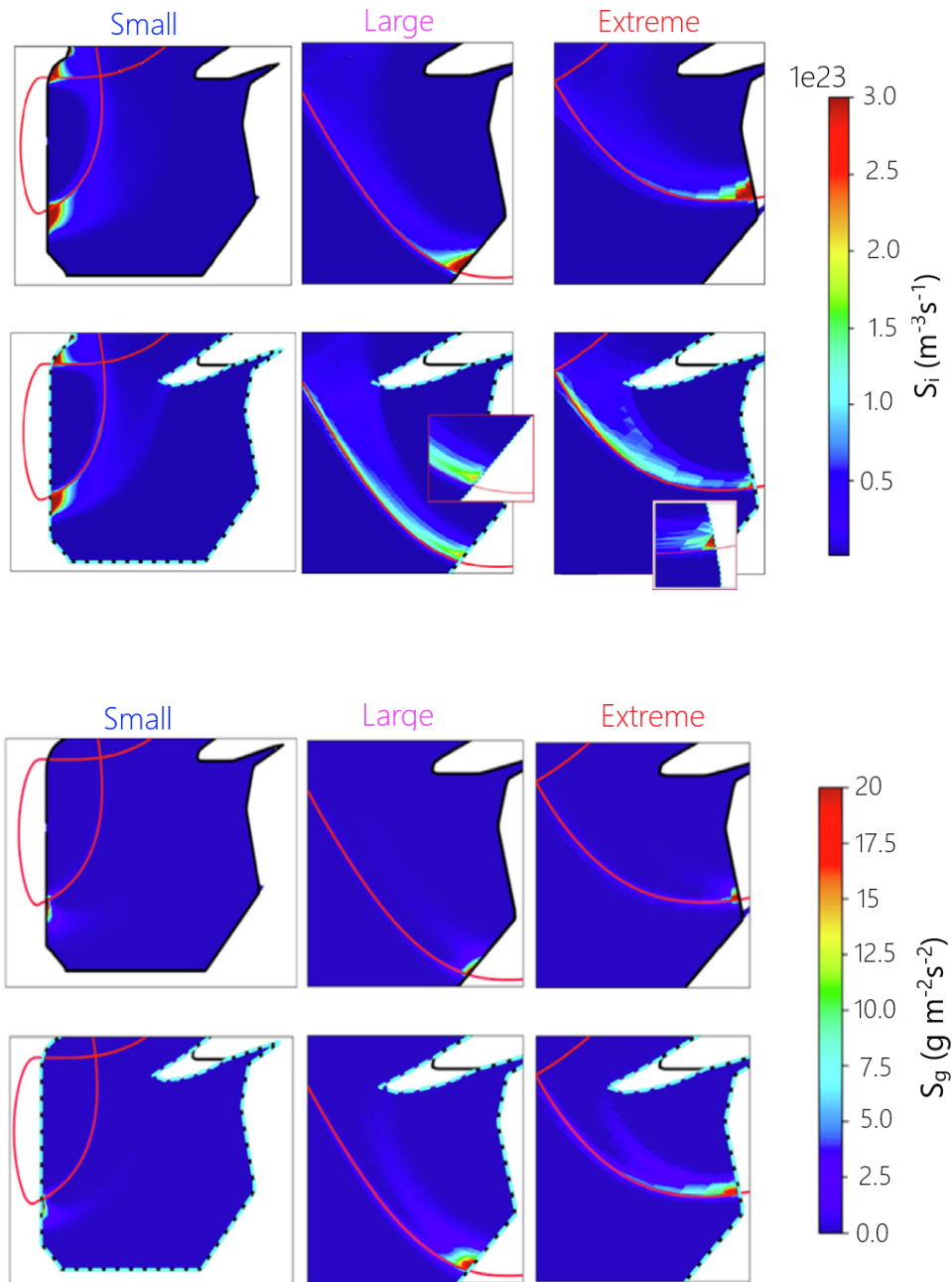
Figure 4.12: 2D divertor colour plot of the total ionisation source, S_i, and total momentum sink S_g with the actual outer baffle (top) and longer outer baffle (bottom). Only the outer leg and strike point, where most of the changes appear, are shown for the large and extreme. [61]

The lower target peak temperature for large R_t, which is in contrast with theory prediction, could be related to the local radiation losses of carbon and deuterium around the strike points influenced by the geometry of the divertor, and also to the different f_x and β that it has compared to the large case.

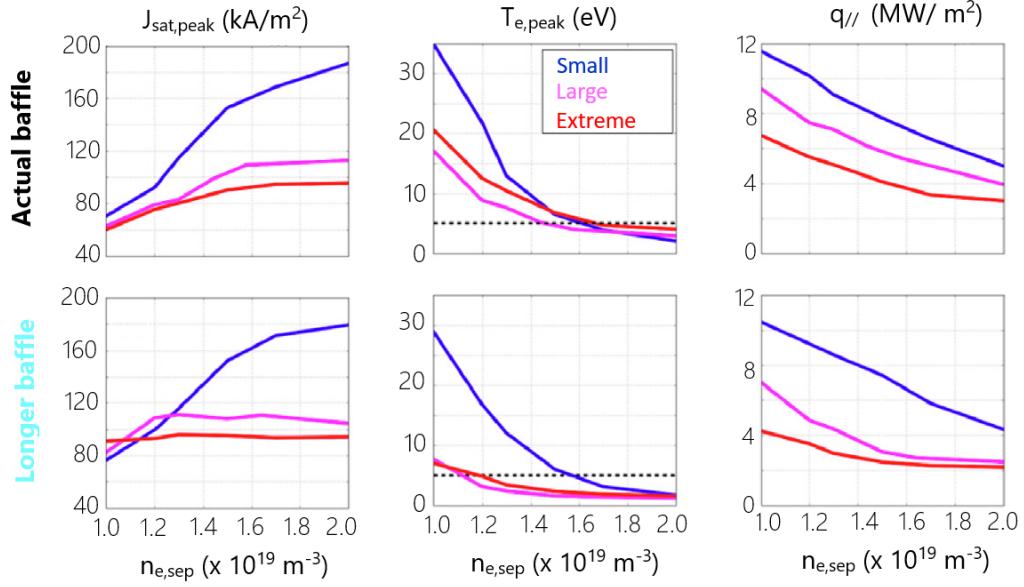**Figure 4.13:** Peaks at the outer target of saturation current, $J_{sat,peak}$, electron temperature, $T_{e,peak}$ and heat parallel flux, $q_{\parallel}$, as function of the separatrix density. With the actual baffle (top) and the longer one (bottom). Detachment threshold is highlighted in T_e plots with a horizontal dashed line. [61]

4.3 Chapter conclusions

Transport study with SOLEDGE2D-EIRENE indicates that the larger R_t configuration in TCV does not fully conform to the modified TPM predictions. This discrepancy is partially attributed to the inadequate confinement of neutral deuterium and carbon particles in the divertor region with the current outer baffle design. The length of the baffle must be extended to realise the advantageous effects of the Super-X configuration. Simulations of cases with a higher compression factor for larger R_t values reveal a corresponding 50% reduction in electron temperature at the target, in line with the predictions of the modified TPM. However, the particle flux does not increase as anticipated. The study indicates that this disparity between simulations and the model could be attributed to power and momentum losses, which are not accounted for in the modified TPM. Furthermore, SOLEDGE simulations reveal that particle fluxes begin to deviate from the predictions of the modified TPM at lower densities when the longer outer baffle is considered, as compared to the experimental cases. This deviation results in a reduction in the onset density for detachment. The results obtained motivate the baffle radius extension in real TCV experiments to study the Super-X configuration. It is worth noting that the extreme R_t case exhibits a similar effect, but it appears to have less favourable conditions at the target compared to the large R_t case. It is likely due to other factors, such as the variation in the β angle to the wall. Therefore, further research is needed to explore the potential benefits of extending the R_t in this manner.

Chapter 5

Core-divertor performance compatibility

Magnetic fusion devices must combine high core confinement to max-imise fusion reactions with divertor plasma conditions compatible with the long life expectancy of PFCs. Referring to the H-mode (section 1.2.1), the pedestal density top is an important indicator of the quality of the confinement. In contrast, density at the separatrix is a crucial factor for the divertor regime. For this reason, different studies are dedicated to the relation between $n_{e,sep}$ and $n_{e,ped}$ [53, 80, 29, 17]. This chapter presents the study done with the code SOLEGE2D-EIRENE to understand how to make edge simulations to enhance the existing database of $n_{e,sep}/n_{e,ped}$ based on experiments. The idea is to start with real pulses and then make simulations changing some input parameters. The analysis uses JET experiments performed in Vertical-Vertical (V-V) and Corner-Corner (C-C) divertor configurations.

5.1 Creating a simulations database

The study here presented takes inspiration from analysis in reference [3] and [17] that obtain scaling laws using JET H-mode pulses:

$$n_{e,sep}/n_{e,ped}^{0.95} \propto P_{SOL}^{0.15} I_p^{-0.33} B_T^{-0.68}$$

$$n_{e,sep}/n_{e,ped} \propto P_{in,tot}^{0.13} I_p^{-0.59}$$

The scaling laws above depend only on engineering parameters: the power entering the SOL (P_{SOL}), the plasma current (I_p), the toroidal magnetic field (B_T), and the total input power ($P_{in,tot}$). The first was obtained for a single type of "strike

point configuration" (Corner-Corner). In contrast, the second one derived from the analysis of different types (Corner-Corner, Vertical-Horizontal, Vertical-Vertical). The aim of studies in [3, 17] is to investigate the possibility of having a scaling law depending only on a few engineering parameters as a guide to foresee the ratio between $n_{e,sep}$ and $n_{e,ped}$. It does not exclude the extrapolation in the future of ad hoc scaling laws, such as, for example, for different divertor geometries and strike point locations. Correlation depending on engineering parameters allows us to understand how to control the two density quantities to optimise and foresee future experiments.

The final idea of the study explained in this chapter is to improve the experimental scaling laws of $n_{e,sep}/n_{e,ped}$ using the transport code SOLEDGE2D-EIRENE for an extensive range of values of input engineering parameters (P_{SOL}, I_p, B_T, $P_{in,tot}$) without doing experiments. The starting point to create a simulation database is to understand which edge diffusivity must be used, leading us to the following questions:

- Have pulses with similar input parameters but different divertor configurations, such as V-V and C-C, the same edge transport?

- Have pulses with same divertor configuration but different P_{SOL} the same edge transport?

- How crucial is it to incorporate the actual pumping geometry into our modelling?

In the following sections will be answers to all these questions.

5.1.1 Experimental analysis and modelling setup

For each pulse we choose, an interval time in which global parameters are stationary; here, experimental data averaged over 200 ms and the EFIT equilibrium reconstruction [9] are used. Modelling with SOLEDGE2D-EIRENE is done by imposing real PFCs geometry and gas injector poloidal position [44]. Among the input parameters of the code are the particle puffing rate, which is set equal to the experimental one, and the power entering the inner boundary of the simulation domain. In the analysed case, the internal domain limit is around $\rho_{pol} \approx 0.9 \pm 0.05$, inside the pedestal density top. Since only a negligible portion of the plasma core is included, the radiation within the core is subtracted from the total experimental input power. The radiation from impurities within the modelling domain is also excluded because we work with pure deuterium. Plasma radiation is evaluated

Configuration	Pulse number	I_{plasma} (MA)	B_t (T)	P_{SOL} (MW)	D_2 puff (D_2/s)	NBI (electrons/s)
C-C	94210	2.47	2.8	8.4	15.7×10^{21}	1.5×10^{21}
V-V	85262	2.48	2.7	6.9	22.6×10^{21}	1.7×10^{21}

Table 5.1: Main features of the two pulses in analysis.

using tomographic reconstructions of the bolometer measurements [41]. The resulting input power for our simulation, which will be named P_{SOL} from now on, is

$$P_{SOL} = P_{tot,in} - P_{core,rad} - P_{impurity,rad}$$

where the total input power $P_{tot,in}$ is the sum of ohmic power and that auxiliary, which in these cases can be NBI[1] and/or ICRH[2].

Other essential input parameters of the code are the perpendicular transport coefficients for density and energy, named D and χ, respectively. This work did not estimate the power distribution between ions and electrons, so the same energy diffusion, i.e. $\chi_e = \chi_i$, is applied. Transport coefficients are tuned to reproduce electron density and temperature on the outer mid-plane from high-resolution Thomson scattering (HRTS). Thanks to its high spatial resolution, this diagnostic allows a good transport estimation, particularly in the near-SOL and pedestal region. The separatrix position is set where T_e equals 100 eV, in agreement with the JET convention. There are more accurate methods to locate the separatrix position, as, for example, the power balance approach [45], but this will be implemented in the next steps of this study.

5.1.2 Impact of divertor configuration on transport

The main difference between the two is the magnetic divertor configuration. One has the strike points on the vertical targets of the divertor, V-V configuration (JPN[3] 85262). In contrast, the other one has the strike points on the low horizontal targets, C-C configuration (JPN 94210). Figure 5.1 shows the two cases in the poloidal section. Here, the gas injector positions used for the simulation (green) correspond to the actual poloidal ones. Instead, the pumping surfaces (blue) are placed at the opening between the divertor region and that of the sub-divertor. The sub-divertor area, where the real pump is located, is not included in the studies presented in this section (see section 5.1.5 for its inclusion). Electron density and temperature profiles are fitted using a modified hyperbolic tangent to have

---

[1]NBI=Neutral-beam injection
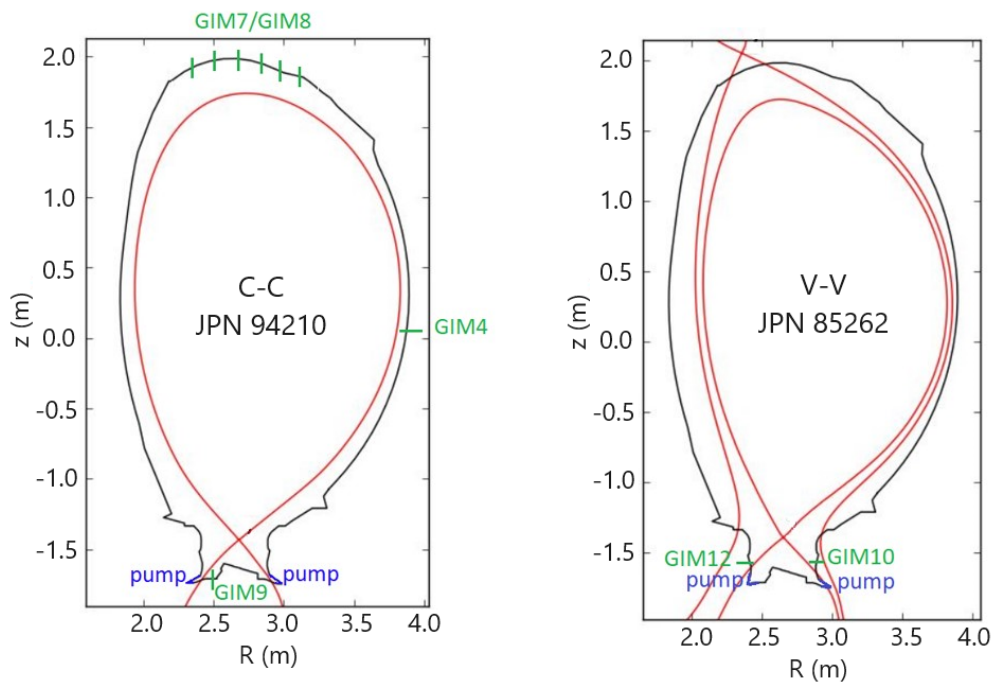[2]ICRH=Ion Cyclotron Resonance Heating
[3]JPN=JET pulse number

Figure 5.1: JET poloidal cross-section with LCFS of the equilibria (in red). On the left is the Corner-Corner, and on the right is the Vertical-Vertical pulse. The pumps are in blue, and the injector of D_2 is in green.
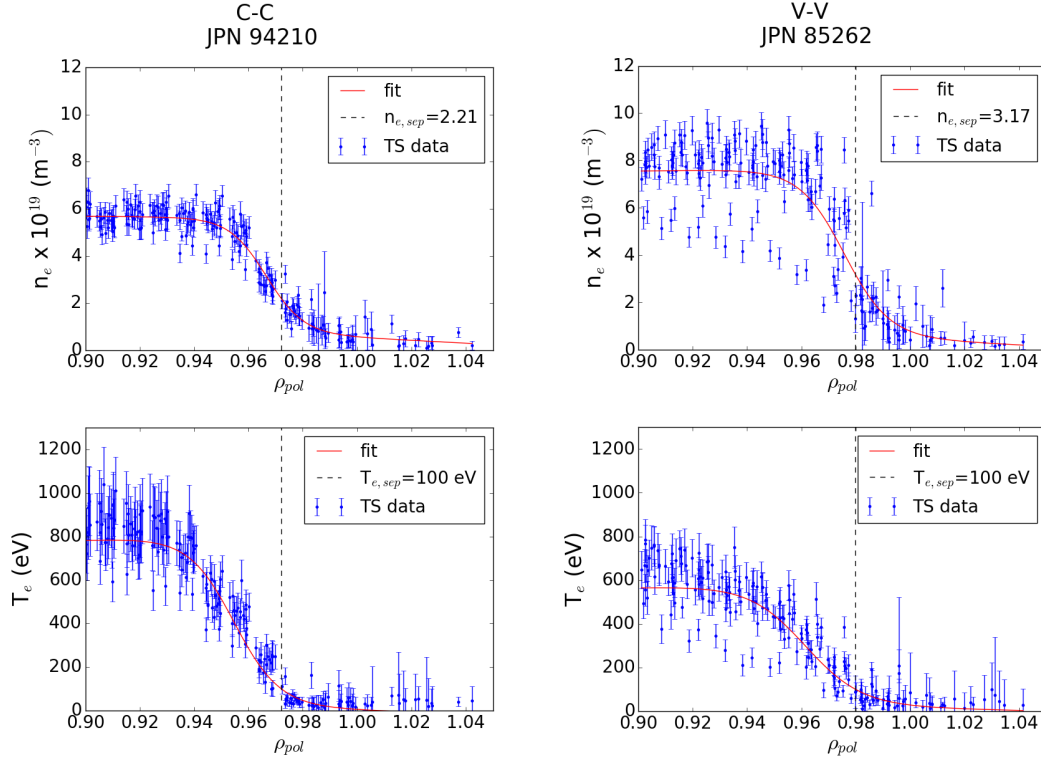
Figure 5.2: Electron density and temperature profiles on the outer mid-plane. Thomson scattering data with error bars in blue, fitted data in red. The data far from the mean values are due to ELMs (see section 1.3). C-C configuration on the left, V-V on the right.

a good approximation of what it is expected to reproduce with the modelling, in particular at the separatrix and pedestal top, see figure 5.2.

Figure 5.3 shows the matching between simulation and TS data for the C-C case. By applying specific diffusion coefficients, we have replicated data along the outer mid-plane: simulated profiles (in blue) are in excellent agreement with experimental data (in green) and with the fit (in red) as well. The particle and energy diffusion coefficients, D and $\chi_{i,e}$, have been modulated along the ρ_{pol} coordinate to match n_e and T_e profiles from the inner boundary of the simulation, $\rho_{pol} \approx 0.95$, up to the wall. The diffusion decreases from the core going towards the separatrix, reaching values of $D = 0.04$ and $\chi_{i,e} = 0.4$, and then increases again in the near-SOL reaching plateau values of $D_{max} = 2.7$ and $\chi_{i,e} = 2.4$ in the far-SOL.

Ad-hoc perpendicular transport has also been tuned for the V-V pulse. Figure 5.4 illustrates the comparison between the two cases in analysis with specific diffusivity that allows the reproduction of experimental data. For both pulses, the density diffusion decreases from the core going towards the separatrix, and then,
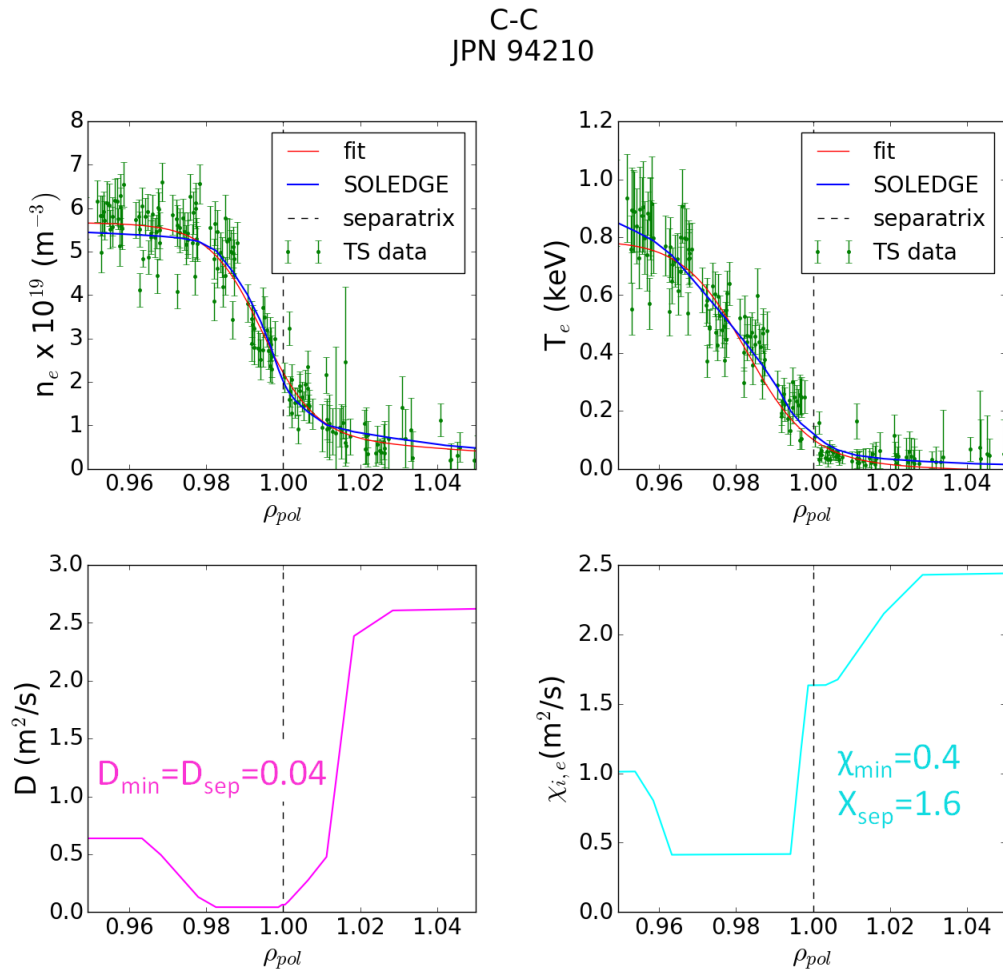
Figure 5.3: Matching between TS and SOLEDGE modelling. The electron density and particle diffusion coefficient profiles are on the left, and the electron temperature is on the right with the energy diffusion coefficient.
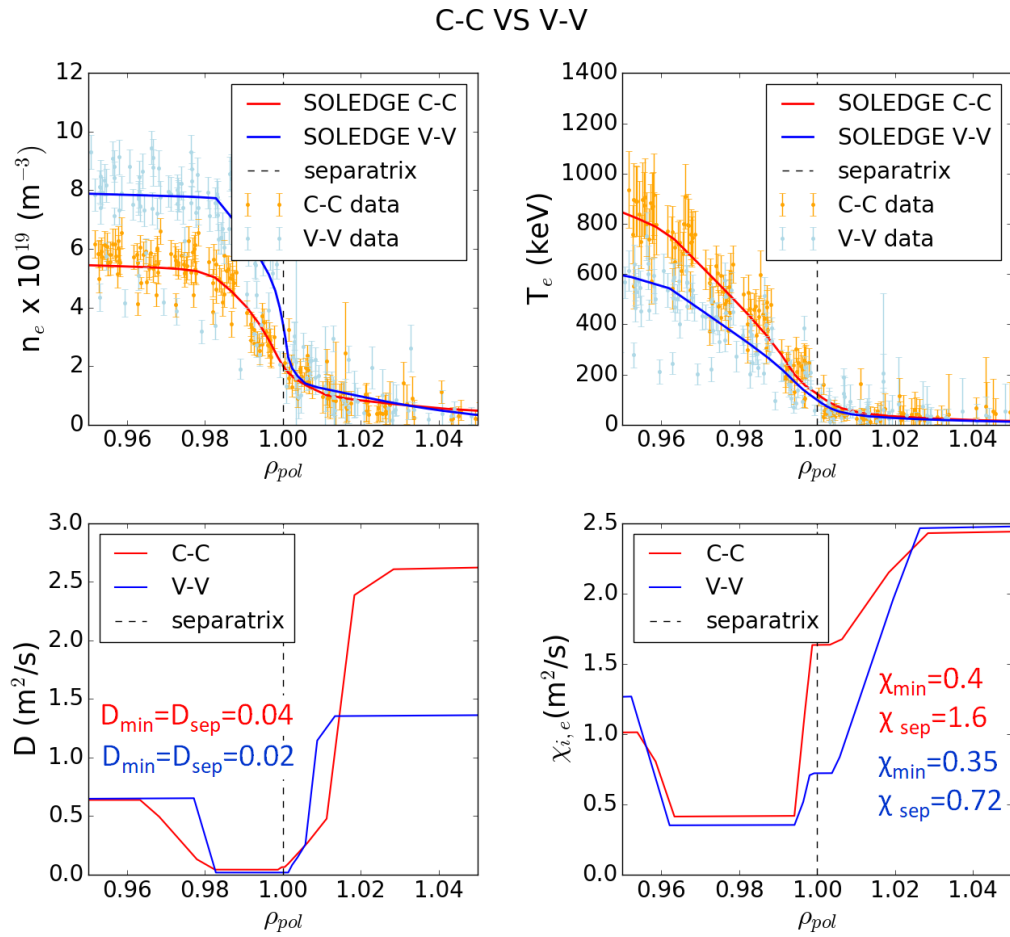
Figure 5.4: Matching between TS and modelled profiles for V-V and C-C cases. On the left are the electron density and particle diffusion coefficient profiles, and on the right, the electron temperature with the energy diffusivity.

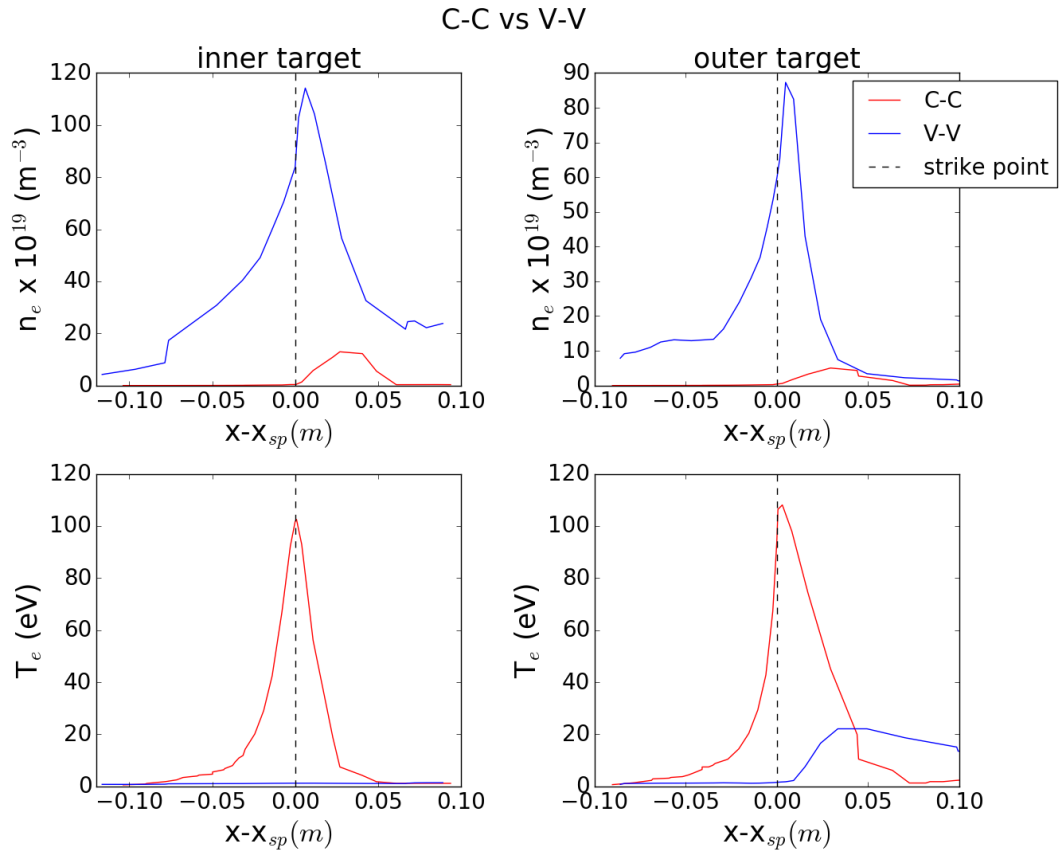**Figure 5.5:** SOLEDGE2D-EIRENE electron density and temperature profiles on targets obtained reproducing the experimental TS data on the outer mid-plane. In red is the Corner-Corner, and in blue is the Vertical-Vertical configuration.
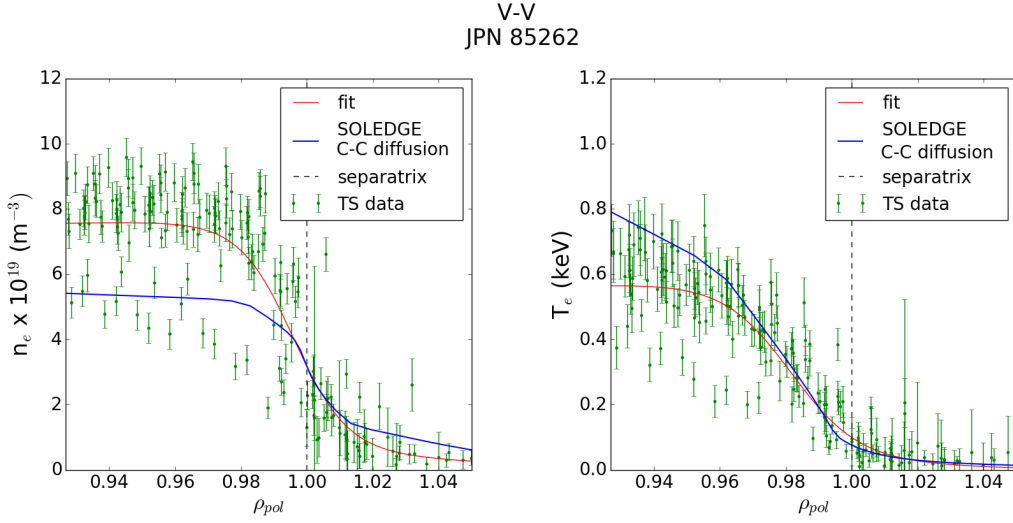
Figure 5.6: Outer mid-plane profiles of the V-V pulse with the C-C diffusivity constraint.

it increases in the near-SOL, faster for the V-V case, reaching plateau values in the far-SOL. Overall, V-V has half diffusion to the C-C pulse. In particular, the difference in D in the transport barrier causes a higher density at the pedestal top in the V-V case. On the other hand, the energy diffusion, which is different around the separatrix, $\chi_{vv} \approx \frac{1}{2}\chi_{cc}$, causes two different divertor regimes: the C-C case is in the attached regime while the V-V case is in detachment. Suppose the target simulation corresponds to reality by comparing these two pulses. In that case, drawing general conclusions on which configurations are better to achieve detachment is tough. It is advisable to compare two pulses with similar input parameters and the same separatrix density, which significantly influences the target condition (see the two-point model in section 1.3.1.1). It will be done in the near future.

5.1.3 Transport discrepancy investigation

Because of the similar input parameters (see table 5.1), such a big difference in perpendicular transport between the two cases was not expected; the starting point of the investigation was applying the C-C transport to the V-V case with all other inputs necessary for the simulation specific to the V-V case itself, result in figure 5.6. As expected, the C-C diffusivity cannot reproduce the outer mid-plane profiles of the V-V case. In particular, n_e is well reproduced only around the separatrix but is lower in the core and doubled in the SOL, while T_e is matched in the far-SOL but is smaller around the separatrix and bigger in the core.

All varying input parameters were systematically tested (see table 5.1) to ascertain whether transport is the sole and definitive factor causing the notable differences between the two cases, a: C-C diffusion coefficients were applied to V-V also imposing the C-C input parameter values, one at a time, coupled together and then all together. If some of these inputs enable the reproduction of V-V experimental profiles, then the difference in diffusion that simulations show (section 5.1.2) hides, in reality, other causes. Between input parameters, we also tested the influence of the pumping speed. In this case, because of the unreal position that pumps have in the simulation domain (as explained in section 5.1.1), the albedo is fixed to that of the C-C case, i.e. 3%, and let the code adjust the value of the pumping speed to match this value. In fact, in EIRENE code, these two quantities are linked with the following relation [78]

$$v_{pump} = A \cdot (1 - \mathscr{R}) \cdot 3.638 \cdot \sqrt{T/m} \quad [l/s] \tag{5.1}$$

where $1 - \mathscr{R}$ is the albedo with $\mathscr{R}$ that is the absorption probability, A is the area seen by particles, T an m are the temperature and mass of the particles. Figure 5.7 shows how pedestal and separatrix density consequently change, imposing different constraints: on y-axes, there are n_{ped} (top) and n_{sep} (bottom) while on the x-axes there are the C-C inputs applied to the V-V case. The horizontal lines highlight experimental n_{ped} and n_{sep} of C-C (dashed blue line) and V-V (solid red line). The figure above shows that the n_{ped} consistently remains close to the experimental C-C value, indicating that differences in these parameters between the two configurations are not the cause of the discrepancy. The density at the separatrix, shown in the figure below, is well reproduced using C-C diffusion when constraints are applied to NBI and P_{SOL}, while n_{sep} decreases by changing the puffing. The most significant reduction occurs when the pumping speed is changed. In this case, where v_{pump} goes from 60 m^3/s of the V-V case with its transport to 92 m^3/s to match the C-C albedo of 3%, n_{sep} approaches the C-C value, decreasing further when is combined with all other parameters. Figure 5.8 shows the profiles obtained by applying all the input parameters and the albedo of the C-C case to the V-V equilibrium. Density results to be approximately halved for each ρ_{pol}. Meanwhile, the temperature is more or less the same from $\rho_{pol} = 0.98$ until the wall but is doubled in the core. Profiles are more similar to those of the C-C case than the V-V experimental data.

Focusing on the divertor region, it is clear from simulation results that NBI, P_{SOL}, and puffing constraints do not change anything, both with and without the albedo set to the C-C value. For this reason, these cases will be combined, referring to them as "Diffusion" (Diff) and "Diff+v_{pump}" when the albedo is fixed. Figure 5.9 shows the outer target's electron density and temperature profiles. It should be kept in mind that experimental data are unavailable in this region, so our study

Figure 5.7: All the V-V cases have the C-C diffusion coefficient. The other input parameters are changed one at a time, coupled and all together.

Figure 5.8: Results obtained for the V-V case applying all the input parameters and albedo of the C-C pulse.
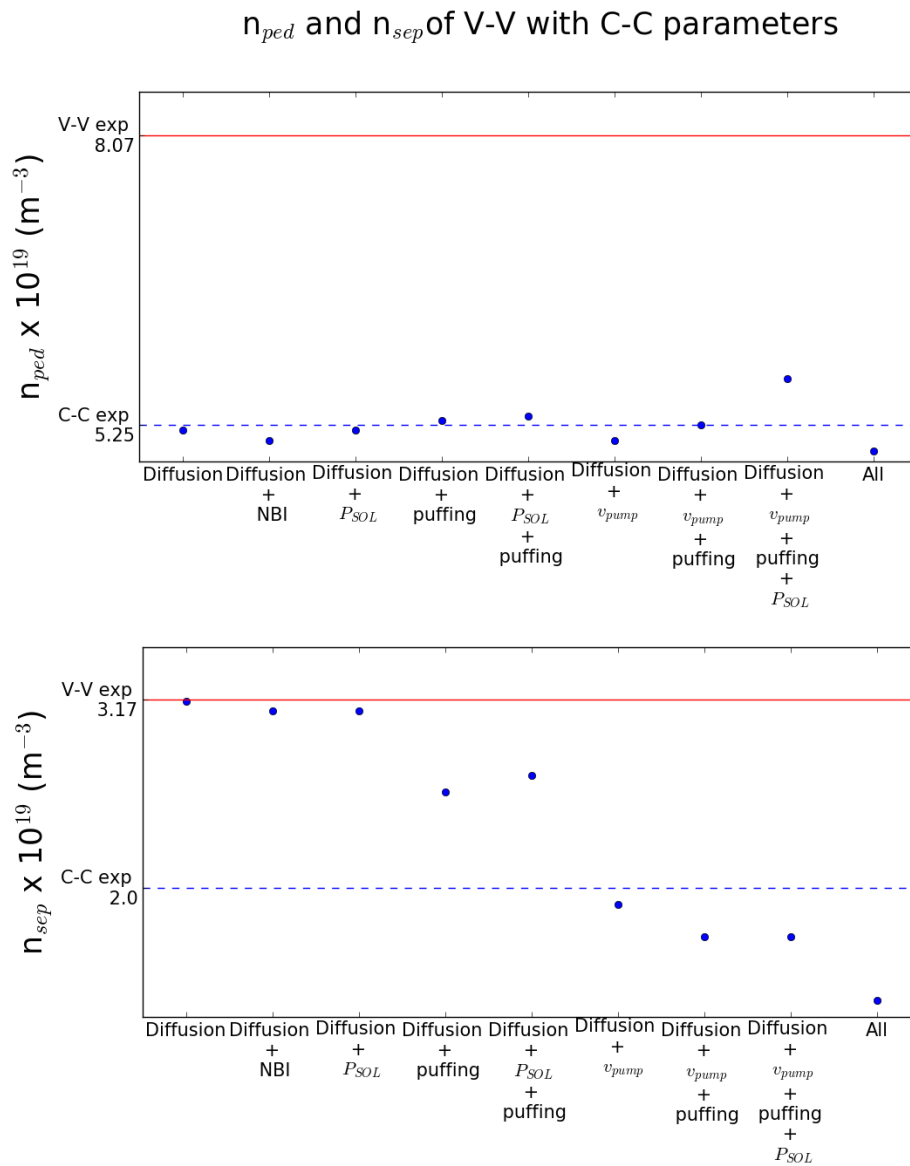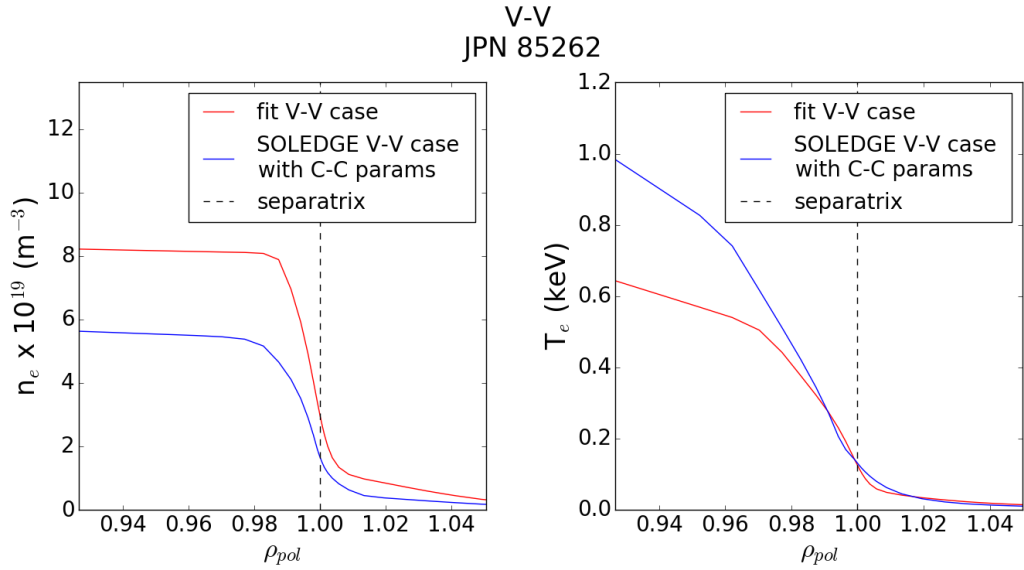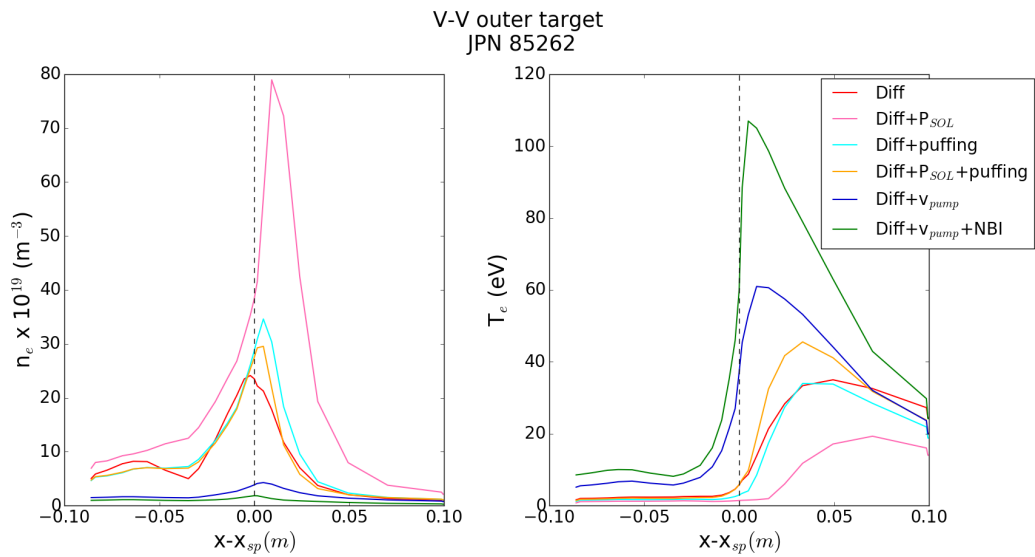

Figure 5.9: All the simulated V-V cases have the C-C diffusivity. The other input parameters are changed one at a time, coupled and all together, putting the corresponding C-C values to the V-V case. "Diff" stays for diffusion.
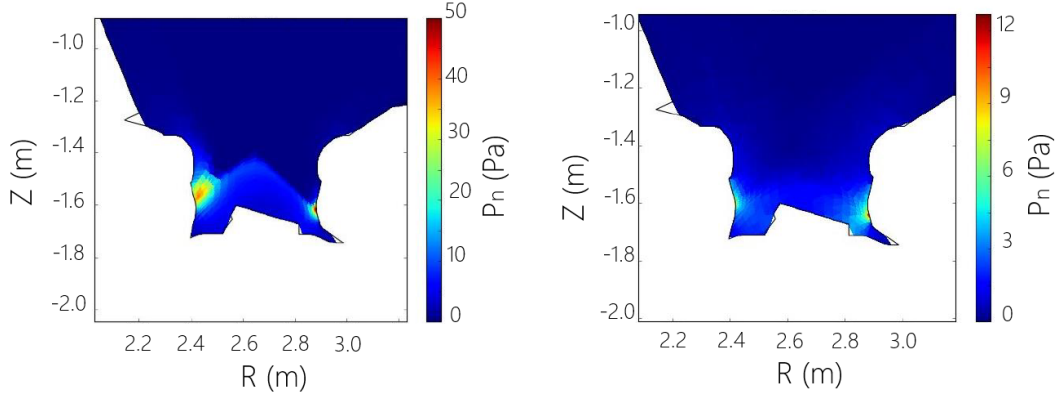
Figure 5.10: 2D view of the neutral pressure, P_n, in the divertor region. On the left is the V-V case with only the C-C diffusion constraint, on the right also with the v_{pump} value of C-C. Increasing the pumping speed is equivalent to reducing the recycling, so the neutral pressure decreases.

is not interpretive but an indicator of how the parameters influence the target behaviour. Starting from the case with only C-C transport imposed (in red), which is in high-recycling condition with the heat concentrated on the right, it is evident that parameters have a big role in determining the divertor regime. Increasing P_{SOL} up to the C-C case value (profiles in pink), target behaviours change going to detached condition ($T_{e,sp} < 5$ eV). The same, but with a bigger temperature on the right of the strike point, occurs if the puffing is changed (profiles in cyan) and also imposing the P_{SOL} of C-C (profiles in orange), the divertor returns in the high-recycling regime. Setting albedo to the C-C value, v_{pump} increases and the neutral pressure in the divertor region decreases, turning the divertor in the attached regime, see figure 5.10. Finally, putting all the parameters equal to the C-C case (profiles in green), the attached regime becomes stronger.

To conclude, the discrepancy between the experimental and modelled V-V cases can not be explained or justified by the differences in input parameters. The hypothesis is that the two divertor configurations, C-C and V-V, have different transport. Moreover, it has to be taken into account that these parameters have a significant influence on the target condition; therefore, for future studies, it is mandatory to have experimental data in the target region: this will allow for improved transport parameters with a consequent better understanding of the phenomena involved. The pumping velocity is another variable better to fix to the actual value and with the real pump position. For this reason, the sub-divertor region has been included in the study presented in section 5.1.5.

Configuration	Pulse number	I_{plasma} (MA)	B_t (T)	P_{SOL} (MW)	D_2 puff (e/s)	NBI (electrons/s)
C-C	94210	2.47	2.8	8.4	15.7×10^{21}	1.5×10^{21}
C-C	92296	2.7	2.8	24,4	13.6×10^{21}	$2,67 \times 10^{21}$

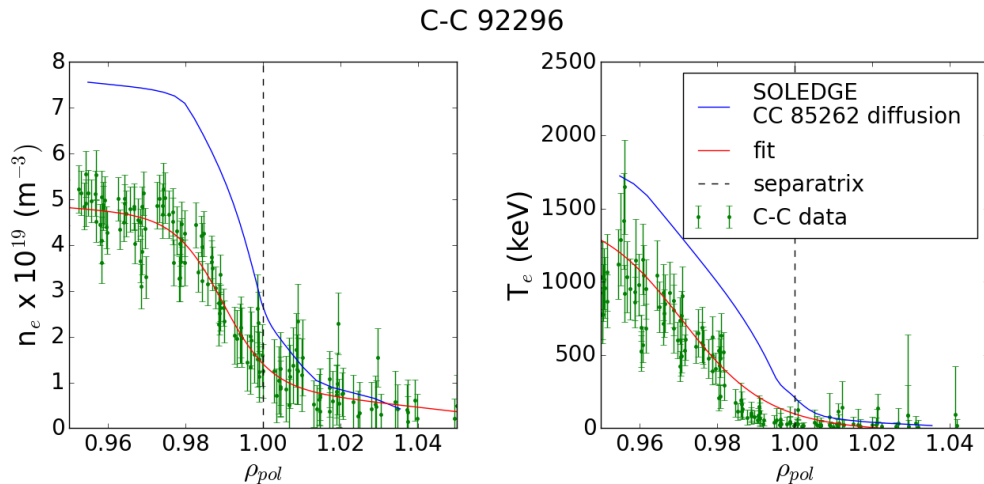**Table 5.2:** Main features of the two pulses in analysis.

Figure 5.11: Results obtained for the JPN 92296 applying JPN 85262 diffusivity.

5.1.4   Relevance of the input power

Before, two different magnetic divertor shape configurations were compared, but what about the diffusion for the same configuration but with different P_{SOL}? Two C-C pulses with similar input parameters are studied: JPN 94210, first analysed, with $P_{SOL} = 8.4$ MW, and JPN 92296, with a bigger P_{SOL} equal to 24.4 MW. See table 5.2 for details. Applying the perpendicular transport of JPN 94210 to JPN 92296, the electron density and temperature profiles on the outer mid-plane are not well reproduced. The conclusion is that having different P_{SOL} for the same magnetic divertor configuration leads to a different perpendicular transport. What is found here is not very surprising because also the simple Two-point model describes the dependence of $\chi_\perp$ to P_{SOL} (see equation 1.12). Therefore, it will be apparent to consider the dependence of transport parameters on the input power when it expands the $n_{e,sep}/n_{e,ped}$ database by using SOLEDGE.

5.1.5   Modelling with sub-divertor and cryopump

JET pulses are usually modelled considering absorbing neutrals and ions in the corners of the divertor, as shown in figure 5.1. Working in this way, i.e. setting the
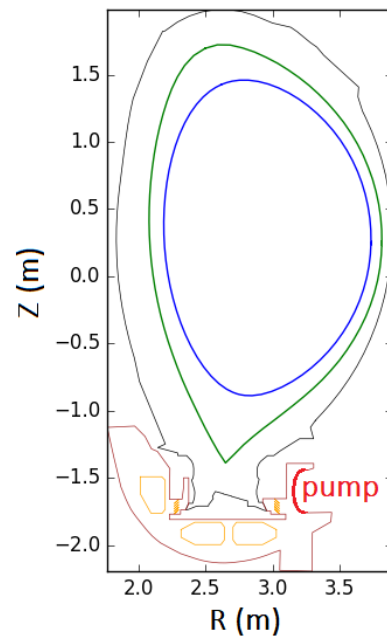
Figure 5.12: Poloidal section of JET. The inner boundary of the simulation domain is in blue, and the LCFS is in green (JPN 85262). In orange and brown is the sub-divertor, where the cryopump is highlighted in red.
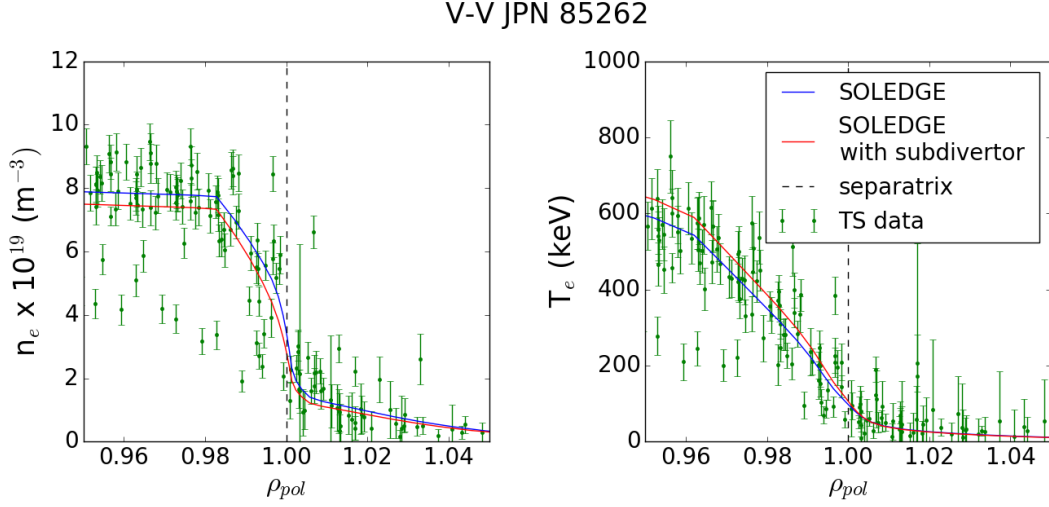
Figure 5.13: Match between experimental n_e and T_e profiles (in green) on OMP and that simulated for JPN 85262. In the blue simulation, results were obtained without a sub-divertor region and considering neutrals and ions absorption in the corners of the diverter; in red, results included the sub-divertor and setting the cryopump in its real poloidal position.

albedo and leaving the pumping velocity free to change by simulation evolution (see equation 5.1), it is possible to have an idea of the recycling in the divertor.

In the study presented here, the sub-divertor geometry is included in the simulation domain of the V-V pulse #85262 to put pumps in the proper poloidal position and provide better modelling of gas pumping. In the sub-divertor of JET, there is a cryopump system consisting of two independent 180° elements. The pump operation is very stable and unaffected by all kinds of plasma operation conditions [69]. Figure 5.12 shows the poloidal position of the cryopump set in the simulation domain, which corresponds to the real location. In this analysis, the albedo is left free to change following plasma evolution, setting the pumping velocity to its real value[4] of 200 m³/s. This simulation was compared with the old one performed for the same pulse without including the sub-divertor to see where and how this setup influences the results (section 5.1.3). Figure 5.13 shows that the diffusivity found to match experimental profiles with the old setting also allows us to reproduce them in this new case. What changes, on the other hand, is the divertor behaviour. As figure 5.14 shows, from the old to the new case, n_e decreases on the inner target while temperature increases, decreasing the sharpness of the detachment. On the

---

[4]It is assumed here that the velocity is constant, considering that neutrals in the sub-divertor are thermalised with the wall (room temperature).
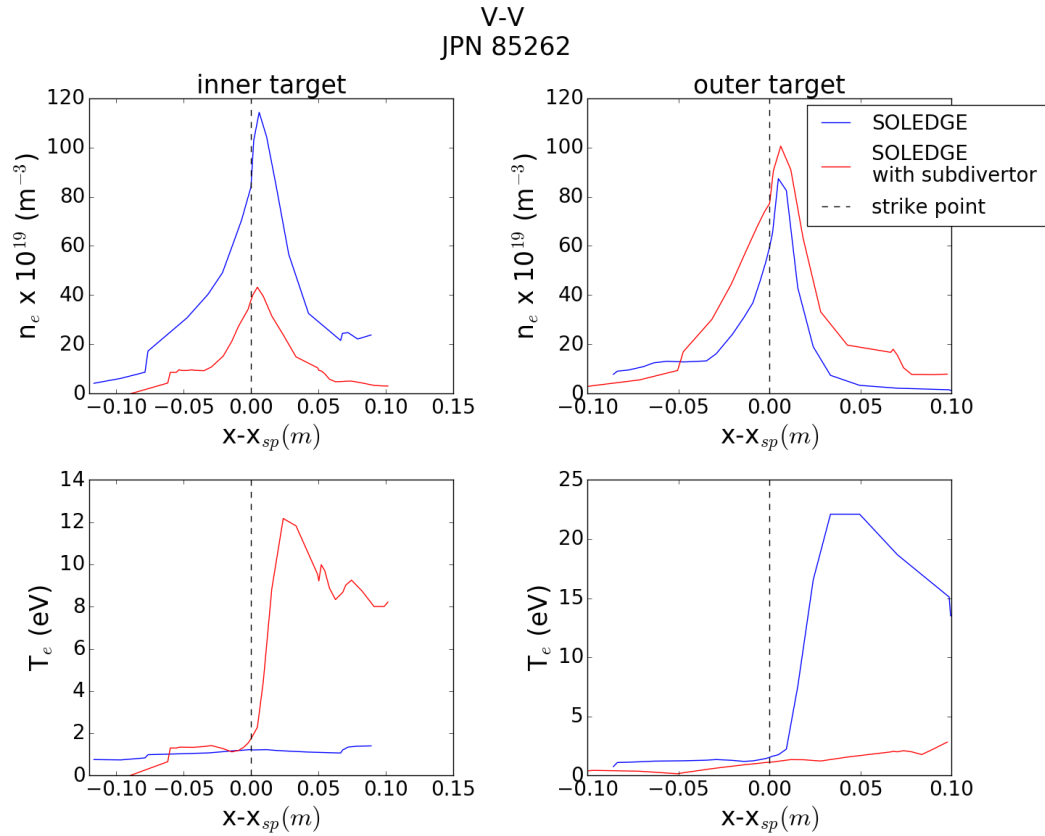
Figure 5.14: Electron density and temperature profiles at the strike points obtained for the JPN 85262 without sub-divertor (in blue) and with sub-divertor (in red). Negative values indicate the private region.

outer target, there is a slight increase in density and a sharp decrease in temperature, leading to a strong detached regime. Examining the overall temperature, it appears there is a redistribution of heat between the inner and outer target, which is the one closer to the pump. Once again, having data from this region would greatly enhance our understanding of the dynamics. However, it is clear from this analysis that incorporating the real divertor geometry and pumping speed yields different results, especially in the divertor region.

5.2 Chapter conclusion

The final aim of this work is to be able to conduct edge simulations to study the relationship between density at the pedestal top and at the separatrix using the code SOLEDGE2D-EIRENE independently of experimental data. First, it is necessary to understand which edge transport to use. For this reason, it is investigated the possibility of applying the same perpendicular transport to modelled very similar pulses with different divertor configurations, Vertical-Vertical and Corner-Corner (section 5.1.3), and different P_{SOL} (section 5.1.4). These analyses lead us to hypothesise that the two divertor configurations, C-C and V-V, have different diffusivity, excluding the possibility of modelling a real experiment and then simulating cases using the same transport simply changing, for example, the power entering the SOL. This transport study confirms what we expected from observing n_e and T_e experimental profiles on the outer mid-plane. In fact, the plasma shapes of the two pulses, shown in figure 5.1, are somewhat different, partially due to the different divertor configurations: Vertical-Vertical and Corner-Corner. It is clear that the temperature and density gradients in the edge, which are strictly correlated to the transport, depend on the plasma shape. The influence of including the sub-divertor region in the simulation domain and of placing the pumps in their actual positions with their real pumping velocities is also investigated. Including these elements makes a significant difference in the divertor's behaviour and regime.

All the studies presented here emphasise the importance of having data in the divertor region to understand how to tune transport and to be able to interpret as close to reality as possible. Access to these data allows us to understand whether the modelling accurately represents the target situation. If the interpretation of the transport were correct, it would provide the essential information that the V-V configuration would be more favourable for reaching the detachment regime than the C-C, as figure 5.5 shows.

To conclude, it can be affirmed that creating a simulation database is not straightforward. However, the studies presented here allow us to take a step forward in understanding how different factors influence transport. Analyses have shown that divertor configuration, due to its influence on the plasma shape, should also be included among the engineering parameters in this kind of study. Similarly, the placement of pumps and the shape of the divertor also impact, so it would not be surprising to observe different $n_{e,sep}/n_e, ped$ scalings across other machines.

Chapter 6

Conclusions

Plasma exhaust has been identified as a significant challenge in realising magnetic confinement fusion. As the size of tokamaks and the duration of pulse lengths increase, it will become even more challenging to manage power losses. The work presented here is dedicated to studying the plasma at the edge, in SOL and divertor region, with the ultimate goal of contributing to developing and improving current and future devices. In particular, different magnetic configurations have been studied to understand their possible advantages from the power exhaust point of view. Our studies have been performed both by analysing experimental data and by modelling using the 2D fluid edge code SOLEDGE2D-EIRENE to improve the knowledge of three relevant topics of power exhaust: ELMs mitigation using Negative Triangularity, detachment achievement by ADCs and finally, the relation between SOL and pedestal density.

One problem in PEX panorama is the Edge Localised Modes, which can lead to large, uncontrolled heat fluxes at the machine targets. Among the most promising solutions for this problem is the Negative Triangularity (NT) configuration. TCV experiments have been analysed to understand, in particular, the energy and particle edge transport. The studies have shown that NT affects transport specifically in the edge plasma, highlighting the presence of a little barrier around the separatrix. This small barrier probably has a role in the good core condition achievable by NT with less input power than the PT H-mode. Moreover, it was found that the NT edge transport stands between the PT low-confinement and high-confinement mode, with better performance than the reactor-relevant PT H-mode. The good power exhaust and core conditions achievable without ELMs make NT an interesting configuration for future reactors. For this reason, the studies will be extended to other devices, AUG and DIII-D, to use modelling tools to predict the behaviour of NT plasmas in future devices, particularly for DTT. The analysis started on TCV with the code SOLEDGE3X will continue in parallel with the fluid simulations in order to have information about the turbulence features in NT compared

with the PT.

The detachment is one of the desirable regimes for future fusion reactors thanks to particle and heat flux reduction that allows to have on divertor plates. Among the advanced divertor magnetic configurations that aim to ease the achievement of the detachment is the Super-X Divertor (SXD) configuration. Our studies focused on understanding why, as experimental and modelling studies have shown in the past, SXD has shown lesser benefits than the theoretically modified Two-point model. TCV experiments were used to do the study. It is found that the discrepancy could be partially attributed to inadequate confinement of neutral deuterium and carbon particles achieved in the divertor region with the TCV current outer baffle design. The modelling shows that the length of the baffle must be extended to have the advantageous effects of the Super-X configuration. Moreover, simulations highlight the importance of power and momentum losses, physics phenomena that are not included in the theoretic model. These results will be considered in the TCV experimental campaign planned with a longer baffle.

Magnetic fusion devices must combine high core confinement to maximise fusion reactions with divertor plasma conditions compatible with the long life expectancy of plasma-facing components. Referring to the high-confinement mode in PT, the pedestal density top ($n_{e,ped}$) is an essential indicator of the quality of the confinement. In contrast, density at the separatrix ($n_{e,sep}$) is a crucial factor for the divertor regime. Correlating these two quantities through engineering parameters allows us to understand how to optimise and foresee future experiments. Our study aims to understand how to make edge simulations to enhance the existing experimental database of $n_{e,sep}/n_{e,ped}$. The code SOLEDGE2D-EIRENE and JET experiments performed in Vertical-Vertical and Corner-Corner divertor configurations have been used for the study. It has been found that generating a synthetic database from modelling is complex. However, the study allows us to take a step forward in understanding how different factors influence transport. The analyses have shown that among the engineering parameters to consider in experimental studies, divertor configuration should also be included because different divertor configurations have different transport. Similarly, the placement of pumps and the shape of the divertor have an impact as well, particularly the divertor's behaviour and regime. For this reason, it is necessary to include them in future analyses, and it would not be surprising to observe different $n_{e,sep}/n_e, ped$ scaling across different devices. Future analyses will allow us to extend the work and provide information on which is the more favourable divertor magnetic configuration to reach the detachment regime.

Ph.D activities: Education, papers & CO

Education and Training activities

- 2021 and 2022: Tutor activity in the General Physics laboratory of engineering courses (UNIPD) - 80 hours divided into laboratory assistance, supervision during the exam, and student reports revision.

- 2021-2023: Ph.D courses participation with corresponding exams:

  - Advanced Course on Plasma Physics and Diagnostics
  - Advanced Course on Plasma Control and CODAC
  - Advanced Course on Fusion Engineering and Technology

- 4-6 July 2022: Participation in the FuseNet PhD Event (Padova) with poster presentation: "Analysis of edge transport in L-mode negative triangularity TCV discharges"

Research activities

- 2021: Work within the WPTE/RT18 "Alternative divertor configuration"

- 2021-2022: Work within the WPTE/RT07 "Negative Triangularity scenarios as an alternative for DEMO" (one week on-site, see sec.6)

- 2022-2023: Work within the WPTE/RT22-02 "Physics understanding of alternatives to Type-I ELM regime"

- All three years (2021-2023): Work within the TSVV-02 "Theory, Simulation, Validation and Verification: Physics Properties of Strongly Shaped Configurations"

- All three years (2021-2023): Collaboration with IRFM laboratory (CEA) for deriving a scaling law for separatrix density as a function of engineering parameters.

All the work was always joined with regular updates from the different WP groups, and I followed different Eurofusion meetings about the Tokamak edge physics and simulations.

Periods abroad

- From 12th November to 9th December 2022 at IRFM (CEA, Cadarache, France): During my visit, I worked with the theory group on the numerical development of the turbulent code SOLEDGE3X-EIRENE as well as its application to TCV in perspective of DTT negative triangularity scenarios.

- One week in 2022 at IPP laboratory (Max-Planck-Institut für Plasmaphysik, Garching-German): Experimental campaign participation within the RT07 ("Negative Triangularity scenarios as an alternative for DEMO").

Conferences and Seminars

- 13-17/06/2022: 25th PSI (Korea but virtual): Participation with the poster "Analysis of edge transport in L-mode negative triangularity TCV discharges".

- 2022: Poster at the meeting "Technology Path to 2050" between ENI-JRA and MIT

- 03-07/07/2023 EPS Plasma Conference (Bordeaux, France): Participation with the poster "Multi-devices edge transport analysis of positive and negative D-shape plasmas in high power tokamak scenario"

- Once a year: TSVV2-02 annual meeting.
  The last one (2023) has been on-site at EPFL (Lausanne, Swiss)

- Once a year: Seminar meetings within the Joint Research Agreement (ENI-CNR)

Publications and Contributions

- P. Muscente et al.; Analysis of edge transport in L-mode negative triangularity TCV discharges; 2023; https://doi.org/10.1016/j.nme.2023, published on *Nuclear material and Energy*.

- C. Meineri et al.; Numerical study of fully baffled Super-X L-mode discharges on TCV; 2023; https://doi.org/10.1016/j.nme.2023.101383, *Nuclear material and Energy.*

Contributions

- A Balestri et al., "Experiments and gyrokinetic simulations of TCV plasmas with negative triangularity in view of DTT operation", Conference: 27th Joint EU-US Transport Task Force Meeting (TTF 2023), Nancy, France, 12th September 2023.

- L Aucone et al., "Experiments and numerical modelling of negative triangularity ASDEX Upgrade plasmas in view of DTT scenarios", Conference: 27th Joint EU-US Transport Task Force Meeting (TTF 2023), Nancy, France, 12th September 2023.

- G Ciraolo et al., "Investigation of JET H-mode edge plasma and derivation of a scaling law for separatrix density as a function of engineering parameters", Conference: 49th European Conference on Plasma Physics (EPS 2023)., Bordeaux, France, 3rd July 2023.

- A Mariani et al., "Negative triangularity scenarios: from TCV and AUG experiments to DTT predictions", Conference: 29th IAEA Fusion Energy Conference, London, United Kingdom, 16th October 2023.

- C Theiler et al., "Experimental and numerical progress in the assessment of alternative divertor configurations in TCV and extrapolations towards higher power conditions", Conference: Fourth Technical Meeting on Divertor Concepts, Vienne, 7th November 2022.

- J Ball et TSVV 2 team, "Insights into a negative triangularity reactor from EUROfusion's TSVV 2", Journal: Plasma Physics and Controlled Fusion, submitted.

Bibliography

[1] 2012. URL: https://www.iter.org/newsline/243/1326.

[2] Emilio Acampora et al. "Conceptual design of in-vessel divertor coils in DTT". In: *Fusion Engineering and Design* 193 (2023), p. 113651.

[3] Julio J Balbin-Arias et al. "Investigation of the dependency of JET mid-plane separatrix density as a function of engineering parameters". In: *Contributions to Plasma Physics* 60.5-6 (2020), e201900157.

[4] S. Baschetti et al. "A model for plasma anomalous transport in tokamaks: closure via the scaling of the global confinement". In: *Nuclear Materials and Energy* 19 (2019), pp. 200–204. ISSN: 2352-1791.

[5] S. Baschetti et al. "Self-consistent cross-field transport model for core and edge plasma transport". In: 61.10 (Sept. 2021), p. 106020.

[6] P Blanchard et al. "Thomson scattering measurements in the divertor region of the TCV tokamak plasmas". In: *Journal of Instrumentation* 14.10 (2019), p. C10038.

[7] J Bohdansky, J Roth, and HL Bay. "An analytical formula and important parameters for low-energy ion sputtering". In: *Journal of Applied Physics* 51.5 (1980), pp. 2861–2865.

[8] SI Braginskii. "Transport processes in a plasma". In: *Reviews of plasma physics* 1 (1965), p. 205.

[9] M Brix et al. "Accuracy of EFIT equilibrium reconstruction with internal diagnostic information at JET". In: *Review of Scientific Instruments* 79.10 (2008).

[10] H Bufferand et al. "Progress in edge plasma turbulence modelling—hierarchy of models from 2D transport application to 3D fluid simulations in realistic tokamak geometry". In: *Nuclear Fusion* 61.11 (2021), p. 116052.

[11] H Bufferand et al. "Three-dimensional modelling of edge multi-component plasma taking into account realistic wall geometry". In: *Nuclear Materials and Energy* 18 (2019), pp. 82–86.

105

[12] H. Bufferand et al. "Implementation of drift velocities and currents in SOLEDGE2D–EIRENE". In: *Nuclear Materials and Energy* 12 (2017). Proceedings of the 22nd International Conference on Plasma Surface Interactions 2016, 22nd PSI, pp. 852–857. ISSN: 2352-1791.

[13] Hugo Bufferand et al. "Near wall plasma simulation using penalization technique with the transport code SolEdge2D-Eirene". In: *Journal of Nuclear Materials* 438 (2013), S445–S448.

[14] Hugo Bufferand et al. "Numerical modelling for divertor design of the WEST device with a focus on plasma–wall interactions". In: *Nuclear Fusion* 55.5 (2015), p. 053025.

[15] KH Burrell et al. "Physics of the L-mode to H-mode transition in tokamaks". In: *Plasma Physics and Controlled Fusion* 34.13 (1992), p. 1859.

[16] C. Bustreo et al. "How fusion power can contribute to a fully decarbonized European power mix after 2050". In: *Fusion Engineering and Design* 146 (2019), pp. 2189–2193.

[17] Guido Ciraolo et al. *Derivation of a scaling law for n_{sep}/n_{ped} as a function of engineering parameters in JET H-mode plasma and impact of divertor geometry*. EPS 2023 - 49th Conference on Plasma Physics. Poster. July 2023. URL: https://cea.hal.science/cea-04273678.

[18] Guido Ciraolo et al. "Investigation of Edge and SOL Particle Flux Patterns in High Density Regimes using SOLEDGE2D-EIRENE Code". In: *Contributions to Plasma Physics* 54.4-6 (2014), pp. 432–436.

[19] S. Coda et al. "Physics research on the TCV tokamak facility: from conventional to alternative scenarios and beyond". In: *Nuclear Fusion* 59.11 (Aug. 2019), p. 112023.

[20] AJ Creely et al. "Overview of the SPARC tokamak". In: *Journal of Plasma Physics* 86.5 (2020), p. 865860502.

[21] H De Oliveira et al. "Langmuir probe electronics upgrade on the tokamak à configuration variable". In: *Review of Scientific Instruments* 90.8 (2019).

[22] dtt-project. *dtt-project*. 2023. URL: https://www.dtt-project.it.

[23] Thomas Eich et al. "Scaling of the tokamak near the scrape-off layer H-mode power width and implications for ITER". In: *Nuclear fusion* 53.9 (2013), p. 093031.

[24] TE Evans et al. "Suppression of large edge localized modes in high confinement DIII-D plasmas with a stochastic magnetic boundary". In: *Journal of nuclear materials* 337 (2005), pp. 691–696.

[25] M Faitsch et al. "Dependence of the L-Mode scrape-off layer power fall-off length on the upper triangularity in TCV". In: *Plasma Physics and Controlled Fusion* 60.4 (2018), p. 045010.

[26] M. Faitsch et al. "Broadening of the power fall-off length in a high density, high confinement H-mode regime in ASDEX Upgrade". In: *Nuclear Materials and Energy* 26 (2021), p. 100890.

[27] O. Février et al. "Divertor closure effects on the TCV boundary plasma". In: *Nuclear Materials and Energy* 27 (2021), p. 100977. ISSN: 2352-1791.

[28] Alexandre Fil et al. "Separating the roles of magnetic topology and neutral trapping in modifying the detachment threshold for TCV". In: *Plasma Physics and Controlled Fusion* 62.3 (2020), p. 035008.

[29] Lorenzo Frassinetti et al. "Role of the separatrix density in the pedestal performance in deuterium low triangularity JET-ILW plasmas and comparison with JET-C". In: *Nuclear Fusion* 61.12 (2021), p. 126054.

[30] D Galassi et al. "Numerical investigation of optimal divertor gas baffle closure on TCV". In: *Plasma Physics and Controlled Fusion* 62.11 (2020), p. 115009.

[31] Manuel García Muñoz et al. "Overview of the TCV tokamak experimental programme". In: *Nuclear Fusion, 62 (4), 042018.* (2022).

[32] L Gil et al. "Stationary ELM-free H-mode in ASDEX Upgrade". In: *Nuclear Fusion* 60.5 (2020), p. 054003.

[33] Robert J Goldston. *Introduction to plasma physics*. CRC Press, 2020.

[34] P-A Gourdain. "The stability of unity beta equilibria in tokamaks". In: *arXiv preprint arXiv:1703.01354* (2017).

[35] M. Greenwald et al. "Characterization of enhanced [formula omitted] high-confinement modes in Alcator C-Mod". In: *Physics of Plasmas* 6.5 (1999). Cited by: 172, pp. 1943–1949.

[36] H.Bufferand. *Global 3D full-scale turbulence simulations of TCV-X21 experiments with SOLEDGE3X*. Presentation at PET-19. 2023.

[37] F.D. Halpern et al. "The GBS code for tokamak scrape-off layer simulations". In: *Journal of Computational Physics* 315 (2016), pp. 388–408.

[38] Woonghee Han et al. "Suppression of first-wall interaction in negative triangularity plasmas on TCV". In: *Nuclear Fusion* 61.3 (2021), p. 034003.

[39] T Happel et al. "Overview of initial negative triangularity plasma studies on the ASDEX Upgrade tokamak". In: *Nuclear Fusion* 63.1 (2022), p. 016002.

[40] Ferdinand Hofmann and Gilbert Tonetti. "Tokamak equilibrium reconstruction using Faraday rotation measurements". In: *Nuclear Fusion* 28.10 (1988), p. 1871.

[41] A Huber et al. "Improved radiation measurements on JET–First results from an upgraded bolometer system". In: *Journal of nuclear materials* 363 (2007), pp. 365–370.

[42] OA Hurricane et al. "Physics principles of inertial confinement fusion and US program overview". In: *Reviews of Modern Physics* 95.2 (2023), p. 025005.

[43] P Innocente et al. "Design of a multi-configurations divertor for the DTT facility". In: *Nuclear Materials and Energy* 33 (2022), p. 101276.

[44] Philippe Jacquet et al. "Maximization of ICRF power by SOL density tailoring with local gas injection". In: *Nuclear Fusion* 56.4 (2016), p. 046001.

[45] A Kallenbach et al. "Multi-machine comparisons of H-mode separatrix densities and edge profile behaviour in the ITPA SOL and Divertor Physics Topical Group". In: *Journal of Nuclear Materials* 337 (2005), pp. 381–385.

[46] Y. Kamada et al. "Disappearance of giant ELMs and appearance of minute grassy ELMs in JT-60U high-triangularity discharges". In: *Plasma Physics and Controlled Fusion* 42.SUPPL. 5A (2000), A247–A253.

[47] M Kikuchi et al. *Impact of High Field & High Confinement on L-mode-Edge Negative Triangularity Tokamak (NTT) Reactor*. Tech. rep. 2018.

[48] M. Kikuchi et al. "L-mode-edge negative triangularity tokamak reactor". In: *Nuclear Fusion* 59.5 (Apr. 2019), p. 056017.

[49] M Kotschenreuther et al. "The super X divertor (SXD) and a compact fusion neutron source (CFNS)". In: *Nuclear Fusion* 50.3 (2010), p. 035003.

[50] M. Kotschenreuther et al. "On heat loading, novel divertors, and fusion reactors". In: *Physics of Plasmas* 14.7 (2007).

[51] Mike Kotschenreuther et al. "Magnetic geometry and physics of advanced divertors: The X-divertor and the snowflake". In: *Physics of Plasmas* 20.10 (2013).

[52] B LaBombard et al. "ADX: a high field, high power density, advanced divertor and RF tokamak". In: *Nuclear Fusion* 55.5 (2015), p. 053020.

[53] AW Leonard et al. "Compatibility of separatrix density scaling for divertor detachment with H-mode pedestal operation in DIII-D". In: *Nuclear Fusion* 57.8 (2017), p. 086033.

[54] K Lim et al. "Effect of triangularity on plasma turbulence and the SOL-width scaling in L-mode diverted tokamak configurations". In: *Plasma Physics and Controlled Fusion* 65.8 (June 2023), p. 085006.

[55] Bruce Lipschultz, Felix I Parra, and Ian H Hutchinson. "Sensitivity of detachment extent to magnetic configuration and external parameters". In: *Nuclear Fusion* 56.5 (2016), p. 056007.

[56] A Loarte et al. "Progress on the application of ELM control schemes to ITER scenarios from the non-active phase to DT operation". In: *Nuclear Fusion* 54.3 (2014), p. 033007.

[57] BC Lyons et al. "Flexible, integrated modeling of tokamak stability, transport, equilibrium, and pedestal physics". In: *arXiv preprint arXiv:2305.09683* (2023).

[58] *Manual of soledge2D*.

[59] Alessandro Marinoni, O Sauter, and S Coda. "A brief history of negative triangularity tokamak plasmas". In: *Reviews of Modern Plasma Physics* 5.1 (2021), p. 6.

[60] R. Maurizio et al. "H-mode scrape-off layer power width in the TCV tokamak". In: *Nuclear Fusion* 61.2 (Jan. 2021), p. 024003.

[61] C Meineri et al. "Numerical study of fully baffled Super-X L-mode discharges on TCV". In: *Nuclear Materials and Energy* 34 (2023), p. 101383.

[62] M. Merola et al. "Overview on fabrication and joining of plasma facing and high heat flux materials for ITER". In: *Journal of Nuclear Materials* 307-311 (2002), pp. 1524–1532.

[63] Jan Mlynar et al. *Bolometry on the TCV Tokamak*. Tech. rep. 1999.

[64] Fabio Mombelli. "Numerical investigation of negative triangularity boundary plasmas through the SOLPS-ITER code". In: (2022).

[65] P Muscente et al. "Analysis of edge transport in L-mode negative triangularity TCV discharges". In: *Nuclear Materials and Energy* 34 (2023), p. 101386.

[66] A.O. Nelson, C. Paz-Soldan, and S. Saarelma. "Prospects for H-mode inhibition in negative triangularity tokamak reactor plasmas". In: *Nuclear Fusion* 62.9 (Aug. 2022), p. 096020.

[67] AO Nelson et al. "Robust avoidance of edge-localized modes alongside gradient formation in the negative triangularity tokamak edge". In: *arXiv preprint arXiv:2305.13458* (2023).

[68] Kai Henrik Nordlund et al. "European research roadmap to the realisation of fusion energy". In: (2018).

[69] W. Obert et al. "Performance of the JET pumped divertor cryopump system". In: *Proceedings of 16th International Symposium on Fusion Engineering*. Vol. 1. 1995, 742–745 vol.1.

[70]   Jef Ongena. "Fusion: a true challenge for an enormous reward". In: *EPJ Web of Conferences* 189 (Jan. 2018), p. 00015. DOI: 10.1051/epjconf/201818900015.

[71]   A. Paredes et al. "Penalization technique to model wall-component impact on heat and mass transport in the tokamak edge". In: *Journal of Nuclear Materials* 438 (2013), S625–S628.

[72]   T.W. Petrie et al. "Effect of separatrix magnetic geometry on divertor behavior in DIII-D". In: *Journal of Nuclear Materials* 438 (2013), S166–S169. ISSN: 0022-3115.

[73]   TW Petrie et al. "Effect of changes in separatrix magnetic geometry on divertor behaviour in DIII-D". In: *Nuclear Fusion* 53.11 (2013), p. 113024.

[74]   Charles Spencer Pitcher and PC Stangeby. "Experimental divertor physics". In: *Plasma Physics and Controlled Fusion* 39.6 (1997), p. 779.

[75]   "Power exhaust in tokamaks and scenario integration issues". In: *Fusion Engineering and Design* 122 (2017), pp. 256–273.

[76]   H Reimerdes et al. "Assessment of alternative divertor configurations as an exhaust solution for DEMO". In: *Nuclear Fusion* 60.6 (2020), p. 066030.

[77]   H. Reimerdes et al. "Overview of the TCV tokamak experimental programme". In: *Nuclear Fusion* 62.4 (Mar. 2022), p. 042018.

[78]   Detlev Reiter, Martine Baelmans, and Petra Boerner. "The EIRENE and B2-EIRENE codes". In: *Fusion science and technology* 47.2 (2005), pp. 172–186.

[79]   TD Rognlien, ME Rensink, and GR Smith. "Users manual for the UEDGE edge-plasma transport code". In: *Lawrence Livermore National Lab. Report No. UCRL-ID-137121* (2000).

[80]   S Saarelma et al. "Testing a prediction model for the H-mode density pedestal against JET-ILW pedestals". In: *Nuclear Fusion* 63.5 (2023), p. 052002.

[81]   O. Sauter. "Geometric formulas for system codes including the effect of negative triangularity". In: *Fusion Engineering and Design* 112 (2016), pp. 633–645. ISSN: 0920-3796.

[82]   Jacob A Schwartz, Andrew Oakleigh Nelson, and Egemen Kolemen. "To dee or not to dee: costs and benefits of altering the triangularity of a steady-state DEMO-like reactor". In: *Nuclear Fusion* 62.7 (2022), p. 076006.

[83]   Thomas E Schwartzentruber, Leonardo C Scalabrin, and Iain D Boyd. "Multiscale particle-continuum simulations of hypersonic flow over a planetary probe". In: *Journal of Spacecraft and Rockets* 45.6 (2008), pp. 1196–1206.

[84] D Silvagni et al. "Scrape-off layer (SOL) power width scaling and correlation between SOL and pedestal gradients across L, I and H-mode plasmas at ASDEX Upgrade". In: *Plasma Physics and Controlled Fusion* 62.4 (2020), p. 045015.

[85] Boris V Somov. "The Generalized Ohm's Law in Plasma". In: *Plasma Astrophysics* (2007), pp. 193–204.

[86] VA Soukhanovskii. "A review of radiative detachment studies in tokamak advanced magnetic divertor configurations". In: *Plasma Physics and Controlled Fusion* 59.6 (2017), p. 064005.

[87] P Stangeby. "Tutorial on some basic aspects of divertor physics". In: *Plasma Physics and Controlled Fusion* 42 (Dec. 2000), B271.

[88] Peter C Stangeby et al. *The plasma boundary of magnetic fusion devices.* Vol. 224. 2000.

[89] A. Stegmeir et al. "Global turbulence simulations of the tokamak edge region with GRILLIX". In: *Physics of Plasmas* 26.5 (May 2019), p. 052517.

[90] J. Stober et al. "Type II ELMy H modes on ASDEX upgrade with good confinement at high density". In: *Nuclear Fusion* 41.9 (2001), pp. 1123–1134.

[91] Patrick Tamain et al. "The TOKAM3X code for edge turbulence fluid simulations of tokamak plasmas in versatile magnetic geometries". In: *Journal of Computational Physics* 321 (2016), pp. 606–623.

[92] C Theiler et al. "Advances in understanding power exhaust physics with the new, baffled TCV divertor". In: *28th IAEA Fusion Energy Conference (FEC 2020).* 2021.

[93] C Theiler et al. "Results from recent detachment experiments in alternative divertor configurations on TCV". In: *Nuclear Fusion* 57.7 (2017), p. 072008.

[94] Christian Theiler. "Basic Investigation of Turbulent Structures and Blobs of Relevance for Magnetic Fusion Plasmas". PhD thesis. 2011.

[95] Kathreen Thome. "Initial Results from the DIII-D Negative Triangularity Campaign". In: *MagNatUS Meeting 2023.* 2023, p. 13.

[96] F. Troyon and R. Gruber. "A semi-empirical scaling law for the -limit in tokamaks". In: *Physics Letters A* 110.1 (1985), pp. 29–34.

[97] Prashant M Valanju et al. "Super-X divertors and high power density fusion devices". In: *Physics of Plasmas* 16.5 (2009).

[98] Matteo Valentinuzzi et al. "Fluid description of neutral particles in divertor regimes in WEST". In: *Contributions to Plasma Physics* 58.6-8 (2018), pp. 710–717.

[99] Liang Wang et al. "Achievements of actively controlled divertor detachment compatible with sustained high confinement core in DIII-D and EAST". In: *Nuclear Fusion* 62.7 (2022), p. 076002.

[100] M Wensing et al. "SOLPS-ITER validation with TCV L-mode discharges". In: *Physics of Plasmas* 28.8 (2021).

[101] John Wesson and David J Campbell. *Tokamaks*. Vol. 149. Oxford university press, 2011.

[102] Sven Wiesen et al. "The new SOLPS-ITER code package". In: *Journal of nuclear materials* 463 (2015), pp. 480–484.

[103] HR Wilson et al. "Numerical studies of edge localized instabilities in tokamaks". In: *Physics of Plasmas* 9.4 (2002), pp. 1277–1286.

[104] *www.soledge3x.com*.

[105] X Xu et al. "Boundary plasma turbulence simulations for tokamaks". In: *Communications in Computational Physics, vol. 4, no. 5, July 1, 2008, pp. 949-979* 4.LLNL-JRNL-404082 (2008).

[106] Hartmut Zohm et al. "Studies of edge localized modes on ASDEX". In: *Nuclear fusion* 32.3 (1992), p. 489.